Spring 1-1-2018

Lamb Waves with Conical Dispersion at Zero Wavenumber

David M. Stobbe
University of Colorado at Boulder, david.stobbe@colorado.edu

Lamb Waves with Conical Dispersion at Zero Wavenumber

by

David M. Stobbe

B.S., University of Michigan, 2003

M.S., Georgia Institute of Technology, 2005

A thesis submitted to the

Faculty of the Graduate School of the

University of Colorado in partial fulfillment

Of the requirement for the degree of

Doctor of Philosophy

Department of Mechanical Engineering

2018

This thesis entitled:

Lamb Waves with Conical Dispersion at Zero Wavenumber

Written by David Stobbe

Has been approved for the Department of Mechanical Engineering

_____

Professor Todd Murray

_____

Professor Xiaobo Yin

Date:

The final copy of this thesis has been examined by the signatories, and we find that both the content and the form meet acceptable presentation standards of scholarly work in the above mentioned discipline.

Abstract

Stobbe, David (Ph.D., Mechanical Engineering)

Lamb Waves with Conical Dispersion at Zero Wavenumber

Thesis directed by Associate Professor Todd Murray

Lamb waves are guided elastic waves in plates. These waves are dispersive, with the frequency and wavenumber related by the well-known Rayleigh-Lamb equation. Generally, at zero wavenumber the dispersion curves are parabolic and the waves are non-propagating thickness resonances. For distinct values of Poisson's ratio, however, degeneracy can occur between thickness resonance modes. At these coincidence frequencies the dispersion curves become linear and in a three-dimensional representation the dispersion surface is shaped like a cone. This behavior is referred to as conical dispersion. Waves excited at coincidence frequencies maintain the infinite phase velocity associated with thickness resonances but transport energy at a finite group velocity. A unique characteristic of such waves is that they propagate with an infinite wavelength, resulting in uniform oscillation of the plate surface. Conical dispersion essentially decouples the spatial and temporal behavior of the wave field and produces a field that is static in space yet oscillating in time.

The focus of this thesis is to investigate Lamb waves with conical dispersion in homogenous isotropic plates. The mode shapes and energy transport along the plate are analyzed in order to elucidate the origin of conical dispersion for a specific degenerate case. The theoretical group velocity is derived based on the velocity of energy transport. Conical dispersion

is measured in an aluminum plate by cooling the plate in order to tune Poisson's ratio through the degenerate point. Linear dispersion at zero wavenumber is measured and found to agree with the theory. Waves excited near the degenerate frequency exhibited spatially uniform phase over the plate surface. Mode conversion upon encountering the free edge of the plate is studied. The mode converted field is found to propagate perpendicular to the plate edge, irrespective of angle of incidence. This behavior is demonstrated by focusing a mode converted field from a semi-circular edge in the plate. This peculiar type of lens will focus the field regardless of the location of the source on the plate. Experimental results also show that Lamb waves with conical dispersion flow around a hole in the plate without distortion. This phenomenon causes the hole in the plate to be hidden when observing just the long wavelength signal distal to the hole. All of the experimental results are confirmed by comparison with time domain finite element simulations. We propose that Lamb waves with conical dispersion allow the manipulation of elastic energy in novel ways and may find use in nondestructive evaluation of materials and development of acoustic devices.

Acknowledgements

I would like to thank my advisor Dr. Todd Murray for his support while conducting this work. Dr. Murray brought tremendous expertise to this topic and was always willing to engage in spirited debate over data and theory.

I would like to thank the members of the Borden and Murray lab groups. Thanks to Andrew Bakir, Jordan Lum, Alec Thomas, and Marco Inzunza for their assistance with running and maintaining the laser optics lab. Special thanks to Jordan and Marco for being flexible with their lab time schedules and for shutting down my experiments for me after hours.

I would most of all like to thank my wife Katrina for her patience and support during this research.

Contents

Figures

Chapter 1

Introduction

1.1 Brief history of elastic waves

Elastic wave propagation was first studied in the early 1800s by Young and Fresnel [1]. At the time they were investigating the nature of light, which, at the time, was thought to propagate through an elastic ether. Concurrently, the fundamental mathematics of classical elasticity was described by Cauchy and Navier [1] including the stress and displacement equations of motion. Additionally, Poisson [2] and Lamè [3] discovered that all elastic waves could be decomposed into dilatational (longitudinal) and equivoluminal (shear) waves, allowing the equations of motion to be represented by the sum of a scalar potential and a vector potential, each of which satisfies the wave equation. With these tools, 19th century researchers studied the propagation of waves in elastic half spaces due to harmonic surface disturbances [4]. This work elucidated the existence and velocities of the common bulk wave modes: shear vertical (SV), shear horizontal

(SH), and dilatational (L), where the velocity of the first two are equal in the case of an isotropic medium.

In the early 20th century, interest in seismology spurred the study of wave propagation on elastic half spaces. Rayleigh was first to explore the behavior of waves propagating along the traction free surface of an elastic half space, leading to the discovery of the Rayleigh or surface wave [5]. Lamb then considered the propagation of a pulse through an elastic half space [6] and the problem now bears his name. Lamb's problem was treated by later researchers [7] and most notably by Cagniard [8] who used Laplace and Fourier integral transforms to solve the transient wave problem. This technique is still used in modern elastodynamics, when finite element techniques are not employed. Love [9] considered modified Rayleigh waves which occur on the free surface of an elastic half space that is welded to another half space, where the upper half space has a low wave speed compared to the lower half space. Stonely [10] noted that in such a system a generalized Rayleigh wave occurs along the interface of the half spaces. This work laid much of the foundation for modern semiology.

Waveguides were first considered in the mid-18th century as one-dimensional vibrating elastic bars and rods. The flexural (shear) vibrations of such bodies were derived by Euler and Bernoulli and the extensional (longitudinal) vibrations were derived by Navier [4]. In the late-19th century Pochhammer [11] formulated the general theory for vibrating cylinders of infinite length and traction free lateral surfaces. Pochhammer derived the frequency equations for such cylinders, which relates the frequency and wavenumber for flexural, extensional, and torsional waves. A similar analysis was performed on infinite plates that are traction free on the top and bottom surfaces by Lamb [12] and Rayleigh [13], where the frequency and wavenumber are

related by the Rayleigh-Lamb frequency equation. Waves which propagate in elastic plates are referred to as Lamb waves.

Lamb waves

The frequency equations for plates exhibit an infinite number of branches (modes) and due to the intractable nature of the equations, Lamb wave study was largely limited to the lowest frequency modes until the work performed by Mindlin in the mid-20th century [14]. Mindlin was the first to sketch the shape of the higher-order real modes in an isotropic homogenous elastic plate of infinite dimension. He accomplished this by partitioning the frequency-wavenumber space using solutions to the uncoupled dilatational and equivolmunial waves. He then sketched the "terrace-like" structure within these partitions of modes that occurred when the dilatational and equivolmunial waves interacted with one another. Mindlin curves are generally no longer necessary due to modern computers which are able to numerically solve the frequency equations. However, Mindlin curves are still useful in understanding the physics underlying Lamb waves and are but one of Mindlin's many contributions to the field. The topic of elastic waveguides has been treated in great detail by several other modern authors: Miklowitz [4], Auld [15], Rose [16], and Achenbach [17].

The renewed and continued interest in Lamb waves, since Mindlin's work, has been due primarily to the engineering need for non-destructive structural health monitoring (NDSHM) and non-destructive evaluation (NDE) of materials. Lamb waves are useful in this regard due to their ability to inspect entire structures over long distances with high sensitivity to defects [18]. Examples of Lamb waves used for NDSHM are: pipe systems, aircraft skin, and composite or layered structures [19-22]. Lamb waves are also used to characterize particular geometric

dimensions or material properties (NDE). A recent technique for measuring the elastic properties of plates using a laser excitation to excite selected plate resonances is discussed in detail in Section 1.2.1 due to its use in this manuscript. More recently, Lamb waves have drawn new interest due to advances in the field of metamaterials. Metamaterials are materials engineered to have properties which do not occur in nature and are often achieved using a repeated structure on or less than the wavelength scale of a particular phenomenon. Recently, metamaterials have been fabricated with a negative index of refraction; that is, they support backward propagating waves. Materials that display backward wave motion have been demonstrated in electro-magnetic and mechanical metamaterials [23-26], photonic and phononic crystals [27-29], and mechanical and electro-magnetic wave guides [30-35]. These materials allow for wave fields to be manipulated in novel waves including lensing from a flat interface [36-43]. Interestingly, simple elastic plates also support backward wave motion [44] and have been used to create a flat lens as well [45-46]. Backward propagating Lamb waves are discussed in more detail in Section 1.2.2 due to their relationship with conical point Lamb waves and this author's own research on the matter.

Another area of recent interest in both the photonics and acoustics communities is the development of metamaterials that exhibit conical dispersion at zero wavenumber [47-55]. This behavior is typically referred to as Dirac cone or Dirac-like cone dispersion and occurs in a material with a zero-index (ZIM) or near zero-index (NZIM) of refraction. These materials can be used to manipulate wave fields in novel ways including: tunneling, beam steering, total reflection, cloaking, and lensing [47-55]. Just as the case with backward waves, a similar behavior to Dirac cone dispersion also exists in Lamb waves. This fact was recently highlighted by Maznev [56] where he discussed the condition for occurrence of such waves in elastic plates and noted some of the similarities (and differences) between conical dispersion in plates and

metamaterials. This manuscript will demonstrate conical dispersion in a simple aluminum plate and experimentally show that Lamb waves with conical dispersion can be used to manipulate wave fields in interesting and novel ways.

1.2 Modern topics in Lamb wave research

1.2.1 Zero group velocity points

A peculiar property of Lamb waves is the existence of frequency and wavenumber points where the phase velocity is finite but the group velocity is zero. These points are commonly referred to as zero group velocity (ZGV) points. One such point is shown and labeled as ZGV in Fig. 1.1, which shows the dispersion curves for a plate with Poisson's ratio = 0.35. These points have been known since the 1950's, but have recently experienced renewed interest [57-66] and have been shown to be a powerful NDE tool. Some NDE applications include: thin layer thickness measurement [63], interfacial stiffness measurement [64], and material property measurement [59]. ZGV Lamb waves are useful because the frequency at which they occur is a function of the plate thickness and elastic properties and their frequency can be measured with high accuracy. The high accuracy comes from the fact that ZGV points are stationary resonances and accordingly they slowly ring down over many cycles. This was first noted by Tolstoy and Usdin [67] who hypothesized the wave behavior of a ZGV point as "associated with a sharp continuous wave resonance and ringing effects". Additionally, Prada et al. [58] reported that ZGV Lamb waves in thin plates could be excited with a low-power amplitude modulated laser source and

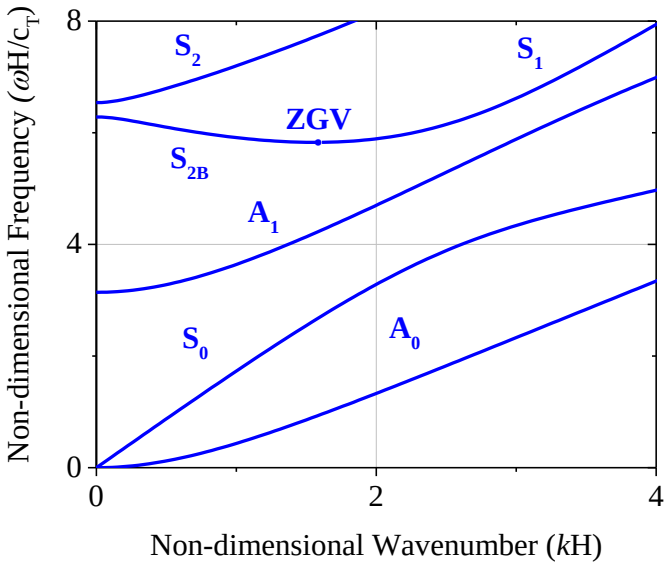

Fig. 1.1. Dispersion curves for Lamb waves in a plate with Poisson's ratio = 0.35. The "S" and "A" refer to symmetric and antisymmetric modes, respectively.

measured with a high-quality factor (Q) using an optical interferometer. A laser-based method for measuring Poisson ratio to within ±0.2% was presented by Clorennec et. al. [59]. The origin of ZGV points in the frequency dispersion stems from the repulsion of same symmetry modes [64]. The most commonly studied ZGV point is that shown in Fig. 1.1, which occurs at the intersection of the S_1 and S_{2B} modes and results from the repulsion of the S_2 and S_{2B} modes near zero wavenumber. One reason this ZGV point is of interest is because it occurs over the range of elastic properties commonly found in engineering materials ($0 \leq \nu \leq 0.43$) [68]. The repulsion between the S_2 and S_{2B} modes near zero wavenumber causes a "dip" in the S_{2B} mode and results in backward propagating waves in the S_{2B} mode. Backward propagating waves are discussed in more detail in Section 1.2.2. The amount of repulsion between these modes is related to their proximity, which is set by the elastic properties of the plate.

1.2.2 Backward propagating Lamb waves

For some Lamb wave modes, the dispersion curve has negative slope near zero wavenumber, as observed in the S_{2B} mode in Fig. 1.1. This curvature results in backward propagating waves, which are waves with anti-parallel phase velocity and group velocity. Physically, backward waves emanate away from the source but the individual wave-fronts travel back toward the source. An interesting quality of such waves is that when they mode convert to or from a regular forward propagating wave, negative reflection and/or refraction occurs. Recent experiments have demonstrated that negative refraction can be used to create a flat tunable acoustic lens by machining a symmetric trough in an aluminum plate [45-46], an example of such a lens is shown in Fig. 1.2.

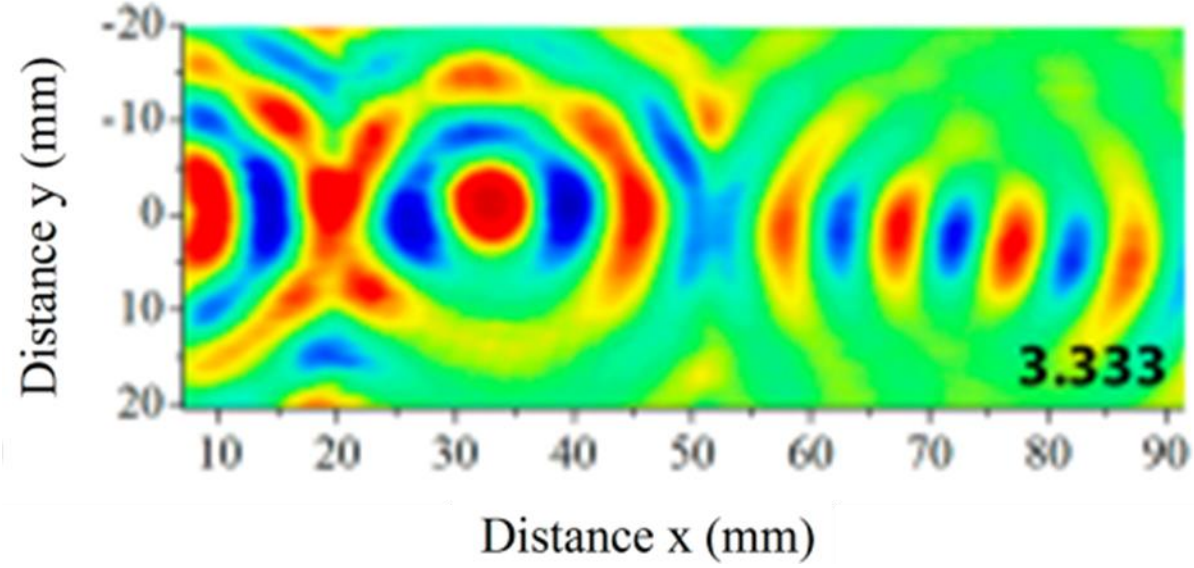

Fig. 1.2. Normal displacement at 3.333 MHz of an aluminum plate excited by a pulse from a transducer array located at x = 0 mm and y = 0 mm. The wave field is focused within the symmetric trough due to negative refraction from the flat interface at x = 18 mm. The field is then focused again after the trough from the second flat interface at x = 51 mm [46].

Further, consider a backward propagating Lamb wave that is incident on the free edge of a plate. The physics of such a scenario are interesting because if the incident backward wave mode converts to a forward wave upon reflection, it will be directed on the same side of the surface normal as the incident wave (negative reflection). Negative reflection of Lamb waves was first shown by Germano et al. [69] by reflecting a forward propagating Lamb wave from the free edge of a steel plate and observing the reflected field on the same side of the surface normal as the incident wave. More recently, broad angle negative reflection was demonstrated by reflecting a backward propagating Lamb wave off the free edge of an aluminum plate [70-71]. Here the mode converted field was focused from the flat edge.

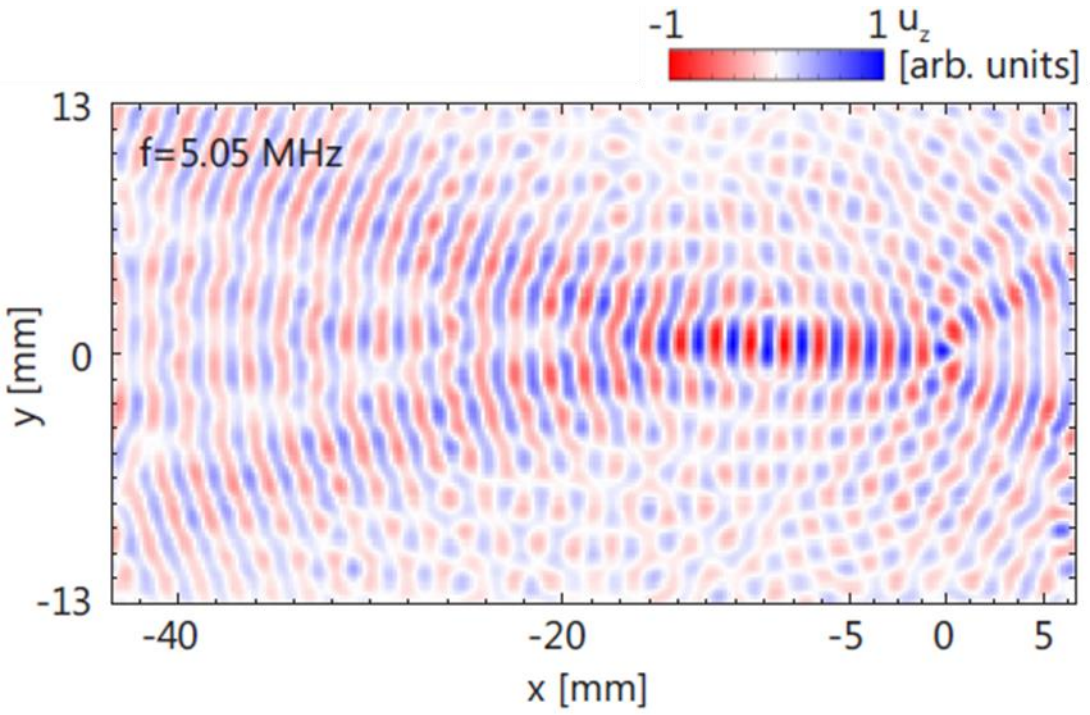

Fig. 1.3. Normal displacement at 5.05 MHz of an aluminum plate excited by a continuous wave laser source at x = 0 mm and y = 0 mm. The plate has a flat edge located at x = 7 mm. The wave field is spatially bandpass filtered in order to isolate the reflected S_1 mode. Negative reflection and field focusing can be observed [70].

An interesting quality of dispersion curves that exhibit backward wave motion is that the backward propagating mode ultimately intersects with a forward propagating mode at a ZGV point. This is noteworthy because reflection between backward and forward modes (and *vice versa*) proximate to the ZGV point will nearly retrace one another. This behavior has been studied by Gérardin et. al. [71] where they show that "In the vicinity of the ZGV-point, wave numbers coincide and the wave is retro-reflected on the source. In this frequency range, the free edge acts as a perfect phase conjugating mirror."

This author has explored backward propagating Lamb waves and this work is detailed in Appendix A. In brief, this work used finite element analysis to explore aspects of negative refraction including Lamb wave steering and quantifying the ideal focusing resolution of an elastic lens. The mode conversion efficiency between forward and backward Lamb waves as a function of temporal frequency, angle of incidence, and interface geometry was also explored. There is a demonstration of partial source annihilation using two sources, one generating a forward propagating wave and the other generating a backward propagating wave. Finally, although not discussed in Appendix A or in the current literature, it should be noted that regions of backward wave propagation appear to behave as a "complimentary material" [72] to regions of forward wave propagation. This author has briefly investigated this phenomenon and found that indeed regions of space can be effectively "cancelled out" using backward waves. This behavior and interpretation of backward waves is worthy of further investigation in this author's opinion.

1.3 Dirac Points and Conical Dispersion

The previous Sections discussed the Lamb wave topics of ZGV points and backward waves. It was noted that both of these features are a result of dispersion curve repulsion near zero wavenumber. The frequencies at which the dispersion curves cross zero wavenumber depend on the plate's elastic properties and thickness. The relative proximity between modes at zero wavenumber depends solely on Poisson's ratio. For example, the spacing between the S_2 and S_{2B} modes, at zero wavenumber, in Fig. 1.1 is determined solely by Poisson's ratio. Mindlin [14] showed that for multiple distinct values of Poisson's ratio some modes become coincident at zero wavenumber and in the cases where these modes are of the same symmetry degeneracy occurs. In these degenerate cases the dispersion curves become linear at zero wavenumber instead of parabolic. Linear dispersion at zero wavenumber in a three-dimensional representation assumes the shape of a cone [73] and accordingly is referred to as conical dispersion in this manuscript. This is remarkable because Lamb waves at zero wavenumber are normally stationary resonances. However, in the event of conical dispersion, Lamb waves at zero wavenumber become propagating waves that have an infinite wavelength and infinite phase velocity. An infinite wavelength essentially decouples the spatial and temporal behavior of the wave field and produces a field that is static in space yet oscillating in time [74]. Due to the recent interest in metamaterials with conical (Dirac) dispersion at zero wavenumber, Maznev published a paper [56] highlighting such behavior in elastic plates. Here he suggested tuning a plate's Poisson's ratio to a degenerate condition by coating the plate to create a bi-layer. This technique allows the tuning of the total effective Poisson's ratio for the plate. This is the extent of the research into conical dispersion in elastic plates until the work performed in this manuscript [74-75].

1.4 Objectives of this dissertation

1.4.1 Scope

The main objective of this manuscript is to study Lamb waves with conical dispersion at zero wavenumber in simple elastic plates. This work covers the theory for causing conical dispersion in plates and shows a way to induce this behavior in a commercially available aluminum plate. Multiple experiments and numerical simulations are then performed in order to both demonstrate conical dispersion and to show how it can be used to manipulate elastic waves in novel waves. A brief outline of the Chapters is given.

Chapter 2 Lamb Wave Theory: provides the background and theory pertaining to Lamb waves with conical dispersion at zero wavenumber. The mode shapes of the simple thickness resonances are used to explain how coincident longitudinal and shear thickness resonances of the same symmetry lead to propagating waves. The group velocity of Lamb waves with conical dispersion at zero wavenumber are calculated from the modes shapes and are shown to agree with the group velocity previously derived by Mindlin [14].

Chapter 3 Inducing and Measuring Conical Dispersion of Lamb Waves: details experimental results showing that conical dispersion can be induced in a simple aluminum plate by cooling the plate such that degeneracy occurs between the S_2 and S_{2B} modes at zero wavenumber. Linear dispersion is measured in the transition from backward to forward propagating waves near zero wavenumber and the group velocity proximate to zero wavenumber is measured and confirmed to agree with that predicted by theory.

Chapter 4 Reflection of Lamb waves with Conical Dispersion from a Free Edge: finite element simulation and experiment are used to demonstrate that Lamb waves with conical dispersion can be used to focus a mode converted reflected field from the free edge of a plate. The results show how conical point Lamb waves lose a sense of directionality and behave as if they were decoupled in space and time. Because of this, any mode converted wave is reflected normal to the edge and consequently the geometry of a reflected field can be controlled by the shape of the edge.

Chapter 5 Scattering of Lamb waves with Conical Dispersion: finite element simulations and experiments are used to study how Lamb waves with conical dispersion scatter from single and multiple holes in a plate. Here it is shown that in the long wavelength limit the steady state field is unperturbed by a finite sized hole. It is also shown how this effect can be used to create a type of pseudo-cloaking. Specifically, single and multiple scatterers are hidden, when observing a mode converted field distal to the scatterers. It is also observed that a conical point Lamb wave reflects a mode converted field from scatterers. This reflected field is uniform around the scatterer, again confirming that the conical point wave is decoupled in space and time.

Chapter 6 Conclusions and Future Work: summarizes the findings in this manuscript and details suggested areas of future investigation into conical dispersion of Lamb waves.

1.4.2 Significance

A theoretical background for the occurrence of conical dispersion in elastic plates and a physical explanation for why this occurs in presented. The finite group velocity that results from coincident longitudinal and shear simple thickness resonances, of the same symmetry, is

physically explained using displacement and stress mode shapes and the value of this group velocity is derived. Lamb waves with conical dispersion at zero wavenumber are measured for the first time in a simple elastic plate. Lensing a reflected wave field from a Lamb wave with conical dispersion is experimentally demonstrated for the first time. Finally, scattering a Lamb wave with conical dispersion from a finite sized hole is studied and demonstrated for the first time. These results are significant because they demonstrate new ways that elastic energy can be manipulated using a simple plate.

1.5 References

[1] A. E. Love, *Mathematical Theory of Elastic Systems* (McGraw-Hill Inc., New York 1944).

[2] S. D. Poisson, *Royal Academy of Science Paris*, 8 (1829).

[3] G. Lamè, *Lessons on the mathematical theory of the elasticity of solid bodies,* Paris (1852).

[4] J. Miklowitz, *The Theory of Elastic Waves and Waveguides* (North Holland Publishing Company 1978).

[5] Lord Rayleigh, *Proceedings of the London Mathematical Society*, 17 (1887).

[6] H. Lamb, *Philosophical Transactions of the Royal Society London*, 203 (1904).

[7] E. R. Lapwood, *Philosophical Transactions of the Royal Society London*, 242 (1949).

[8] L. Cagniard, *Reflection and Refraction of Progressive Seismic Waves* (Mc-Graw-Hill Inc. New York, 1962).

[9] A. E. Love, *Some Problems of Geodynamics* (Cambridge University Press, Cambridge 1911).

[10] R. Stonely, *Proceedings of the London Mathematical Society*, 106 (1924).

[11] L. Pochhammer, *Journal of Mathematics (Germany)*, 81 (1876).

[12] L. Rayleigh, *Proceedings of the London Mathematical Society*, 20 (1889).

[13] H. Lamb, *Proceedings of the London Mathematical Society*, 21 (1890).

[14] R. D. Mindlin, *An Introduction to the Mathematical Theory of Vibrations of Elastic Plates* (World Scientific, Singapore, 2016).

[15] B. A. Auld, *Acoustic Fields and Waves in Solids* (John Wiley and Sons, New York 1973).

[16] J. L. Rose, *Ultrasonic Waves in Solid Media* (Cambridge University Press 1999).

[17] J. D. Achenbach, *Wave Propagation in Elastic Solids* (North-Holland, Amsterdam, 1973).

[18] D. C. Worlton, "Experimental confirmation of Lamb waves at megacycle frequencies," J. Appl. Phys. 32 (1961).

[19] E. A. Birt, “Damage detection in carbon-fibre composites using ultrasonic Lamb waves,” Insight 40 (1998).

[20] M. Lemistre, D.L. Balageas, “Structural health monitoring system based on diffracted Lamb wave analysis by multiresolution processing,” Smart Mater. Struct. 10 (2001).

[21] J.D. Achenbach, “Quantitative nondestructive evaluation,” Int. J. Solids Struct. 37 (2000).

[22] M. Z. Silva, R. Gouyon, and F. Lepoutre, “Hidden corrosion detection in aircraft aluminium structures using laser ultrasonics and wavelet transform signal analysis,” Ultrasonics 41 (2003).

[23] 1. R. A. Shelby, D. R. Smith, and S. Schultz, “Experimental Verification of a Negative Index of Refraction”, Science 292, 77 (2001).

[24] A. A. Houck, J. B. Brock, and I. L. Chuang, “Experimental Observation of a Left-Handed Material That Obeys Snell’s Law”, Phys. Rev. Lett. 90, 137401 (2003).

[25] N. Fang, D. Xi, J. Xu, M. Ambati, W. Srituravanich, C. Sun, and X. Zhang, “Ultrasonic metamaterials with negative modulus”, Nature Materials 5, 452-456 (2006).

[26] S. Zhang, L. Yin, and N. Fang, “Focusing Ultrasound with an Acoustic Metamaterial Network”, Phys. Rev. Lett. 102, 194301 (2009).

[27] 5. A. Sukhovich, B. Merheb, K. Muralidharan, J. O. Vasseur, Y. Pennec, P. A. Deymier, and J. H.Page, "Experimental and theoretical evidence for subwavelength imaging in phononic crystals." Phys. Rev. Lett. 102, 154301 (2009).

[28] M. Notomi, “Theory of light propagation in strongly modulated photonic crystals: Refractionlike behavior in the vicinity of the photonic band gap”, Phys. Rev. B 62, 10696 (2000).

[29] E. Cubukcu, K. Aydin, E. Ozbay, S. Foteinopoulou, and C. M. Soukoulis, “Electromagnetic waves: Negative refraction by photonic crystals”, Nature (London) 423, 604 (2003).

[30] I. Tolstoy, and E. Usdin, “Wave Propagation in Elastic Plates: Low and High Mode Dispersion”, J. Acoust. So. Am. 29, 1 (1957).

[31] A. H. Meitzler, “Backward-Wave Transmission of Stress Pulses in Elastic Cylinders and Plates”, J. Acoust. So. Am. 38, 835 (1965).

[32] P. L. Marston, “Negative group velocity Lamb waves on plates and applications to the scattering of sound by shells”, J. Acoust. Soc. Am. 38, 835 (1965).

[33] M. Ibanescu, S. G. Johnson, D. Roundy, C. Luo, Y. Fink, and J. D. Joannopoulos, “Anomalous Dispersion Relations by Symmetry Breaking in Axially Uniform Waveguides”, Phy. Rev. Lett. 92, 6 (2004).

[34] A. L. Shuvalov, and O. Poncelet, “On the backward Lamb waves near thickness resonances in anisotropic”, Int. J. Solids Struct. 45, (2008).

[35] A. A. Maznev and A. G. Every, “Surface acoustic waves with negative group velocity in a thin film structure on silicon”, Appl. Phys. Lett. 95, 011903 (2009).

[36] J. B. Pendry, “Negative Refraction Makes a Perfect Lens”, Phys. Rev. Lett. 85, 3966 (2000).

[37] S. A. Cummer, “Simulated causal subwavelength focusing by a negative refractive index slab”, Appl. Phys. Lett. 95, 011903 (2003).

[38] E. Cubukco, K. Aydin, E. Ozbay, S. Foteinopoulou, and C. M. Soukoulos, “Electromagnetic waves: Negative refraction by photonic crystals”, Nature 423, (2003).

[39] S. Yang, J. H. Page, Z. Liu, M. L. Cowan, C. T. Chan, and P. Sheng, “Focusing of Sound in a 3D Phononic Crystal”, Phys. Rev. Lett. 93, 024301 (2004).

[40] N. Fang, H. Lee, C. Sun, and X. Zhang, “Sub–Diffraction-Limited Optical Imaging with a Silver Superlens”, Science 308, 534 (2005).

[41] S. A. Ramakrishna, “Physics of negative refractive index materials,” Rep. Prog. Phys. 68, 449 (2005).

[42] V. G. Veselago and E.E. Narimanov , “The left hand of brightness: past, present, and future of negative index materials”, Nature Material 5, (2006).

[43] R. Craster and S. Guenneau, “Acoustic metamaterials: Negative refraction, imaging, lensing and cloaking”, Springer-Verlag, London, (2012).

[44] I. Tolstoy, and E. Usdin, “Wave Propagation in Elastic Plates: Low and High Mode Dispersion”, J. Acoust. So. Am. 29, 1 (1957).

[45] S. Bramhavar, C. Prada, A. A. Maznev, A. G. Every, T. B. Norris, and T. W. Murray, “Negative refraction and focusing of elastic lamb waves at an interface”, Phys. Rev. B 83, 014106 (2011).

[46] F. D. Philippe, T. W. Murray, and C. Prada, “Focusing on Plates: Controlling Guided Waves using Negative Refraction”, Sci. Rep. 5, 11112 (2015).

[47] X. Huang, Y. Lai, Z. H. Hang, H. Zheng, and C. T. Chan, Dirac cones induced by accidental degeneracy in photonic crystals and zero-refractive-index materials, Nat. Mater. 10, 582 (2011).

[48] F. Liu, Y. Lai, X Huang, and C. T. Chan, Dirac cones at k = 0 in phononic crystals, Phys. Rev. B 84, 224113 (2011).

[49] M. Silveirinha and N. Engheta, Tunneling of Electromagnetic Energy through Subwavelength Channels and Bends using ε-Near-Zero Materials, Phys. Rev. Lett. 97, 157403 (2006).

[50] R. Liu, Q. Cheng, T. Hand, J. J. Mock, T. J. Cui, S. A. Cummer, and D. R. Smith, Experimental Demonstration of Electromagnetic Tunneling Through an Epsilon-Near-Zero Metamaterial at Microwave Frequencies, Phys. Rev. Lett. 100, 023903 (2008).

[51] J. Hao, W. Yan, and M. Qiu, Super-reflection and cloaking based on zero index metamaterial, Appl. Phys. Lett. 96, 101109 (2010).

[52] F. Liu, X. Huang, and C. T. Chen, Dirac cones at k = 0 in acoustic crystals and zero index acoustic materials, Appl. Phys. Lett. 100, 071911 (2012).

[53] V. C. Nguyen, L. Chen, and K. Halterman, Total Transmission and Total Reflection by Zero IndexMetamaterials with Defects, Phys. Rev. Lett. 105, 233908 (2010).

[54] Q. Wei, Y. Cheng, and X. Liu, Acoustic total transmission and total reflection in zero-index metamaterials with defects, Appl. Phys. Lett. 102, 174104 (2013).

[55] F. Liu and Z. Liu, Elastic Waves Scattering without Conversion in Metamaterials with Simultaneous Zero Indices for Longitudinal and TransverseWaves, Phys. Rev. Lett. 115, 175502 (2015).

[56] A. A. Maznev, Dirac cone dispersion of acoustic waves in plates without phononic crystals, J. Acoust. Soc. Am. 135, 577 (2014).

[57] S.D. Holland, D. Chimenti, Air-coupled acoustic imaging with zero-group-velocity Lamb modes, Appl. Phys. Lett. 83, 2704 (2003).

[58] C. Prada. O. Balogun and T. W. Murray, "Laser-based ultrasonic generation and detection of zero-group velocity Lamb waves in thin plates," Appl. Phys. Lett. 87, 194109 (2005).

[59] D. Clorennec, C. Prada, and D. Royer, "Local and noncontact measurements of bulk acoustic wave velocities in thin isotropic plates and shells using zero group velocity Lamb modes," J. Appl. Phy. 101, 034908 (2007).

[60] D. Clorennec, C. Prada, D. Royer, and T. W. Murray, "Laser impulse generation and interferometer detection of zero group velocity Lamb mode resonance," Appl. Phys. Lett. 89, 024101 (2006).

[61] O. Balogun, T. W. Murray, and C. Prada, "Simulation and measurement of the optical excitation of the zero group velocity Lamb wave resonance in plates," J. Appl. Phy. 102, 064914 (2007).

[62] C. M. Grünsteidl, I. A. Veres, and T. W. Murray, “Experimental and numerical study of the excitability of zero group velocity Lamb waves by laser-ultrasound.” J. Acoust. Soc. Am. 138, 242 (2015).

[63] M. Cès, D. Clorennec, D. Royer, and C. Prada, “Thin layer thickness measurements by zero group velocity Lamb mode resonances,” Rev. Sci. Instrum. 82, 114902 (2011).

[64] C. Prada, D. Clorennec, and D. Royer, “Local vibration of an elastic plate and zero-group velocity Lamb modes,” J. Acoust. Soc. Am. 124, 203 (2008).

[65] Sylvain Mezil, Francois Bruno, Samuel Raetz, Jérôme Laurent, Daniel Royer, and Claire Prada, “Investigation of interfacial stiffnesses of a tri-layer using Zero-Group Velocity Lamb Modes” J. Acoust. Soc. Am. 138, 3202 (2015).

[66] C. Prada, D. Clorennec, and D. Royer, Power law decay of zero group velocity Lamb modes, Wave Motion 45 (2008).

[67] I. Tolstoy, and E. Usdin, “Wave Propagation in Elastic Plates: Low and High Mode Dispersion”, J. Acoust. So. Am. 29, 1 (1957).

[68] A. L. Shuvalov, and O. Poncelet, “On the backward Lamb waves near thickness resonances in anisotropic”, Int. J. Solids Struct. 45, (2008).

[69] M. Germano, A. Alippi, A. Bettucci, and G. Mancuso, “Anomalous and negative reflection of Lamb waves in mode conversion”, Phys. Rev. B 85, 012102 (2012).

[70] I. A. Veres, C. Grunsteidl, D. M. Stobbe, and T. W. Murray, “Broad angle negative reflection and focusing of elastic waves from a plate edge,” Phy. Rev. B. 93, 174304 (2016).

[71] B. Gérardin, J. Laurent, C. Prada, and A. Aubry, "Negative reflection of Lamb waves at a free edge: Tunable focusing and mimicking phase conjugation," J. Acoust. Soc. Am. 140, 591 (2016).

[72] J. B. Pendry and S. A. Ramakrishna, "Focusing light using negative refraction," 2003 J. Phys. Condens. Matter 15 6345.

[73] T. J. Delph, G. Herrmann, and R. K. Kaul, On coalescence of frequencies and conical points in the dispersion spectra of elastic bodies, Int. J. Solids Struct. 13, 423 (1977).

[74] D. M. Stobbe and T. W. Murray, "Conical dispersion of Lamb waves in elastic plates," Phys. Rev. B 96, 144101 (2017).

[75] D. M. Stobbe and T. W. Murray, "Scattering of Lamb waves with conical dispersion in elastic plates", In Progress (2018).

Chapter 2

Lamb Wave Theory

2.1 Introduction

This Chapter introduces the necessary physics and mathematics for studying Lamb waves with conical dispersion at zero wavenumber (k). First, the dispersion of Lamb waves is examined in order to identify regions where conical dispersion at $k = 0$ can be induced, and then the mechanisms for such occurrences are discussed. This leads to the classification and mathematical description of the simple thickness resonance modes. It is shown how coincident simple thickness resonances of the same symmetry lead to conical dispersion at $k = 0$. It will also be shown how the group velocity of a Lamb wave at $k = 0$ can be calculated based on the displacement and stress mode shapes. Next, the response of a plate with conical dispersion at $k = 0$ to an impulsive force is calculated and analyzed. Finally, some of the numerical methods used in the manuscript are introduced.

2.2 Lamb wave dispersion curves

The geometry and boundary conditions for a free plate of infinite extent is illustrated in Fig. 2.1.

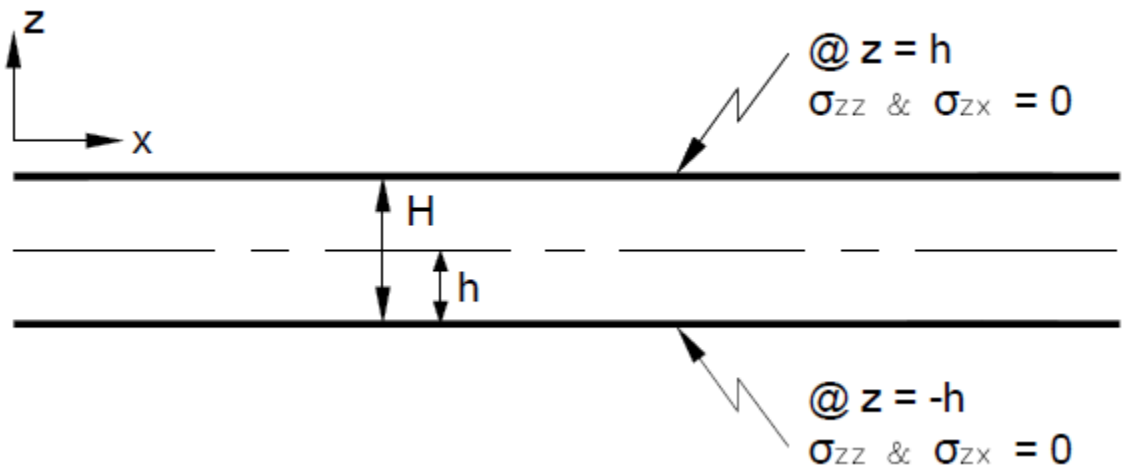

Fig. 2.1 Geometry of the 2-dimensional fee plate problem.

For the case of plane strain, vibration of a free plate consisting of homogenous isotropic linear elastic material results in wave motion according to Eq. 2.1 [1]:

$$u_p = \bar{\Gamma}_p(z,k,\omega)e^{i(kx-\omega t)} \quad (p = x,z), \qquad \text{Eq. 2.1}$$

where ω and *k* are frequency and wavenumber, respectively, and $\bar{\Gamma}_p$is a complex function of z, *k*, and ω. This solution, for a given ω and *k*, represents a traveling wave in the *x*-direction whose magnitude and phase depends on a "static" function of *z*. The static function through the plate thickness (*z*) is often referred to as a transverse resonance or mode shape [1]. The relationship ω(*k*) or *k*(ω) is given by solution of the Rayleigh-Lamb frequency equation [2,3]:

$$\frac{\tan\left(\sqrt{\left(\frac{\omega^2}{{c_T}^2}-k^2\right)}h\right)}{\tan\left(\sqrt{\left(\frac{\omega^2}{{c_L}^2}-k^2\right)}h\right)} = -\frac{4k^2\sqrt{\left(\frac{\omega^2}{{c_T}^2}-k^2\right)}\sqrt{\left(\frac{\omega^2}{{c_L}^2}-k^2\right)}}{\left(\frac{\omega^2}{{c_T}^2}-2k^2\right)^2} \qquad \text{(Eq. 2.2)} \qquad \text{for symmetric modes and}$$

$$\frac{\tan\left(\sqrt{\left(\frac{\omega^2}{{c_T}^2}-k^2\right)}h\right)}{\tan\left(\sqrt{\left(\frac{\omega^2}{{c_L}^2}-k^2\right)}h\right)} = -\frac{\left(\frac{\omega^2}{{c_T}^2}-2k^2\right)^2}{4k^2\sqrt{\left(\frac{\omega^2}{{c_T}^2}-k^2\right)}\sqrt{\left(\frac{\omega^2}{{c_L}^2}-k^2\right)}} \qquad \text{(Eq. 2.3)} \qquad \text{for antisymmetric modes.}$$

Where c_L and c_T are the longitudinal wave velocity and shear wave velocity, respectively. Symmetric and antisymmetric describe the normal displacement (*z*-direction) of the plate relative to the mid-plane, as depicted in Fig 2.2.

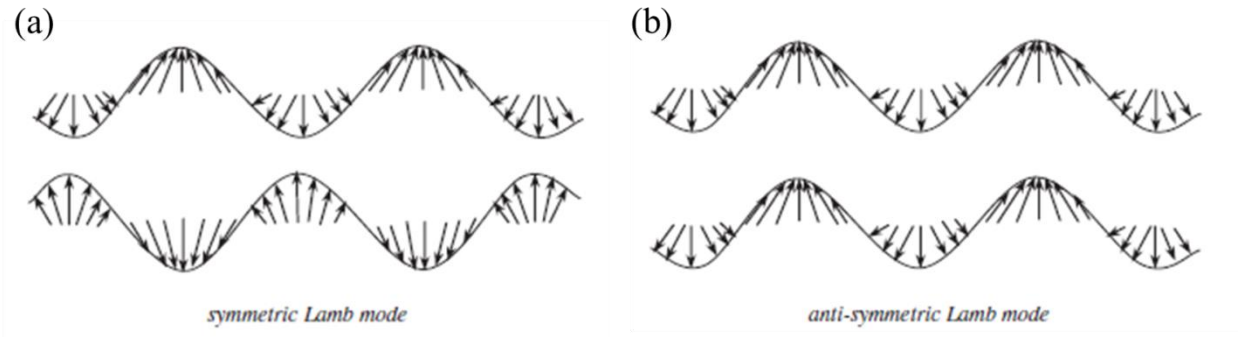

Fig. 2.2 Pictorial representation of (a) symmetric and (b) anti-symmetric vibration of a plate.

Equations 2.2 and 2.3 are transcendental equations which relate ω and k given c_T, c_L, and h. For real positive values of ω there are an infinite number of k's which satisfy Eq. 2.2 and 2.3: a finite number of real, a finite number of purely imaginary, and an infinite number of complex [4]. Real *k* represent undamped waves traveling in the *x*-direction, complex *k* represent evanescent or decaying waves traveling in the *x*-direction, and imaginary *k* represent non-propagating waves

with exponential decay in the *x*-direction. The solutions of Eq. 2.2 or 2.3 occur as continuous curves in the range of ω = 0 to ω = ∞, where the domain of *k* for each curve is the complex plane. The first 9 mode curves for real ±*k* are shown in Fig. 2.3, where the solution was obtained with the numerical method detailed in Section 2.6.

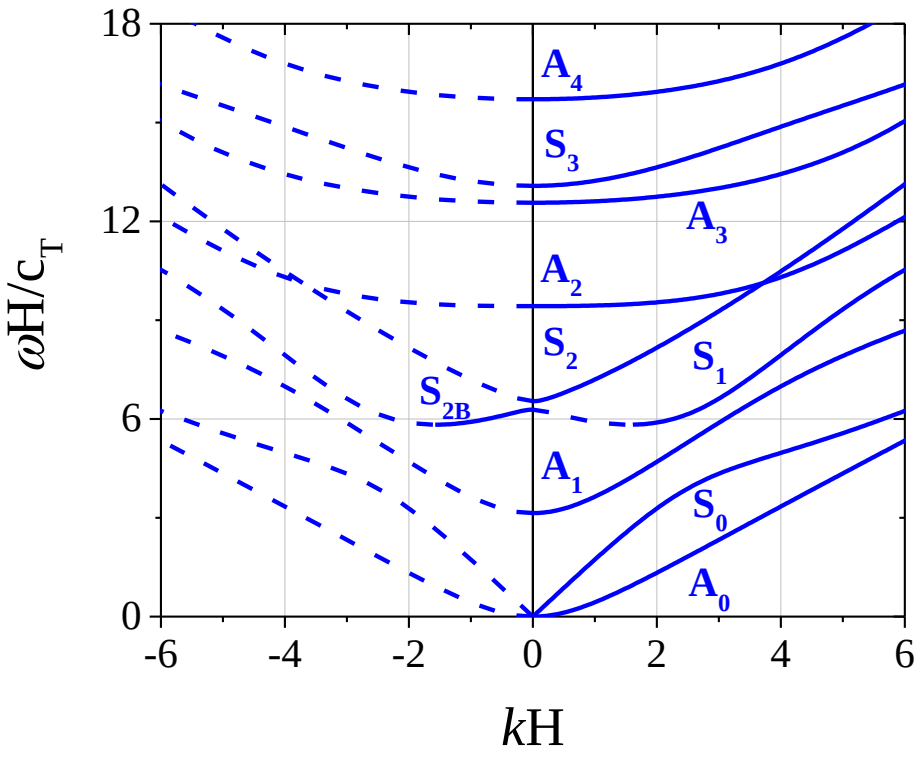

Fig. 2.3 Dispersion curves for Lamb waves in a plate with Poisson's ratio = 0.35.

The individual curves in Fig. 2.3 are labeled in ascending order from 0 and labeled with an A or S according to their displacement symmetry as defined in Fig. 2.2. The dispersion curves in Fig. 2.3 elucidate many features of wave propagation in a plate with consideration of the definitions for a wave's phase velocity (c_p) and group velocity (c_g):

$$c_p = \frac{\omega}{k} \quad and \quad c_g = \frac{d\omega}{dk}. \qquad \text{Eq. 2.4}$$

Phase velocity defines the velocity of a stationary phase whereas c_g defines the velocity at which energy propagates away from the source [4]. Examining the slopes of the mode curves (c_g) it is observed that the dashed curves in Fig. 2.3 represent energy flow in the –*x*-direction and the solid lines represent energy flow in the +*x*-direction. In general, the +*x* traveling waves have a +*k*, meaning that the wave fronts travel in the same direction as the energy flow. However, for the region labeled with a "B" subscript, the phase and group velocity are opposite signed. In such cases the wave fronts travel backward with respect to the energy flow. This type of non-intuitive wave behavior has been studied in literature [5-11] and by this author in [12] and Appendix A. It is also observed that at $k = 0$ the modes all exhibit zero curvature. In the vicinity of $k = 0$ the dispersion curves are parabolic [13] (with the exception of the S_0 mode, however the S_0 mode crosses $k = 0$ at $\omega = 0$, which is the trivial case of no motion). This means that at $k = 0$ Lamb waves are generally not propagating waves but rather are stationary resonances. These resonances are called simple thickness mode resonances [14] or simple thickness resonances. They occur at frequencies called the cutoff frequencies and are the topic of the next section. Examining Eq. 2.4 it is clear that if a dispersion curve has a linear slope, c_p and c_g are equal, and the waves are non-dispersive. If a mode curve is not linear, which is generally the case, the degree of dispersion is proportional to the curvature [14]. It was previously stated that each dispersion curve is a continuous line ranging from $\omega = 0$ to $\omega = \infty$, however, this is not immediately clear in Fig. 2.3. In order to fully visualize the dispersion behavior of an individual mode curve it can be helpful to observe the wavenumber over the entire complex plane, as shown for the first 3 symmetric modes in Fig. 2.4 [5]. Following the S_0 mode in Fig. 2.4, for increasing ω starting at $\omega = 0$, k is real for all ω.

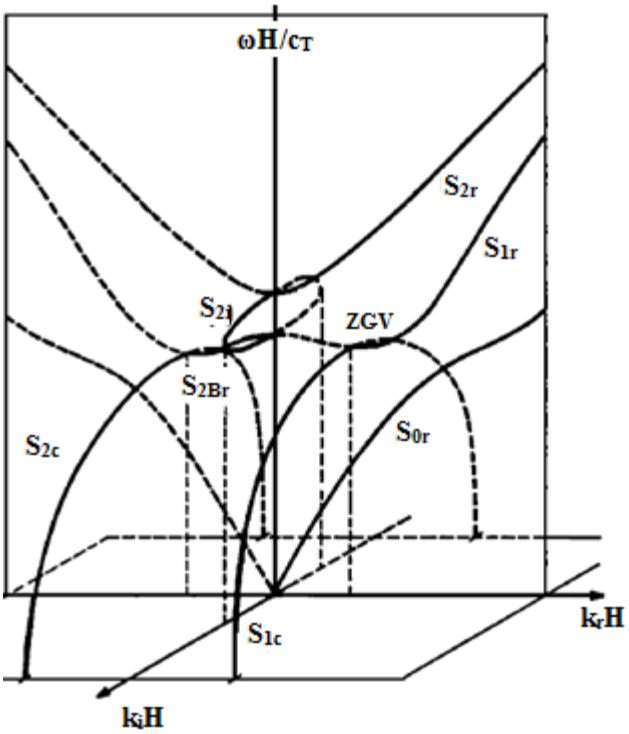

Fig. 2.4 Frequency dispersion for first 3 symmetric modes including complex wave numbers.

The S_1 mode, however, starts out with a complex k at $\omega = 0$ and approaches the real plane with increasing ω. The S_1 mode then becomes real at the point labeled ZGV, and then remains real with increasing ω. The S_2 mode curve is particularly interesting because it crosses $k = 0$ twice. The S_2 mode begins with complex k at $\omega = 0$ and the real part is initially negative. The mode curve then approaches the real plane with increasing ω, and k becomes real and negative at the mirror point of ZGV (not labeled). From this point k is real and negative and the mode curve has a positive slope. This section of the S_2 mode exhibits backward wave motion and accordingly is labeled with a "B" subscript [5]. The backward wave portion of the S_2 mode ends at the lower of the two points where $k_r = 0$. The lower and upper $k_r = 0$ points are connected via a purely imaginary k loop. After this point, k is real and positive with increasing ω. Interestingly, the

aforementioned imaginary loop can close if the two $k_r = 0$ points become coincident (degeneracy). This condition will be shown to cause linear dispersion at $k = 0$ instead of the usual parabolic dispersion and result in Lamb waves that propagate with a finite c_g and an infinite wavelength (λ).

2.3 Degeneracy of Simple Thickness Mode Resonances

Although the specific numerical values of the dispersion curves depend on the plate's elastic properties and thickness, the shape of the mode curves are uniquely defined solely by Poisson's ratio (ν) (or a ratio of c_L and c_T, since ν is uniquely defined by c_L/c_T as shown in Eq. 2.5).

$$\nu = \frac{{c_L}^2 - 2{c_T}^2}{2({c_L}^2 - {c_T}^2)} = \frac{\left({}^{c_L}/_{c_T}\right)^2 - 2}{2\left(\left({}^{c_L}/_{c_T}\right)^2 - 1\right)}. \quad \text{Eq. 2.5}$$

Another feature of the dispersion curves in Fig. 2.3 is that mode curves of the same symmetry cannot cross one another [4]. Similarly, no one mode curve can cross itself. In fact, mode curves of the same symmetry will repel one another when proximate [15,16]. This phenomenon occurs, for example, in the S_2 mode near $k = 0$. Fig. 2.5 shows the S_2 mode near $k = 0$ for 3 different values of ν. Specifically, Fig. 2.5 shows the cases of strong interaction ($\nu = 0.34$), weak interaction ($\nu = 0.40$), and no interaction ($\nu = 0.46$). Fig. 2.5 demonstrates that the existence of a backward propagating portion of the S_2 mode is a result of the repulsion between the S_{2B} and S_2 curves at $k = 0$. The closeness of these two points is set by the frequencies of the longitudinal and transverse simple thickness mode resonances.

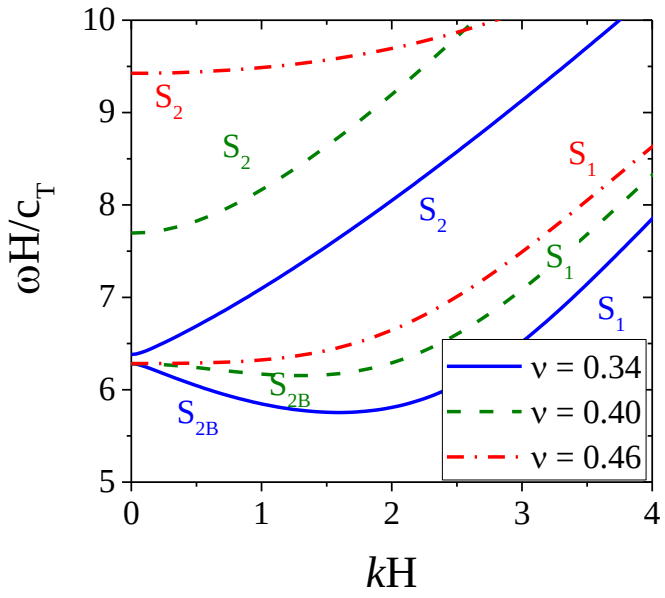

Fig. 2.5 Frequency dispersion of S_2 mode and S_1 mode for ν = 0.34, 0.40, and 0.46, demonstrating the repulsion of mode curves of same symmetry.

These resonances occur at the cutoff frequencies [14]:

$$\omega_{m,L}^{0} = \frac{\pi m c_L}{H} \quad \begin{pmatrix} m = 1,3,5... & symmetric \\ m = 2,4,6... & antisymmetric \end{pmatrix}$$

Eq. 2.6.

$$\omega_{n,T}^{0} = \frac{\pi n c_T}{H} \quad \begin{pmatrix} n = 1,3,5... & antisymmetric \\ n = 2,4,6... & symmetric \end{pmatrix}$$

Here, L and T are longitudinal or transverse (shear) and H is the plate thickness. These resonances are each a result of a bulk wave modes (longitudinal or shear vertical) reflecting normally between the top and bottom faces of the plate. The interaction of proximate resonances can be described mathematically by considering the dispersion branches in the vicinity of $k = 0$ and expanding $\omega(k)$ in even powers, which preserves time reversal symmetry, giving [8]:

$$\omega_{m,\alpha}(k) = \omega_{m,\alpha}^{0} + \frac{1}{2}\left(\frac{\partial^2 \omega_{m,\alpha}}{\partial k^2}\right)_{k=0} k^2 + O\left(k^4\right), \qquad \text{Eq. 2.7}$$

where α corresponds to either a longitudinal or transverse simple thickness mode resonance and the curvatures in the long wavelength limit are given by [8]:

$$\begin{aligned}\left(\frac{\partial^2 \omega_{m,L}}{\partial k^2}\right) &= \frac{c_L h}{\pi m} + \frac{16 h c_T^3}{\pi^2 m^2 c_L^2} \tan\left(\frac{\pi m}{2}\left(1 - \frac{c_L}{c_T}\right)\right) \\ \left(\frac{\partial^2 \omega_{n,T}}{\partial k^2}\right) &= \frac{c_T h}{\pi n} + \frac{16 h c_T^2}{\pi^2 n^2 c_L} \tan\left(\frac{\pi n}{2}\left(1 - \frac{c_T}{c_L}\right)\right)\end{aligned} . \qquad \text{Eq. 2.8}$$

The first term in Eq. 2.7 is the cutoff frequency, as defined by Eq. 2.6, and the following terms describe the curvature of mode at $k = 0$. Consider the curvatures of the first longitudinal simple thickness resonance ($m = 1$), the first and second symmetric transverse thickness resonance ($n = 2$ and $n = 4$), and the second and third antisymmetric transverse thickness resonances ($n = 3$ and $n = 5$). The normalized curvatures are plotted as a function of c_L/c_T (or ν) in Fig. 2.6. The curvatures in Fig. 2.6 show that the resonances $m = 1$ and $n = 2$ interact around $c_L/c_T = 2$ and are both divergent at $c_L/c_T = 2$ ($\nu = \frac{1}{3}$). The curvatures of $m = 1$ and $n = 4$ interact around $c_L/c_T = 4$ and are both divergent at $c_L/c_T = 4$ ($\nu = \frac{14}{30}$). The curvature of m = 1 never interacts with n = 3 or n = 5, even when these curvatures are divergent at $c_L/c_T = 1.5$ and $c_L/c_T = 2.5$, respectively. This shows that modes of different symmetry do not interact with one another. Interestingly, the condition for two resonances curvatures to be simultaneously divergent is also the condition for coincidence and degeneracy. In general, in cases where the ratio of the wave velocities is equal to the irreducible ratio of two positive integers of different parity (one odd and one even)

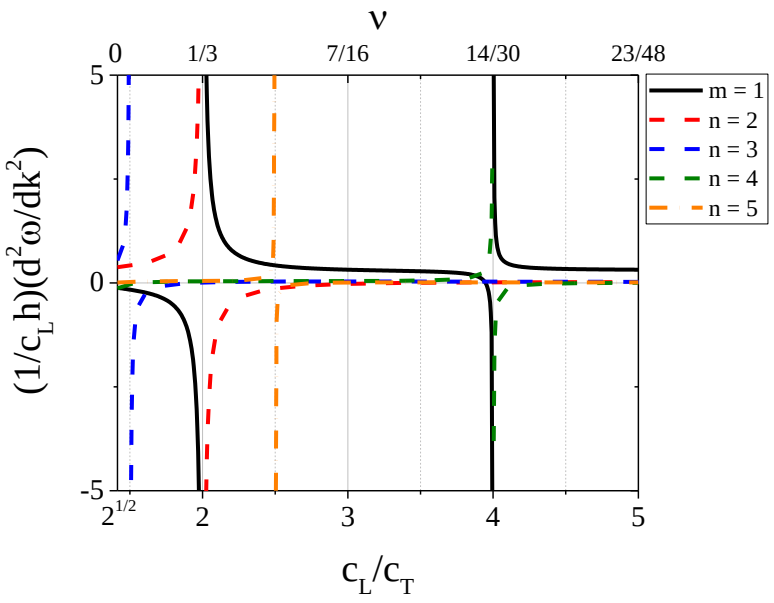

Fig. 2.6 (a) Curvature of the dispersion curves for first symmetric longitudinal thickness resonance (m = 1), the first and second symmetric shear thickness resonances (n = 2 and n = 4), and the second and third antisymmetric shear thickness resonances (n = 3 and n =5).

degeneracy between longitudinal and transverse simple thickness resonances of the same symmetry occurs [14]. In such circumstances the expansion in Eq. 2.7 is no longer valid. In the case of coincident resonances of same symmetry, Mindlin showed that the slope of the dispersion curve is nonzero at $k = 0$ and the local dispersion assumes the linear form [14]:

$$\omega_{m,\alpha}(k) = \omega_{m,\alpha}^{0} \pm \left(\frac{\partial \omega_{m,\alpha}}{\partial k} \right)_{k=0} k, \qquad \text{Eq. 2.9}$$

where the group velocity is given by:

$$c_g = \left(\frac{\partial \omega_{m,\alpha}}{\partial k} \right)_{k=0} = \frac{4c_T}{\pi n}. \quad n = 2,3,4... \qquad \text{Eq. 2.10}$$

The dispersion curves here consist of two lines intersecting at the coincidence frequency and k = 0, with the line segments above $\omega_{m,\alpha}^{0}$ exhibiting forward wave propagation, and the line segments below showing backward wave propagation. The presence of two lines in the degenerate case ensures that $\omega(k) = \omega(-k)$, which again is required by time reversal symmetry. In general, conical dispersion of Lamb waves is associated with closing the imaginary loop of individual modes that exhibit both longitudinal and shear thickness resonances. In the next Section the mechanism for energy transmission (non-zero c_g) in such a case is calculated and physically explained by examination of the displacement and stress fields.

2.4 Linear dispersion from degeneracy of simple thickness mode resonances of like symmetry

In Section 2.3 it was stated that simple thickness resonances are degenerate when the ratio of the wave velocities is equal to the irreducible ratio of two positive integers of different parity. Fig. 2.6 illustrated that the parabolic curvature of the dispersion curves was no longer valid in these cases and instead linear dispersion occurred according to Eq. 2.9 and Eq. 2.10. Here, the mode shapes of the simple thickness resonances are examined and the physics of why conical dispersion at k = 0 occurs in the degenerate case is explained.

The simple thickness resonances arise from a longitudinal or shear wave normally reflecting from the interfaces at $z = \pm h$ [14]. For longitudinal waves the displacement is in plane with the boundaries and for shear waves the displacement is perpendicular to the boundaries (only the shear vertical wave is considered because the shear horizontal wave does not couple

into the longitudinal wave or the shear vertical wave). Mathematically, the displacement fields are found by solving the equations of elasticity while imposing the boundary conditions shown in Fig. 2.1, and assuming that the strain depends only on the *z* direction [14]:

$$\begin{aligned} u_z &= A\sin\left(\frac{m\pi z}{2h}\right)e^{i\omega_m^o t} \quad for\ odd\ m\ (symmetric) \\ u_z &= B\cos\left(\frac{m\pi z}{2h}\right)e^{i\omega_m^o t} \quad for\ even\ m\ (antisymmetric) \end{aligned} \qquad Longitudinal\ Resonances$$

$$\begin{aligned} u_x &= C\sin\left(\frac{n\pi z}{2h}\right)e^{i\omega_n^o t} \quad for\ odd\ n\ (antisymmetric) \\ u_x &= D\cos\left(\frac{n\pi z}{2h}\right)e^{i\omega_n^o t} \quad for\ even\ n\ (symmetric) \end{aligned} \qquad Shear\ Resonances. \qquad \text{Eq. 2.11}$$

Where ω_m^o and ω_n^o are define in Eq. 2.6, *h* is half of the plate thickness, and A, B, C, and D are constants. The mode shapes U_z and U_x for the first symmetric longitudinal mode (m = 1) and the first symmetric shear mode (n = 2) are given by:

$$\begin{aligned} U_x &= 0, \quad U_z = A\sin\left(\frac{\pi z}{2h}\right), \quad for\ m = 1 \\ U_x &= D\cos\left(\frac{\pi z}{h}\right), \quad U_z = 0, \quad for\ n = 2, \end{aligned} \qquad \text{Eq. 2.12}$$

and are shown in Fig. 2.7. Here the longitudinal simple thickness resonance is seen to only have displacement in the *z*-direction and its mode shape is half of a sine cycle. The shear simple thickness resonance only has displacement in the *x*-direction and its mode shape is one cycle of a cosine.

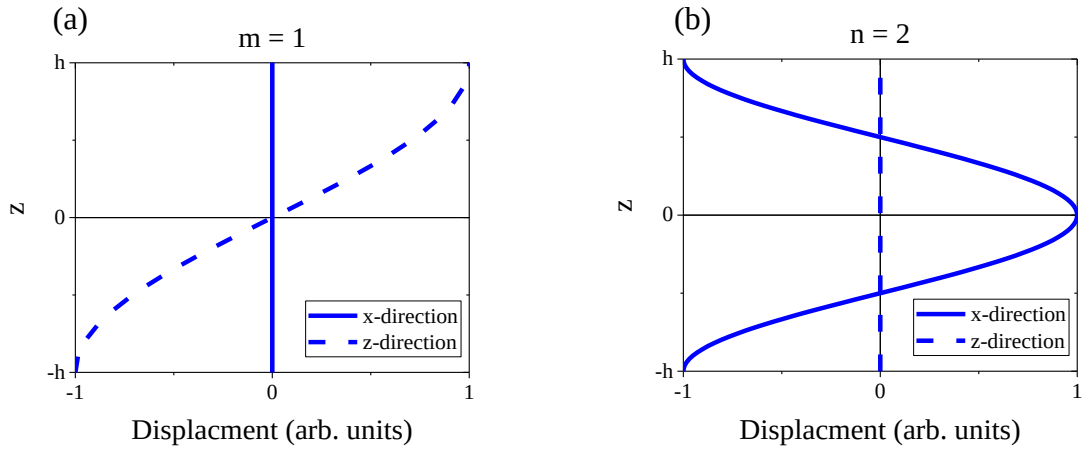

Fig. 2.7 Displacement mode shapes for (a) the first symmetric longitudinal simple thickness mode (m = 1) and (b) the first symmetric shear simple thickness mode (n = 2).

For each of these modes the strain mode shapes E_{xx}, E_{xz}, and E_{zz} are calculated using the strain compatibility equation [1] and are found to be:

$$E_{xx} = 0, \quad E_{xz} = 0, \quad E_{zz} = \left(\frac{A\pi}{2h}\right)\cos\left(\frac{\pi z}{2h}\right), \quad for\ m = 1$$

$$E_{xx} = 0, \quad E_{xz} = -\frac{1}{2}\left(\frac{D\pi}{h}\right)\sin\left(\frac{\pi z}{h}\right), \quad E_{zz} = 0, \quad for\ n = 2. \qquad \text{Eq. 2.13}$$

Next, the stress mode shapes S_{xx}, S_{xz}, and S_{zz} are calculated using the constitutive equations for an isotropic material [1] and are:

$$S_{xx} = \lambda\left(\frac{A\pi}{2h}\right)\cos\left(\frac{\pi z}{2h}\right), \quad S_{xz} = 0, \quad S_{zz} = (\lambda + 2\mu)\left(\frac{A\pi}{2h}\right)\cos\left(\frac{\pi z}{2h}\right), \quad for\ m = 1$$

$$S = 0, \quad S_{xz} = -\mu\left(\frac{D\pi}{h}\right)\sin\left(\frac{\pi z}{h}\right), \quad S_{zz} = 0, \quad for\ n = 2, \qquad \text{Eq. 2.14}$$

where λ and μ are the lame constants. The energy-flux mode shape along the plate (E_x) can be calculated using the following equation [5]:

$$E_x = S_{xx}U_x - S_{xz}U_z \, . \qquad \text{Eq. 2.15}$$

Examining the stress and displacements components in Eq. 2.12 and Eq. 2.14, respectively, for the case where $m = 1$, it can be seen that the first term in Eq. 2.15 is zero since there is no displacement in the x-direction and the second term is also zero since there is no shear stress. Consequently, there is no energy transport in the x-direction. For the case where $n = 2$ the first term in Eq. 2.15 is zero since there is no normal stress in the x-direction and the second term is also zero since there is no displacement in the z-direction, again, there is no energy transport in the x-direction. This confirms the usual parabolic dispersion ($c_g = 0$) at $k = 0$ for these simple thickness resonances, when they occur independently.

Now consider a plate where $c_L = 2c_T$ and thus the first symmetric longitudinal simple thickness mode ($m = 1$) and the first symmetric shear simple thickness mode ($n = 2$) occur at the same frequency: $\omega^o_{1,L} = \omega^o_{2,T} = \frac{\pi c_T}{h}$. Here, by superposition, the displacement and stress mode shapes are:

$$U_x = D\cos\left(\frac{\pi z}{h}\right), \quad U_z = A\sin\left(\frac{\pi z}{2h}\right), \quad and$$
$$S_{xx} = \lambda\left(\frac{A\pi}{2h}\right)\cos\left(\frac{\pi z}{2h}\right), \quad S_{xz} = -\mu\left(\frac{D\pi}{h}\right)\sin\left(\frac{\pi z}{h}\right), \quad S_{zz} = (\lambda + 2\mu)\left(\frac{A\pi}{2h}\right)\cos\left(\frac{\pi z}{2h}\right). \qquad \text{Eq. 2.16}$$

Using Eq. 2.15 the energy-flux mode shape can be calculated and is non-zero as shown in Fig. 2.8:

$$E_x/_{AD} = \left(\frac{\lambda\pi}{2h}\right)\cos\left(\frac{\pi z}{h}\right)\cos\left(\frac{\pi z}{2h}\right) + \left(\frac{\mu\pi}{h}\right)\sin\left(\frac{\pi z}{h}\right)\sin\left(\frac{\pi z}{2h}\right). \qquad \text{Eq. 2.17}$$

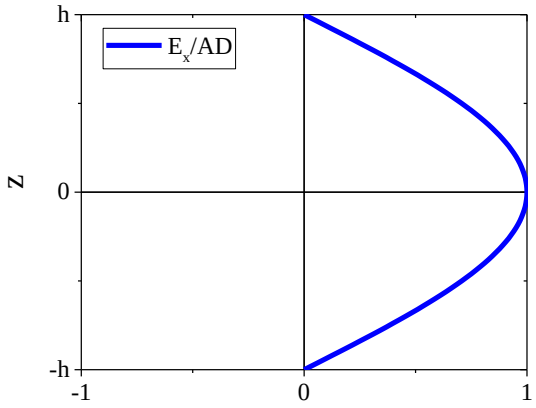

Fig. 2.8 Energy-flux density mode shape at $k = 0$ in the x direction for coincident simple thickness resonances $m = 1$ and $n = 2$.

Examining Eq. 2.15 and Fig. 2.8 it can be seen that the displacement and stress fields from each simple thickness mode resonance interact with one another in order create the energy flow along the wave guide. Each simple thickness resonance on their own does not propagate energy, however when simple thickness resonances of the same symmetry are coincident, there is energy propagation due to the interaction between the displacement and stress of each resonance with one another. It is observed that there is no energy flow if the resonances are of different symmetry when the same procedure as detailed above is followed.

For periodic elastic waves propagating in wave guides, Biot [17] showed that the energy propagates at $d\omega/dk$ (c_g) along the direction of the wave guide. As such, it should be possible to obtain the same Mindlin slopes in Eq. 2.10 by considering the velocity of energy transport. Here,

we consider the case where $c_L = 2c_T$, $m = 1$, and $n = 2$. The velocity of energy transmission in the x-direction is the ratio of the time average power over the time average total energy: [4]

$$c_e = \frac{\frac{1}{T}\int_0^T\left(-1\int_{-h}^{h}(\sigma_{xx}\dot{u}_x+\sigma_{xz}\dot{u}_z)dz\right)dt}{\frac{1}{T}\int_0^T\left(\int_{-h}^{h}\rho(\dot{u}_x^2+\dot{u}_z^2)dz\right)dt}. \qquad \text{Eq. 2.18}$$

For symmetric longitudinal and symmetric shear simple thickness resonances with unit amplitude the displacement components are:

$$\begin{aligned} u_x &= \cos\left(\frac{\pi z}{h}\right)\cos(\omega t) \\ u_z &= \sin\left(\frac{\pi z}{2h}\right)\sin(\omega t) \end{aligned}. \qquad \text{Eq. 2.19}$$

The stress components in Eq. 2.18, with consideration that the displacement functions have no x-direction dependency, are:

$$\begin{aligned} \sigma_{xx} &= \lambda\frac{\partial u_z}{\partial z} = \lambda\frac{\pi}{2h}\cos\left(\frac{\pi z}{2h}\right)\sin(\omega t) \\ \sigma_{xz} &= \mu\frac{\partial u_x}{\partial z} = -\mu\frac{\pi}{h}\sin\left(\frac{\pi z}{h}\right)\cos(\omega t) \end{aligned}. \qquad \text{Eq. 2.20}$$

The velocity components in Eq. 2.18 are:

$$\begin{aligned} \dot{u}_x &= -\omega\cos\left(\frac{\pi z}{h}\right)\sin(\omega t) \\ \dot{u}_z &= \omega\sin\left(\frac{\pi z}{2h}\right)\cos(\omega t) \end{aligned}. \qquad \text{Eq. 2.21}$$

The numerator in Eq. 2.18 can be found by substitution of Eq. 2.20 and Eq. 2.21:

$$\begin{aligned} &\frac{1}{T}\int_0^T\left(-1\int_{-h}^{h}\begin{bmatrix}\left(-\lambda\omega\frac{\pi}{2h}\cos\left(\frac{\pi z}{2h}\right)\cos\left(\frac{\pi z}{h}\right)\sin^2(\omega t)\right)+ \\ \left(-\mu\omega\frac{\pi}{h}\sin\left(\frac{\pi z}{2h}\right)\sin\left(\frac{\pi z}{h}\right)\cos^2(\omega t)\right)\end{bmatrix}dz\right)dt = \\ &\frac{1}{T}\int_0^T\left(\omega\left[\frac{2\lambda}{3}\sin^2(\omega t)+\frac{8\mu}{3}\cos^2(\omega t)\right]\right)dt \qquad \{\lambda = 2\mu = 2\rho c_T^2\} \\ &2\rho\omega c_T^2\frac{1}{T}\int_0^T 1dt = 2\rho\omega c_T^2 \end{aligned}. \qquad \text{Eq. 2.22}$$

The denominator in Eq. 2.18 can be found by substitution of Eq. 2.21:

$$\frac{1}{T}\int_0^T\left(\int_{-h}^{h}\rho\omega^2\left(\cos^2\left(\frac{\pi z}{h}\right)\sin^2(\omega t)+\sin^2\left(\frac{\pi z}{2h}\right)\cos^2(\omega t)\right)\right)dt \\ \frac{1}{T}\int_0^T\left(\rho h\omega^2(\sin^2(\omega t)+\cos^2(\omega t))\right)dt=\rho h\omega^2 \quad \text{Eq. 2.23}$$

Taking the ratio of Eq. 2.22 and Eq.2.23 and using the definition of ω when $m = 1$ and $n = 2$ gives:

$$c_e=\frac{2\rho\omega c_T^2}{\rho h\omega^2}=\frac{2c_T^2}{h\omega} \qquad \left\{\omega=\frac{\pi c_T}{h}\right\} \qquad c_e=\frac{2c_T}{\pi}. \quad \text{Eq. 2.24}$$

Equation 2.24 shows that the velocity of energy transmission, which is equal to c_g, does in fact agree with the value obtained by Mindlin in Eq. 2.10. Mindlin's derivation considered the slope of the dispersion curves when $k \rightarrow 0$. The above derivation does not consider the dispersion equation at all and still arrives at the conclusion that coincident resonances, of the same symmetry, will result in a propagating wave with a finite c_g.

Continuing the analysis of c_g for coincident simple thickness resonances, the dispersion curves for the S_2 mode near $k = 0$ are shown in Fig. 2.9 (a) for a plate with: H = 1.0 mm, $c_T = 3.0$ mm/μs, and $c_L = 6.0$ mm/μs. The S_2 mode is seen to be linear and continuous through $k = 0$ in transition from backward (S_{2B}) to forward (S_2) propagating. The slope of the curve is calculated at $k = 0$ and found to be 1.91 mm/μs. This agrees with the Eq. 2.10 and Eq. 2.24, which give $c_g = (4 \cdot 3.0)/(2 \cdot \pi) \approx 1.91$ mm/μs.

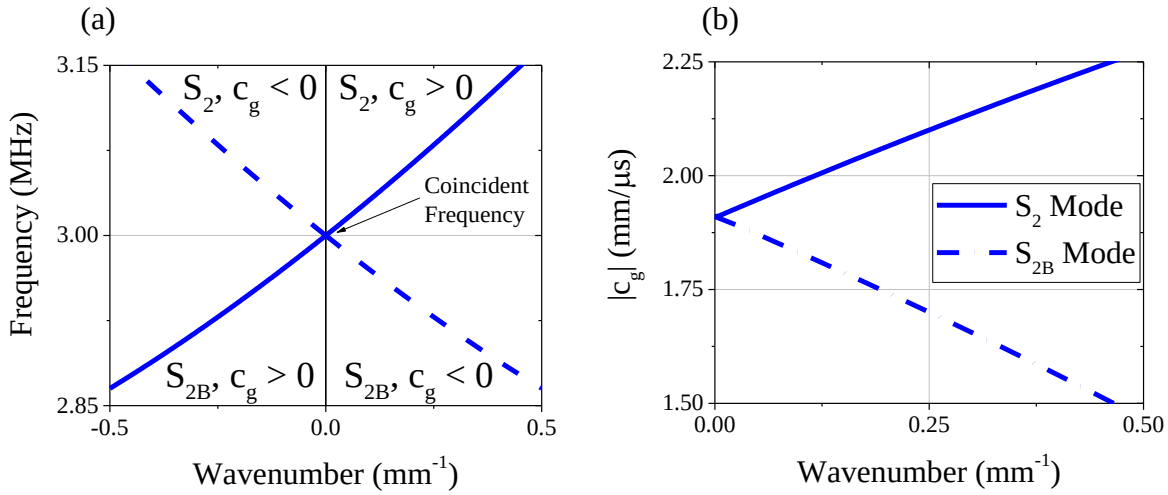

Fig. 2.9 (a) Dispersion curves for the S_2 mode of a plate with H = 1.0 mm, c_T = 3.0 mm/μs, and c_L = 6.0 mm/μs. Linear dispersion is observed at k = 0. (b) Magnitude of group velocity for the S_2 mode and the S_{2B} mode at and near k = 0.

The group velocity curves in Fig. 2.9 (b) show that the linear dispersion is limited to k = 0. Also, the group velocity of the S_2 mode is always larger than the S_{2B} mode except at the coincident point, where they are equal.

This Section demonstrated why coincident simple thickness resonances of like symmetry result in linear dispersion at k = 0 based on an examination of the displacement and stress mode shapes. Also, the Mindlin group velocity equation was re-derived by computation of the velocity of energy transmission for the degenerate case at m = 1 and n = 2. In the next section, the response of a plate, which has conical dispersion, to an impulsive force is studied.

2.5 Plate with conical dispersion at k = 0 response to an impulse

In order to explore the behavior of Lamb waves at and near the conical point, the integral transform technique [18] was used to calculate the normal displacement response of a 1.0 mm thick plate to an impulsive normal force with a Gaussian spatial distribution: full width at half max (FWHM) = 12.5 mm. The temporal profile of the source was also Gaussian with a FWHM of 10 ns, and the wave speeds were selected as c_L = 6.0 and c_T = 3.0 mm/μs (ν = 1/3). Calculations were also performed with a thermoelastic laser source, however, a larger response from the conical mode was observed from a normally applied source. The calculated time domain displacement fields were bandpass filtered between 2.0 MHz and 4.0 MHz to isolate the S_2/S_{2B} mode near 3.0 MHz, the coincident frequency. The resulting waveforms gave the normal displacement as a function of time at several source-to-receiver distances and are shown in Fig. 2.10. In general, the time domain responses show the arrival of two initial wave packets followed by a sustained surface oscillation. The initial wave packets are observed to slightly "stretch" with increased distance from the source due to dispersion. Referring to Fig. 2.9 (b), it is clear that the first wave packet observed in the time traces is the S_2 mode and that the second, slower, packet is the S_{2B} mode.

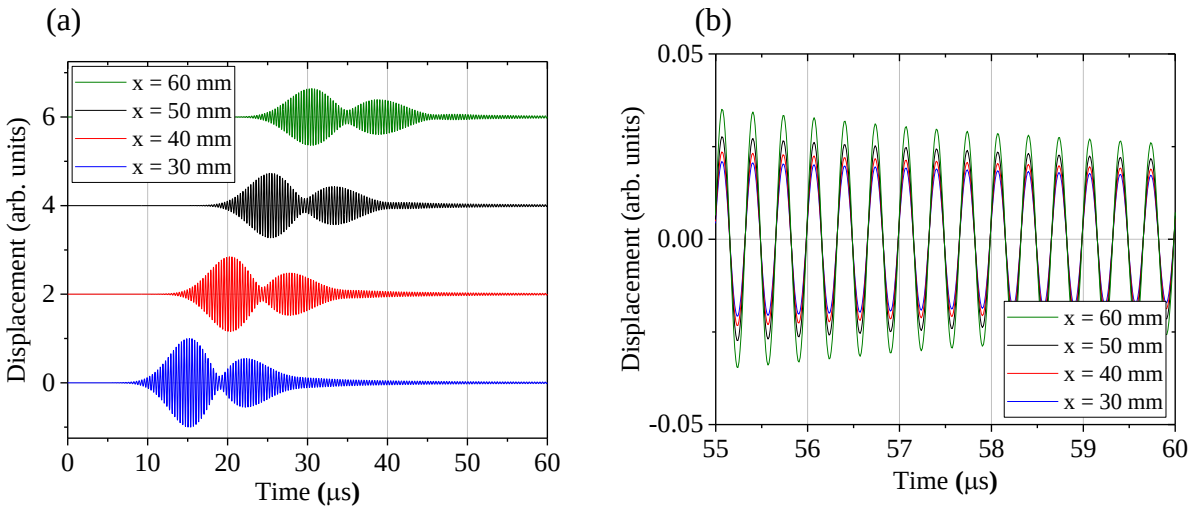

Fig. 2.10 (a) Theoretical surface normal displacement of a plate in response to a normal force. The plate has a thickness of 1 mm and c_L = 6.0 mm/μs and c_T = 3.0 mm/μs. (b) Zoomed in portion of the waveforms shown in (a) over 55 - 60 μs, showing uniform phase.

In between these two packets is the conical point Lamb wave, which, after arriving, results in a sustained surface oscillation. The conical point c_g can be estimated by computing the time lag of the point in between the packets over the 30 mm detection range and is found to be ~ 1.9 mm/μs, which agrees with Eq. 2.10. Observing the time traces in Fig. 2.10 (b) we can see that the sustained surface oscillations are perfectly in phase regardless of spatial location. The magnitude of the Fourier transform of the waveform at source to receiver distance of 30 mm is shown for the entire time window in Fig. 2.11 (a) and for a 55 – 60 μs time window in Fig. 2.11 (b). The spectrum shown in Fig. 2.11 (a) has strong peaks both above (S_2 mode) and below (S_{2B} mode) the conical point with a dip occurring at the coincidence frequency. Additional calculations show that increasing the excitation source size increased the response magnitude at the coincident frequency.

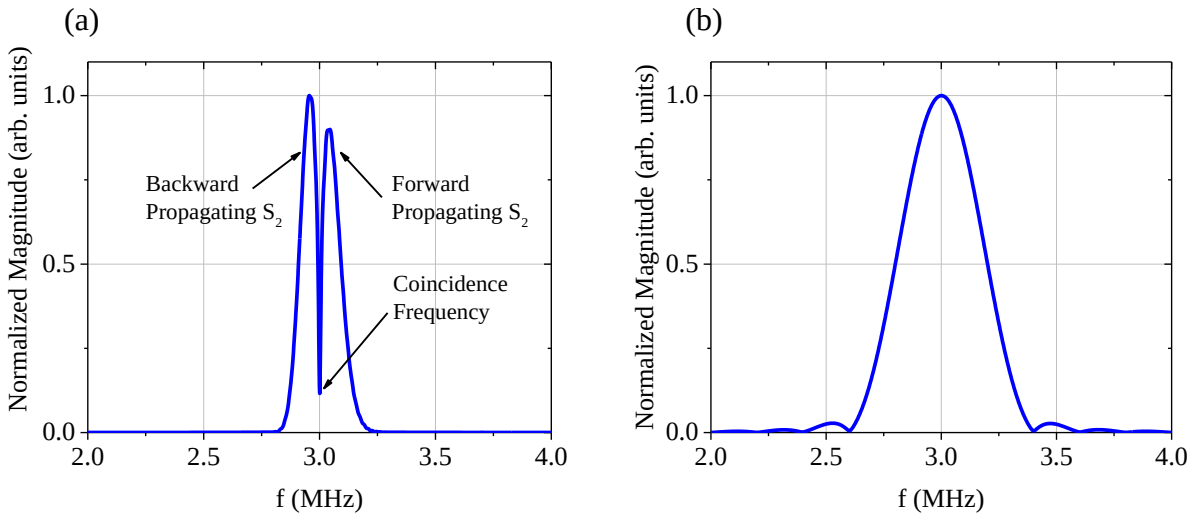

Fig. 2.11 (a) Magnitude of the Fourier transform of the waveform at a source to receiver distance of 30 mm. (b) Magnitude of the Fourier transform of the waveform at a source to receiver distance of 30 mm and time windowed between 55 and 60 μs.

The spectrum in Fig. 2.11 (b) shows that after the initial wave packets pass the detection point the remaining surface oscillations occur at the predicted coincident frequency. This theoretical solution demonstrates that unlike conventional resonances, which have zero c_g at $k = 0$ and slowly decay (depending on the local curvature), conical dispersion at $k = 0$ results in waves that propagate from the source with an infinite wavelength and finite group velocity, producing a spreading spatially uniform temporally oscillating perturbation over the sample surface. Because of this behavior, these waves can be thought of as a type of propagating resonance. This description also follows from the previous modal analysis where the plate vibration is observed to be the superposition of two simple thickness mode resonances.

It is noted here that this theoretical solution was also performed with the time domain finite element simulation software PZFLEX. The numerical simulation was observed to agree with the theoretical solution within numerical noise. The more geometrically complicated experiments

in this manuscript will be compared to numerical simulations since they cannot be solved with the integral transform technique.

2.6 SAFE Method

The Rayleigh-Lamb frequency equation (Eq. 2.2. and Eq. 2.3) is transcendental and the roots must be extracted numerically. An alternative method for solving the free plate problem and calculating the dispersion curves is to use an extended Ritz technique or semi-analytical finite element (SAFE) model [19-23]. For the case of plane strain, the plate can be discretized into finite elements along a line through the thickness (*z*-direction) as shown in Fig. 2.12.

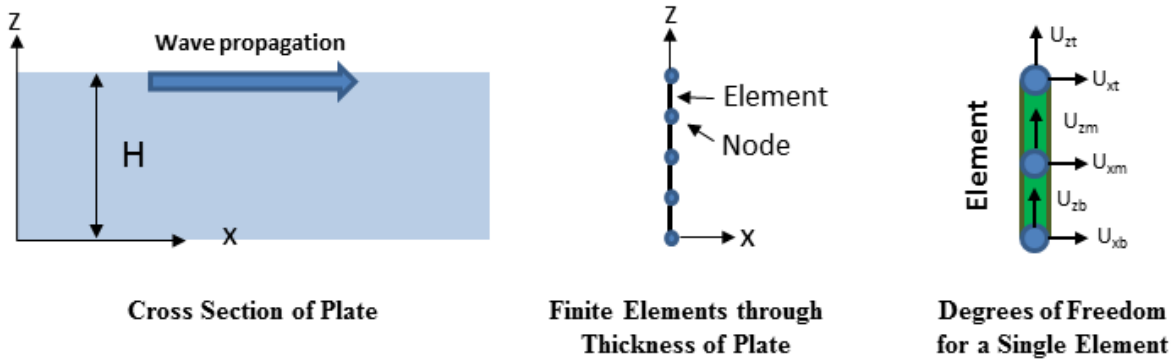

Fig. 2.12 Discretization of plate for solution using a semi-analytical finite element method.

The solution then uses an explicit analytical expression for the traveling waves along the plate (*x*-direction) and unknown mode shapes through the plate thickness (*z*-direction):

$$u_x = U_x(z,t)e^{i(\omega t - kx)} \quad u_z = iU_z(z,t)e^{i(\omega t - kx)}, \qquad \text{Eq. 2.25}$$

with a quadratic interpolation function along each element using three nodes (upper (u), middle (m), and lower (l)):

$$U_j(z,t) = U_{jb}(t)\left[1 - 3\left(\frac{z}{H}\right) + 2\left(\frac{z}{H}\right)^2\right] + U_{jm}(t)\left[4\left(\frac{z}{H}\right) - 4\left(\frac{z}{H}\right)^2\right] + U_{jt}(t)\left[2\left(\frac{z}{H}\right)^2 - \left(\frac{z}{H}\right)\right] \qquad j = x, z. \quad \text{Eq. 2.26}$$

The Lagrangian (L) is then calculated for each element (n) by finding the kinetic (T) and potential (V) energy:

$$\delta L_n = \delta T_n - \delta V_n,$$

$$\delta T_n = \frac{1}{2}\int_0^{2\pi/k}\int_0^H \rho\left(\dot{u_x}^2 + \dot{u_z}^2\right)dzdx,$$

$$\delta V_n = \frac{1}{2}\int_0^{2\pi/k}\int_0^H (C_{11}\varepsilon_{xx}{}^2 + 2C_{12}\varepsilon_{xx}\varepsilon_{zz} + C_{22}\varepsilon_{zz}{}^2 + 4C_{66}\varepsilon_{xz}{}^2)dzdx,$$

$$\delta V_n = \frac{1}{2}\{q_n\}^T[k_n]\{q_n\}, \quad \delta T_n = \frac{1}{2}\{\dot{q_n}\}^T[m_n]\{\dot{q_n}\}, \quad \{q_k\}^T = \{U_{xb}, U_{zb}, U_{xm}, U_{zm}, U_{xt}, U_{zt}\},$$

Eq. 2.27

where k_n and m_n are the element stiffness and mass matrices and C_{11}, C_{12}, C_{22}, and C_{66} are $\lambda+2\mu$, λ, $\lambda+2\mu$, and μ, respectively, for an isotropic material. Summation of the element Lagrangians and application of Hamilton's principal yields the Eigenvalue problem:

$$L = \sum_{n=1}^{num\ elem} (\delta T_n - \delta V_n) = \frac{1}{2}\{\dot{Q}\}^T[M]\{\dot{Q}\} - \frac{1}{2}\{Q\}^T[K]\{Q\},$$

$$[K]\{Q\} + [M]\{\ddot{Q}\} = 0, \quad \{Q\} = \{Q_o\}e^{i\omega t},$$

$$\{[K] - \omega^2[M]\}\{Q_o\} = 0, \qquad \text{Eq. 2.28}$$

where K and M are the total stiffness and mass matrices. The eigenvalues in Eq. 2.28 are the squared frequencies, ω, that solve Eq. 2.2 and Eq. 2.3 for a given k. Each eigenvector, Q_o, is the displacement mode shape for the associated Lamb wave. The above detailed SAFE solution to the free plate plain strain problem was implemented in MATLAB® (Appendix B). All of the dispersion curves shown in this manuscript were generating using this SAFE algorithm. The accuracy of the solution depends on the number elements used. Here, 200 elements were used which gives eigenvalue solutions accurate to $+1.0\text{x}10^{-8}$ % of those found with a root finding routine (taken to accuracy where the values differed). In terms of generating the full frequency dispersion, the SAFE method is several orders of magnitude faster than a root finding routine, of equal precision. The SAFE method can be easily extended to solve multi-layer problems where each layer has independent thicknesses and material properties. Also, the SAFE solution automatically generates the displacement mode shapes, via the eigenvectors, which can then be used to calculate the stress mode shapes and energy flux density through the plate.

2.7 Conclusions

This Chapter details the behavior of Lamb waves at $k = 0$ for an isotropic homogenous plate. Specifically, it was shown that at $k = 0$ the plate vibrations are simple thickness resonances that generally have parabolic dispersion and do not propagate energy along the plate. It was shown, however, that if a shear and longitudinal simple thickness resonance, of the same symmetry, are coincident, the dispersion at $k = 0$ becomes linear and energy does propagate along the plate. One such case was shown to occur when $c_L = 2c_T$ for the first symmetric longitudinal simple thickness resonance and the first symmetric shear simple thickness resonance. For this case the

displacement and stress mode shapes were analyzed and it was shown that the interaction between the two resonances causes the wave to propagate.

The response of a plate with $c_L = 2c_T$ to an impulsive force was analyzed. It was observed that Lamb waves with an infinite wavelength and an infinite phase velocity were generated and propagated at the finite group velocity predicted by Mindlin and by the energy transport analysis. After the initial wave packets passed the observation point, the surface oscillations were observed to be uniform in space. Finally, a numerical method for calculating dispersion curves and mode shapes was presented.

2.8 References

[1] J. L. Rose, *Ultrasonic Waves in Solid Media* (Cambridge University Press 1999).

[2] L. Rayleigh, "On the free vibrations of an infinite plate of homogenous isotropic elastic matter," Proceedings of the London Mathematical Society, Vol. 20 (1889).

[3] . Lamb, "On Waves in an Elastic Plate," Proc. Roy. Soc. London, Ser. A 93 (1917).

[4] J. D. Achenbach, *Wave Propagation in Elastic Solids* (North-Holland, Amsterdam, 1973).

[5] I. Tolstoy, and E. Usdin, “Wave Propagation in Elastic Plates: Low and High Mode Dispersion”, J. Acoust. So. Am. 29, 1 (1957).

[6] A. H. Meitzler, “Backward-Wave Transmission of Stress Pulses in Elastic Cylinders and Plates”, J. Acoust. So. Am. 38, 835 (1965).

[7] P. L. Marston, “Negative group velocity Lamb waves on plates and applications to the scattering of sound by shells”, J. Acoust. Soc. Am. 38, 835 (1965).

[8] A. L. Shuvalov, and O. Poncelet, “On the backward Lamb waves near thickness resonances in anisotropic”, Int. J. Solids Struct. 45, (2008).

[9] A. A. Maznev and A. G. Every, “Surface acoustic waves with negative group velocity in a thin film structure on silicon”, Appl. Phys. Lett. 95, 011903 (2009).

[10] F. D. Philippe, T. W. Murray, and C. Prada, “Focusing on Plates: Controlling Guided Waves using Negative Refraction”, Sci. Rep. 5, 11112 (2015).

[11] M. Germano, A. Alippi, A. Bettucci, and G. Mancuso, “Anomalous and negative reflection of Lamb waves in mode conversion”, Phys. Rev. B 85, 012102 (2012).

[12] I. A. Veres, C. Grunsteidl, D. M. Stobbe, and T. W. Murray, “Broad angle negative reflection and focusing of elastic waves from a plate edge,” Phy. Rev. B, (2016).

[13] C. Prada, D. Clorennec, and D. Royer, “Power law decay of zero group velocity Lamb modes,” Wave Motion 45 (2008).

[14] R. D. Mindlin, *An Introduction to the Mathematical Theory of Vibrations of Elastic Plates* (World Scientific, Singapore, 2016).

[15] C. Prada, D. Clorennec, and D. Royer, “Local vibration of an elastic plate and zero-group velocity Lamb modes,” J. Acoust. Soc. Am. 124, 203 (2008).

[16] M. Ibanescu, S. G. Johnson, D. Roundy, C. Luo, Y. Fink, and J. D. Joannopoulos, “Anomalous Dispersion Relations by Symmetry Breaking in Axially Uniform Waveguides,” Phys. Rev. Lett. 92, 063903 (2004).

[17] M. A. Biot, “General theorems on the equivalence of group velocity and energy transport,” Phys. Rev. 105 (1957).

[18] J. B. Spicer, A.D.W. McKie, and J.W. Wagner, “Quantitative theory for laser ultrasonic waves in a thin plate,” Appl. Phys. Lett. 57, 1882 (1990).

[19] S. B. Dong and R. B. Nelson, “On Natural Vibrations and Waves in Laminated Orthotopic Plates,” J. Appl. Mech. (1972).

[20] R. B. Nelson and S. B. Dong, “High Frequency Vibrations and Waves in Laminated Orthotropic Plates,” J. Sound Vib. 30 (1973).

[21] S. B. Dong and K. H. Huang, “Edge Vibrations in Laminated Composite Plates,” J. Appl. Mech. 52 (1972).

[22] Z.A.B. Ahmad and U. Gabbert, “Simulation of Lamb wave reflections at plate edges using the semi-analytical finite element method,” Ultrasonics 52 (2012).

[23] I. Bartolia, A. Marzania, F. di Scaleaa, and E. Violab, “Modeling wave propagation in damped waveguides of arbitrary cross-section,” J. Sound Vib. 295 (2006).

Chapter 3

Inducing and Measuring Conical Dispersion of Lamb Waves

3.1 Introduction

Theory predicts that conical dispersion at zero wavenumber (k) will occur in elastic plates whenever simple thickness shear and longitudinal resonances, of the same symmetry, are coincident. The condition for this was detailed in Chapter 2 and was shown to depend only on the elastic properties of the plate. Specifically, conical dispersion at $k = 0$ occurs when the ratio of the longitudinal and shear wave velocities is equal to an irreducible ratio of two positive integers of different parity (one odd and one even) [1]. The general condition for coincident simple thickness resonances, both degenerate and non-degenerate, can be expressed solely in terms of Poisson's ratio (v) [2]:

$$\nu = \frac{m^2-2n^2}{2(n^2-m^2)} \quad where\ m = 1,2,3 \ldots and\ n = 2,3,4 \ldots \tag{3.1}$$

The frequency at which the longitudinal (L) and shear (T) simple thickness resonances occur, in terms of *m* and *n*, respectively, is:

$$\omega^0_{m,L} = \frac{\pi m c_L}{H} \quad \begin{pmatrix} m = 1,3,5... & symmetric \\ m = 2,4,\ 6... & antisymmetric \end{pmatrix}$$

$$\omega^0_{n,T} = \frac{\pi n c_T}{H} \quad \begin{pmatrix} n = 1,3,5... & antisymmetric \\ n = 2,4,\ 6... & symmetric \end{pmatrix} \tag{3.2}$$

Here c_L and c_T are the longitudinal and transverse wave velocities, respectively, and H is the plate thickness. Degeneracy of two coincident simple thickness resonances will occur only if they are of the same symmetry (ie. symmetric or anti-symmetric). Equation 3.2 states that longitudinal resonances are symmetric when *m* is odd and anti-symmetric when *m* is even and shear resonances are symmetric when *n* is even and anti-symmetric when *n* is odd. Equation 3.1 is solved for the first nine combinations of *m* and *n* in Table 3.1.

Table 3.1 Some values of Poisson's ratio at which simple thickness resonances are coincident.

	m = 1	*m = 2*	*m = 3*
n = 2	$\nu = \frac{1}{3}$	Undefined	$\nu = 1\frac{2}{5}$
n = 3	$\nu = \frac{7}{16}$	$\nu = \frac{1}{10}$	Undefined
n = 4	$\nu = \frac{14}{30}$	$\nu = \frac{1}{3}$	$\nu = -\frac{1}{9}$

Examining Table 3.1 it can be seen that one condition for conical dispersion at $k = 0$ is when $\nu = \frac{1}{3}$. Here, the 1st symmetric longitudinal thickness resonance ($m = 1$) and the 1st symmetric shear thickness resonance ($n = 2$) are coincident and degenerate. The 1st anti-symmetric longitudinal resonance ($m = 2$) and the 2nd symmetric shear resonance ($n = 4$) are also coincident when $\nu = \frac{1}{3}$, however, because of the difference in symmetry they are not degenerate. If Table 3.1 were extended it would be seen that when $\nu = \frac{1}{3}$ there are degeneracies between odd m-order longitudinal resonances and $2n$ ordered transverse resonances and non-degeneracy between even m-order longitudinal resonances and $2m$ ordered transverse resonances. Table 3.1 also shows that there are other values of ν that cause degeneracy, for instance, the rows in the 1st column alternate between degenerate and non-degenerate coincidences as $n \to \infty$ and $\nu \to \frac{1}{2}$. In this work we focus on the aforementioned degenerate case at $m = 1$ and $n = 2$. This case is interesting because common engineering materials are known to have ν close to $\frac{1}{3}$ and the group velocity (v_g) at this degeneracy is maximal for a given c_T according to [2]:

$$v_g = \left(\frac{\partial \omega_{m,\alpha}}{\partial k} \right)_{k=0} = \frac{4c_T}{\pi n}. \quad n = 2,3,4... \tag{3.2}$$

Examining Eq. 3.2 it is clear that as n increases v_g decreases, meaning the dispersion curves at $k = 0$ become flatter as n increases. Lamb waves with conical dispersion at $k = 0$ will behave least like typical non-propagating resonances when they not only have linear dispersion at $k = 0$ but also have a large v_g. As such, the remainder of this manuscript will concentrate on conical dispersion at the degeneracy between the 1st symmetric longitudinal thickness resonance and the

1st symmetric shear thickness resonance (S_2-S_{2B} modes) which occurs in homogenous isotropic plates when the material's $\nu = \frac{1}{3}$.

This Chapter will detail the process for selecting a suitable sample for demonstrating Lamb waves with conical dispersion at $k = 0$ and show how that sample's elastic properties were manipulated in order to induce degeneracy. Further, the technique for generating and measuring conical Lamb waves will be shown. And finally experimental and theoretical results will be analyzed in order to understand the behavior of Lamb waves with conical and near conical dispersion at $k = 0$.

3.2 Laser Ultrasonic Measurement of Poisson's Ratio

The first step in measuring Lamb waves with conical dispersion at $k = 0$ was to find a material with $\nu \sim \frac{1}{3}$ and then to tune ν to as close to $\frac{1}{3}$ as possible. This required a technique for very accurately measuring ν. The approach used here was a laser based ultrasonic technique developed by Clorennec *et al* [3]. In this technique a plate is excited with a pulsed laser and a zero-group velocity (ZGV) resonance and a simple thickness mode resonance are measured via optical interferometry. Normal displacement is recorded at the epi-center of the excitation in order to measure the ZGV and thickness resonances. The ratio of these two resonances uniquely defines ν and the numerical value of ν can be deduced from numerical solutions of the Rayleigh-Lamb frequency equation. The literature shows that a thermoelastic excitation from a Gaussian laser source, where the laser spot on the sample has a full width at half max (FWHM) equal to ½ of the S_{2B}/S_1 ZGV's wavelength, effectively excites that ZGV resonance [3-8]. Because the ZGV

resonance is non-propagating, it has a prolonged "ring" time when measured proximate to the source and can be measured with a high quality factor (Q). This excitation was shown to also excite the A_2 simple thickness resonance. Measuring the ratio of these two resonances allows the determination of ν with ±0.2% accuracy [3].

In this work a similar technique was used, however, the ratio of the S_{2B}/S_1 ZGV and S_{5B}/S_4 ZGV resonances was used instead. This change was made because it was observed that the S_{5B}/S_4 ZGV could be excited more efficiently and measured more repeatedly than the A_2 simple thickness resonance, for the samples tested. This observation is consistent with theory when performing this type of laser ultrasonic measurement on a material with $\nu \sim \frac{1}{3}$. The excitability and detection of the S_{5B}/S_4 ZGV resonance exceeds that of the A_2 simple thickness resonance when a plate is excited by a laser impulse and the material's $\nu \sim \frac{1}{3}$ [9].

Here, Lamb waves were excited with a Nd:YAG laser operating at 532 nm with a 10 ns pulse length and a FWHM focused to 3.00 mm on the sample surface. The fluence of the excitation laser was attenuated to just below where sample ablation occurred. The normal displacement was measured on the opposite site of the plate as the source and on epicenter of the source using a Michelson interferometer. The interferometer used a single longitudinal mode frequency doubled Nd:YAG laser with an output of 150 mW. The detection laser was focused on the sample using a 10X microscope objective. The time domain response was measured using a digital oscilloscope where the time window was 100 μs, the sampling frequency was 100 MHz, and the waveforms were averaged 1000 times. The experimental setup for this measurement is shown in Fig 3.1. The foam box in Fig. 3.1 was only used in experiments where ν was measured at cooled temperatures.

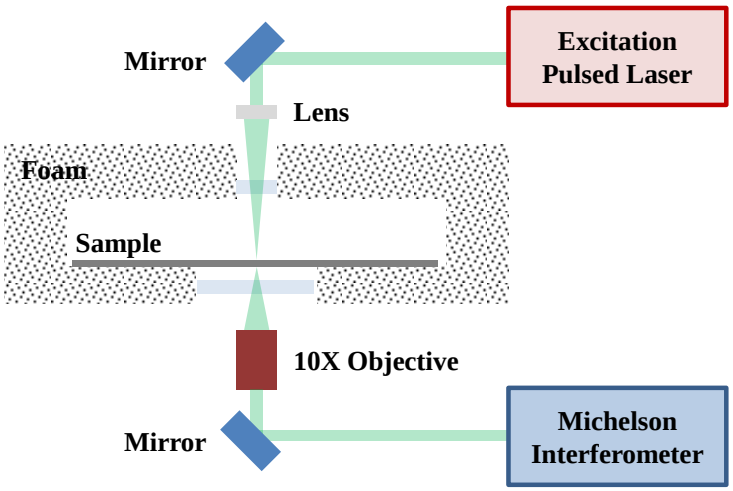

Fig. 3.1 Experimental setup for measuring Poisson's ratio.

A typical time domain response and frequency domain response are shown in Fig. 3.2 for (a) and (b), respectively, after processing by a high pass filter (f = 1.0 MHz). The responses qualitatively agrees with those shown in literature [5,7] for similar experiments.

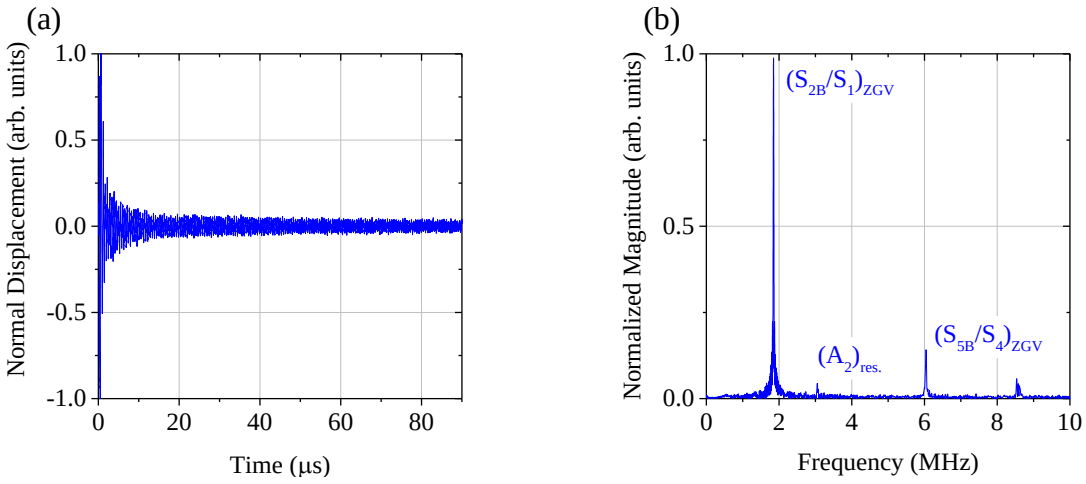

Fig. 3.2 Normal displacement measured at source epicenter due to a laser impulse: (a) time and (b) frequency domains.

The time domain response in Fig. 3.2 (a) confirms the slow temporal decay of the ZGV and simple thickness resonances. The frequency domain response in Fig. 3.2 (b) shows the excited modes and their relative normal displacement response. The S_{2B}/S_1 ZGV mode has the largest response followed by the S_{5B}/S_4 ZGV and then the A_2 simple thickness resonance, which agrees with the literature [9].

The calibration curve for determining ν as a function of the ratio of the S_{5B}/S_4 ZGV frequency and S_{2B}/S_1 ZGV frequency was calculated by solving the Rayleigh-Lamb frequency equation using the SAFE method (Appendix B) for a range of ν (near $\frac{1}{3}$) and then computing the ratio of the aforementioned ZGV frequencies. This calibration curve is shown in Fig. 3.3.

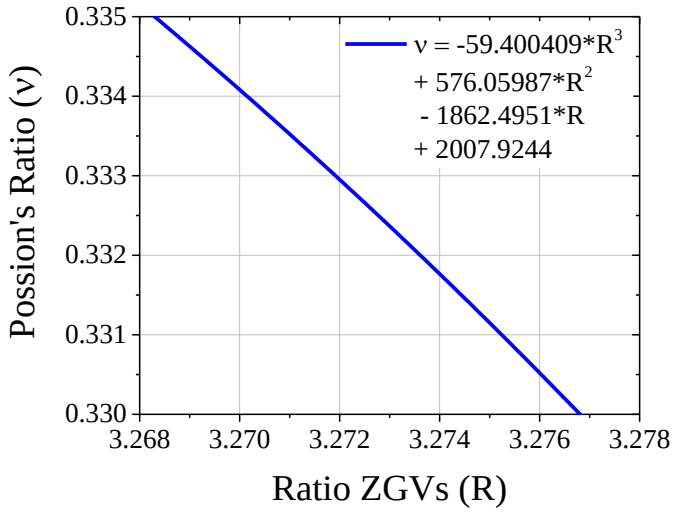

Fig. 3.3 Calibration curve for measuring ν based on the ratio (R) of the S_{5B}/S_4 ZGV frequency and S_{2B}/S_1 ZGV frequency.

The numerical data points were fit with the third-order polynomial shown in Fig. 3.3. For an example of using this technique to measure ν, consider the data in Fig. 3.2. The S_{2B}/S_1 ZGV

frequency and S_{5B}/S_4 ZGV frequency occur at 1.8480 MHz and 6.0439 MHz, respectively, giving an R value of 3.2705. Plugging this R into the equation shown in Fig 3.3 gives a ν of 0.3339. The uncertainty of a single measurement can be calculated using the Q factor of the resonances as shown in the literature [3]. In this study, multiple measurements were performed and a statically approach was used to quantify the error.

Poisson's ratio for plates made from the following aluminum alloys and heat treatments were tested: 1100-O, 2024-O, 2024-T6, 3003, 5052-O, 6061-O, 6061-T6 and 7075-T6. For each sample, ν was measured multiple times at a single location and the mean and standard deviation of the mean was computed. It was determined that 6061-O had a ν closest to $\frac{1}{3}$. For the 6061-O plate, ν was measured using the above detailed technique 30 sequential times at a given location. These 30 measurements were then repeated at 12 randomly chosen locations on the plate. The results of these measurements are shown in Fig. 3.4.

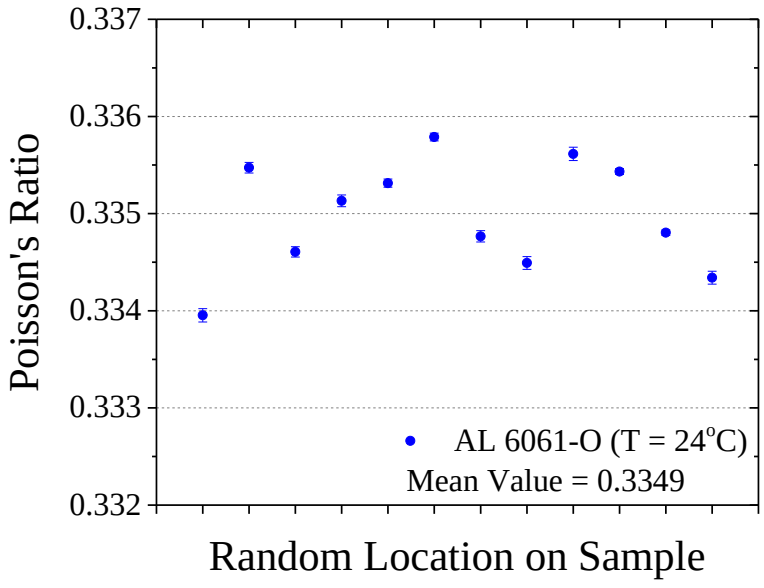

Fig. 3.4. Measurements of Poisson's ratio on 6061-O aluminum plate.

The average value of ν was 0.3349 ± 0.0006, where the experiments were conducted with an average ambient temperature of 24°C. The variation in ν at different measurement locations is due to sample inhomogeny. Sources of local inhomogeny included chemistry, grain texture, and surface residual stress (from forming).

The next step was to modify the elastic properties of the sample so that on average $\nu = \frac{1}{3}$. This was accomplished by changing the temperature of the sample. Specifically, literature [10] states that for pure aluminum $\Delta\nu = 5.4 \cdot 10^{-5} / {}^{o}\Delta C$. Since a 6061 alloy is 95.9 – 98.6 % aluminum [11], it is reasonable to expect that if the sample was cooled ~ 30°C its $\nu \sim \frac{1}{3}$. In order to measure the exact temperature at which the sample's average $\nu = \frac{1}{3}$, the sample was placed into a cooling chamber, as shown in Fig 3.1, and the temperature was decreased to -15°C. Poisson's ratio was then measured, using the ZGV technique, while the temperature slowly returned to 24°C. The results of this measurement are shown in Fig. 3.5. A linear fit to the measurements in Fig. 3.5 yielded: $\Delta\nu = 5.6 \cdot 10^{-5} / {}^{o}\Delta C$. This relationship is similar to that reported in the literature for pure aluminum, which was expected. Using this calibration curve and the average ν measured across the sample, it was calculated that ν will be on average equal $\frac{1}{3}$ at a temperature of -5°C. It should be noted that the data in Fig. 3.5 shows $\nu = \frac{1}{3}$ near 0°C not -5°C. This is because of the variation in ν along the sample, as was shown in Fig. 3.4. At the particular location of the plate that the data in Fig. 3.5 was measured, ν happens to be below the average value for the plate. However, in order to have the sample's ν on average equal $\frac{1}{3}$ the plate should be cooled to -5°C.

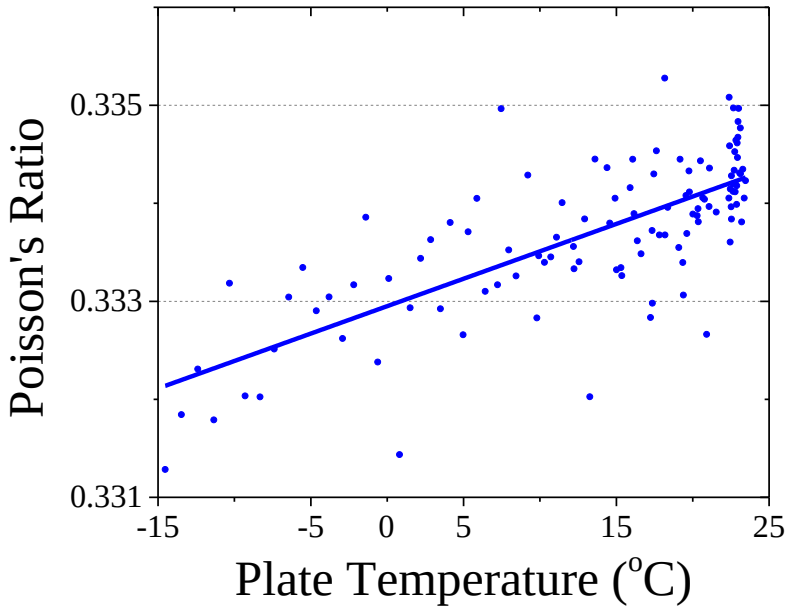

Fig. 3.5 Measurement of Poisson's ratio as a function of temperature for a 6061-O aluminum plate. The solid line shows a linear fit of the data.

3.2 Measurement of Lamb Waves with Conical Dispersion

Conical dispersion was measured in a large 610 x 305 mm 6061-O aluminum plate using the results of the temperature tuning experiment detailed in Section 3.1. This plate had a measured thickness of 1.533 ± 0.003 mm. The plate was cooled to -5°C and the frequency dispersion was measured. This was accomplished by exciting Lamb waves over a narrow frequency band centered on the expected degenerate frequency. Lamb waves were excited by a contact transducer (Olympus v109) with an aperture of 12.7 mm coupled to the sample with a thin oil layer. When electrically driven, the transducer vibrates normal to the aperture plane. This excitation method was selected because theory predicts that the response of the conical mode is

larger for a normal excitation than for a laser thermoselastic excitation, which is primarily a shear excitation. The transducer was driven by a 5 cycle sine wave at 2.04 MHz, from a function generator that was coupled to a 50 dB power amplifier. The resulting normal displacement of the sample was detected using an adaptive photorefractive crystal based interferometer which used a bismuth silicon oxide crystal. A 3.0 kHz, 3.0 kV field was applied to the crystal to enhance two-wave mixing gain, and the laser source for the interferometer was a single longitudinal mode frequency doubled Nd:YAG laser with an output of 150 mW. Further details of the interferometer configuration are available in the literature [12]. The turning mirrors on the signal leg of the interferometer were mounted on a 2-axis translation stage in order to measure the displacement field over the plate surface. The output of the interferometer was sent through a 1.9 MHz analog high pass filter and recorded on a digital oscilloscope at 50 MHz. Time domain responses were measured as the source to receiver distance was increased in 250 μm steps for a total distance of 150 mm, starting 30 mm away from the center of the transducer excitation source. The experimental setup is shown in Fig. 3.6.

The measured waveforms, providing the temporal response as a function of distance, were processed with a two-dimensional fast Fourier transform (FFT) which then gave the temporal frequency as a function of spatial frequency. The magnitude of the response in Fourier space is shown in Fig. 3.7 (a). Here the dispersion curves can be identified as the high magnitude lines in the image. The frequency and wavenumber along these lines was extracted to create experimentally measured dispersion curves which are shown Fig. 3.7 (b) along with the theoretical dispersion curves calculated using the Rayleigh-Lamb frequency equation.

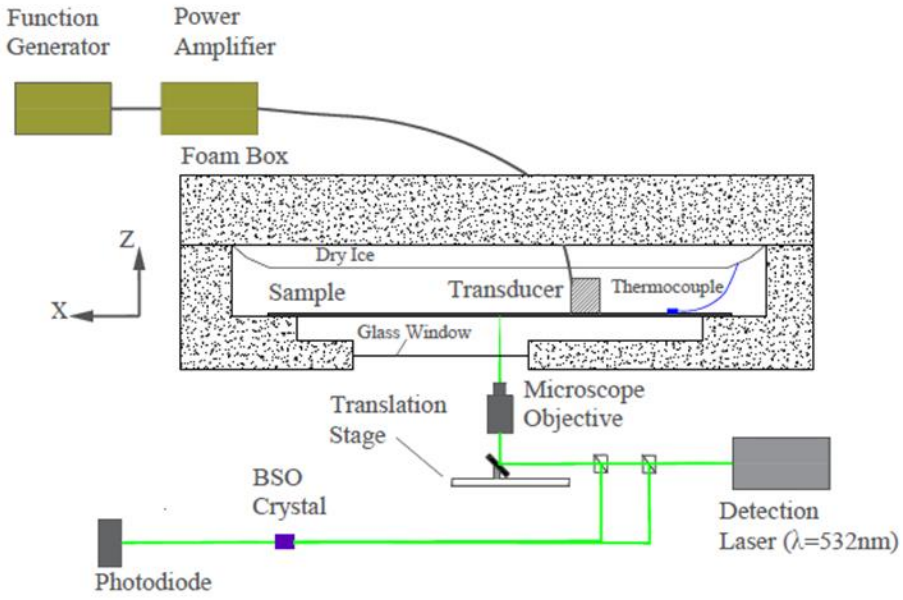

Fig. 3.6 Experimental setup for measuring conical dispersion of Lambs waves.

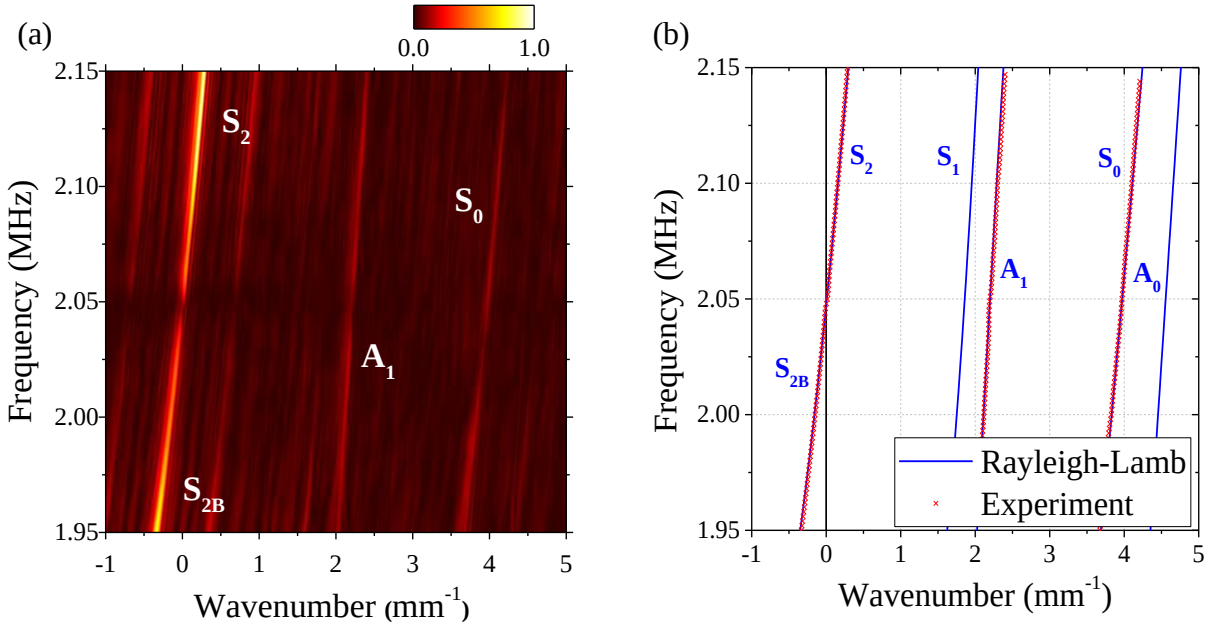

Fig. 3.7 (a) Magnitude plot of the 2D Fourier transform of the experimentally measured waveforms showing the temporal frequency as a function of spatial frequency. (b) Experimentally measured dispersion curves for 6061-O aluminum plate cooled to -5°C.

The dispersion curves for the S_2 mode in Fig. 3.7 show that it exhibits linear dispersion in the transition from the backward propagating region (S_{2B}) to the forward propagating region (S_2) proximate to $k = 0$. Fig. 3.7 (a) shows that the largest response is from the S_2 mode and that the A_1 mode and the S_0 mode are present, but that they have weaker measured responses to the excitation source. This is expected since the source is larger in size than the wavelength of all modes other than the S_2 mode. In fact, as was seen in Chapter 2, if the excitation source were Gaussian, only the S_2 mode would be excited. However, because the source is a top-hat, higher spatial frequency modes were excited due to the sharp edges of the source. The thickness of the cooled plate is 1.532 mm based on the room temperature measured thickness and application of the coefficient of linear thermal expansion: $24 \cdot 10^{-6}$ / Δ°C [10]. Poisson's ratio at -5°C was previously measured to be $\frac{1}{3}$. Using the thickness and v, the c_T for the plate was determined to be 3.138 mm/μs by using a best fit of the theoretical dispersion curve to the experimental data. The c_L is 6.276 mm/μs ($2 \cdot c_T$).

The behavior of conical dispersion at $k = 0$ was further explored by examining the measured frequency dispersion of only the S_2 mode near the coincident frequency. A zoomed in version of the data in Fig. 3.7 (a) is shown in Fig. 3.8 (a). The mode curve extracted from Fig. 3.8 (a) is shown in Fig. 3.8 (b), along with numerical simulation results. The numerical simulation was performed using the finite difference software PZFLEX. The simulation used the same geometry and material properties as the experiment and the data was processed in the same manner. The forcing function for the simulation was a 12.7 mm diameter circular top-hat applied normal to the surface and driven with a 5 cycle sine wave at 2.04 MHz.

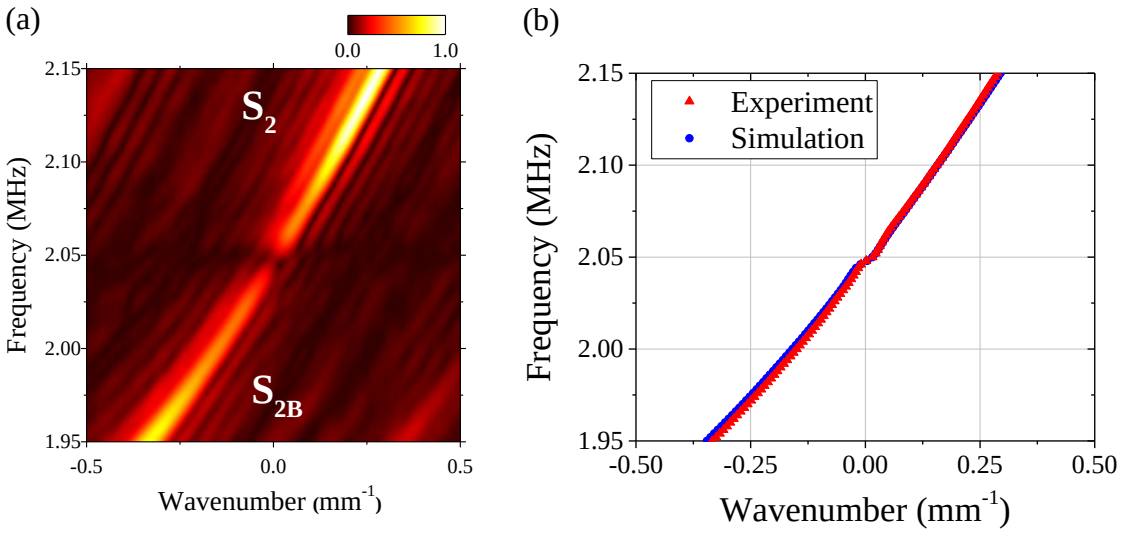

Fig. 3.8 (a) Magnitude plot of the 2D Fourier transform of the experimentally measured waveforms in the vicinity of $k = 0$. (b) Experimentally measured dispersion curve in the vicinity of $k = 0$ and simulation results.

The magnitude plot in Fig. 3.8 (a) shows that the response of the Lamb waves in the immediate vicinity of $k = 0$ is diminished. This result is in agreement with the theoretical predictions shown in Chapter 2. One cause for this effect is the finite size of the source. Specifically, a Lamb wave in which $k \rightarrow 0$ has a wavelength $\rightarrow \infty$ and therefore a finite sized source should couple less efficiently. This effect was confirmed using the theoretical solution, where a larger response at $k = 0$ was observed as the source size was increased (making the plate thinner gives the same effect for a fixed source size). The dispersion curves in Fig. 3.8 (b) exhibit a slight deviation from linearity proximate to $k = 0$. The slope the dispersion curve is approximated through this deviation and found to be ≈ 2.00 mm/μs, which agrees with the theoretical value: $c_g = 2c_T/\pi = 2.00$ mm/μs. The distortion was observed in both the experimental and numerical results. A possible cause of this distortion is operating in the near field of the source. This hypothesis was studied by observing time responses in multiple spatial windows, each with an increasing

distance from the source. This study was performed numerically and the results are shown in Fig. 3.9. The dispersion curves shown in Fig. 3.9 demonstrate that as the detection window is moved progressively further from the source location, the deviation from linearity near $k = 0$ decreases. This result confirms that the deviation from linearity is in fact due to detecting the wave motion in the near field of the source.

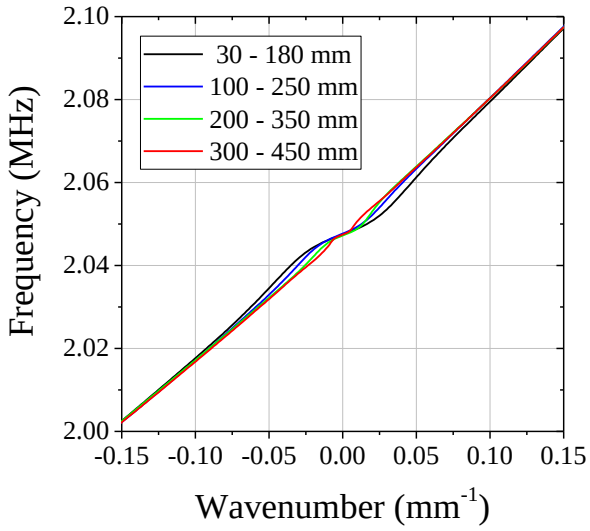

Fig. 3.9 Simulation results for dispersion in the vicinity of $k = 0$ moving the detection region further from the source. The deviation from linearity is seen to decrease with increasing distance from the source.

3.3 Measurement of Lamb Waves with near Conical Dispersion

The behavior of Lamb waves in a plate, with near conical dispersion, was demonstrated by testing the 6061-O aluminum plate at room temperature. The sample had a room temperature $\nu = 0.3349$, which is very close to the degenerate case of $\nu = \frac{1}{3}$. As such, Lamb waves with near

conical dispersion were measured on the sample in the manner described above except the plate was at room temperature instead of cooled to -5°C. The data was collected and processed in the same manner as in the cooled case and again compared with the results of an equivalent numerical simulation. The experimental and numerical results are shown in Fig. 3.10 in terms of extracted dispersion curves near $k = 0$.

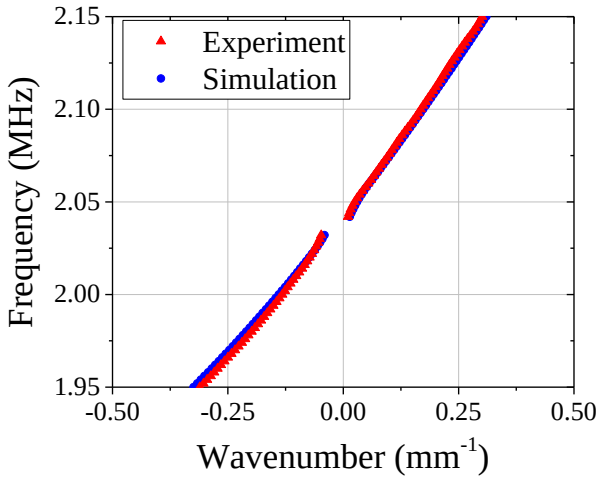

Fig. 3.10 Experimentally measured dispersion curve in the vicinity of $k = 0$ for the 6061-O aluminum plate at room temperature. Simulation results of the experiment are also shown.

The dispersion curves shown in Fig. 3.10 illustrate that the responses of the S_2 and S_{2B} mode curves cannot be resolved at very small k values, resulting in a gap in frequency and k. The gap in k occurs as a consequence of the parabolic dispersion at $k = 0$ for each mode. Parabolic dispersion results in very small group velocities for small k and thus these waves are not detected over the measurement time. The gap in frequency occurs because, for this case, the simple thickness resonances are not coincident. When this is the case, the S_{2B} mode and S_2 mode are connected via an imaginary loop in k space, as was shown in Chapter 2. The lower branch (S_{2B})

is associated with a shear simple thickness mode resonance, which has no normal displacement at $k = 0$. As the dispersion curve approaches this resonance its displacement profile will tend to conform to this shape and therefore it becomes increasingly difficult to excite and detect. The top branch (S_2), on the other hand, is associated with a longitudinal thickness resonance at $k = 0$, which has only displacement normal to the plate surface. Again, as this mode curve approaches the resonance its displacement profile will tend to this shape and therefore the upper mode curve can be resolved closer to $k = 0$ than the lower mode curve can, when exciting and detecting normal to the surface.

The plate thickness was measured to be 1.533 mm and ν was measured to be 0.3349, at room temperature. Using these two values the c_T was determined to be 3.125 mm/μs by using a best fit of the theoretical dispersion curve to the experimental data and c_L is 6.272 mm/μs.

The room temperature experiment demonstrates that without tuning the elastic properties of the plate to the degenerate condition linear dispersion is not observed in the vicinity of $k = 0$. This experiment does show, however, that Lamb waves with an extremely long wavelength and a finite group velocity can be generated in this sample at room temperature. For example, at 2.051 MHz the wavelength is 220 mm and the group velocity is ~ 2.5 mm/μs. These Lamb waves, with long wavelength and large group velocity, can be used to study the behavior of conical point Lamb waves in certain situations. For example, this wavelength is suitable for studying what happens when a conical point Lamb wave mode converts upon reflection or refraction to other modes with very small wavelengths, as will be demonstrated in Chapter 4.

3.4 Conclusions and Significance of Findings

This Chapter experimentally confirms that conical dispersion at $k = 0$ will occur in an isotropic homogeneous plate when the material's $\nu = \frac{1}{3}$. This result has been theoretically predicted [2,13] however this is the first time that it has been experimentally demonstrated. This was accomplished by temperature tuning the elastic properties of a 6061-O aluminum plate in order to induce degeneracy between the 1st symmetric longitudinal simple thickness resonance and the 1st symmetric shear simple thickness resonance. Poisson's ratio was measured using a laser ultrasonic technique at room temperature and as a function of temperature. The frequency dispersion was measured while the sample was cooled and linear dispersion in the vicinity of $k = 0$ was confirmed. A piezoelectric contact transducer, which generated longitudinal vibrations, was able to effectively generate Lamb waves with conical dispersion at $k = 0$. The generation and detection of Lamb waves with extremely long wavelengths and finite group velocity were also measured in a 6061-O aluminum plate at room temperature.

These results show that given the correct material parameters a simple plate can support propagating waves with an infinite wavelength and infinite phase velocity. The result is propagating waves that oscillate in time but are spatially uniform over the plate surface. This means that simple plates can be used to explore the physics of conical dispersion at zero wavenumber. Further, this unusual phenomenon may have application uses in acoustic devices and nondestructive testing.

3.5 References

[1] D. M. Stobbe and T. W. Murray, “Conical dispersion of Lamb waves in elastic plates,” Phys. Rev. B 96, 144101 (2017).

[2] R. D. Mindlin, *An Introduction to the Mathematical Theory of Vibrations of Elastic Plates* (World Scientific, Singapore, 2016).

[3] D. Clorennec, C. Prada, and D. Royer, “Local and noncontact measurements of bulk acoustic wave velocities in thin isotropic plates and shells using zero group velocity Lamb modes,” J. Appl. Phys. 101, 034908 (2007).

[4] C. M. Grünsteidl, I. A. Veres, and T. W. Murray, “Experimental and numerical study of the excitability of zero group velocity Lamb waves by laser-ultrasound,” J. Acoust. Soc. Am. 138, 242 (2015).

[5] D. Clorennec, C. Prada, D. Royer, and T. W. Murray, “Laser impulse generation and interferometer detection of zero group velocity Lamb mode resonance,” Appl. Phys. Lett. 89, 024101 (2006).

[6] C. Prada, O. Balogun, and T. W. Murray, “Laser-based ultrasonic generation and detection of zero-group velocity Lamb waves in thin plates,” Appl. Phys. Lett. 87, 194109 (2005).

[7] D. Clorennec, C. Prada, and D. Royer, “Local and noncontact measurements of bulk acoustic wave velocities in thin isotropic plates and shells using zero group velocity Lamb modes,” Appl. Phys. Lett. 101, 034908 (2007).

[8] C. Prada, D. Clorennec, D. Royer, and RLW, “Local vibration of an elastic plate and zero-group velocity Lamb modes,” J. Acoust. Soc. Am. 124, 203 (2008).

[9] J. Laurent, D. Royer, and C. Prada, “Temporal behavior of laser induced elastic plate resonances,” Wave Motion 51 (2014).

[10] Tables of Physical andChemical Constants, 16th ed. (Longmans, Green Co., 1995), 2.1.4 Hygrometry. Kaye & Laby Online, Version 1.0 (2005).

[11] M. R. Lindeburg, *Mechanical Engineering Reference Manual* (Professional Publications Inc., 2006).

[12] A. Blouin and J. P. Monchalin, “Detection of ultrasonic motion of a scattering surface by two-wave mixing in photorefractive GaAs crystal,” Appl. Phys. Lett. 65, 932 (1994).

[13] A. A. Maznev, “Dirac cone dispersion of acoustic waves in plates without phononic crystals,” J. Acoust. Soc. Am. 135, 577 (2014).

Chapter 4

Reflection of Lamb waves with Conical Dispersion from a Free Edge

4.1 Introduction

In Chapter 3 it was demonstrated that conical dispersion at zero wavenumber (k) occurs in elastic plates when the material's Poisson's ratio (ν) is equal to $\frac{1}{3}$. Lamb waves excited at the degenerate frequency were observed to have an infinite wavelength (λ), an infinite phase velocity (c_p), and a finite group velocity (c_g). The physical behavior of such a wave field is that the surface of the plate oscillates in time but spatially is uniform. This Chapter will explore how such a wave behaves when it encounters the free boundary of a plate. This is accomplished by first analyzing a plane wave at the degenerate frequency reflecting normal to a free edge. This will provide insight into the expected mode conversion of a conical Lamb wave from a free edge. Then the angle of reflection of the predicted mode converted waves will be analyzed using Snell's law and

consideration will be given to the behavior of a long, but not infinitely long, wavelength incident wave. Finally, an experiment is conducted where broad angle reflection is considered from a free boundary. Here the boundary is selected to focus the reflected field. The incident near conical Lamb wave and reflected fields are analyzed. The experimental results are also compared with a numerical simulation, where the material's elastic constants are set to the exact degenerate case.

4.2 Normal reflection of a plane wave from a free edge

A 1.5 mm thick plate with a shear wave velocity (c_T) and a longitudinal wave velocity (c_L) equal to 3.0 mm/μs and 6.0 mm/μs, respectively, will have conical dispersion at $k = 0$ at a frequency of 2.0 MHz. This occurs because of the degeneracy between the 1st symmetric longitudinal simple thickness resonance and the 1st symmetric shear simple thickness resonance, both of which are on the S_2 mode (S_2 and S_{2B} curves, respectively). At this frequency, the S_1, A_1, S_0, and A_0 modes also exist in the plate and occur at wavelengths 3.34 mm, 2.80 mm, 1.56 mm, and 1.35 mm, respectively, as shown in Fig. 4.1.

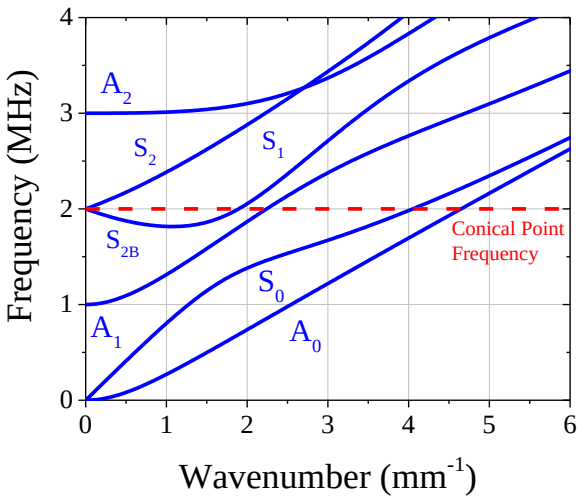

Fig. 4.1 Dispersion curves for a 1.5 mm thick plate with c_T = 3.0 mm/μs and c_L = 6.0 mm/μs.

A numerical simulation was performed of the above detailed plate using PZFLEX. The simulation was two dimensional and plane strain was assumed. The model geometry is shown in Fig. 4.2. The source function was a continuous 2 MHz sine wave applied normal to the surface with a Gaussian distribution, full width at half-max (FWHM) 12.5 mm.

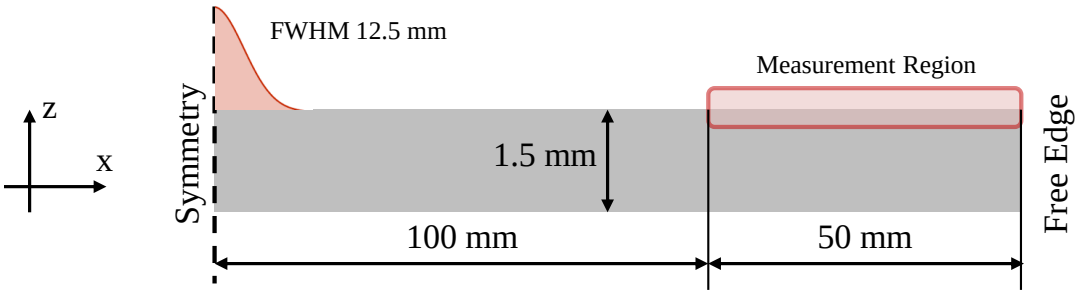

Fig. 4.2 Geometry for PZFLEX simulation of conical mode reflection from a free edge.

The normal displacement on the top of the plate was measured from 100 mm to 150 mm from the source in 50 μm steps. The data was processed in time with an FFT which was windowed

from 120 μs to 150 μs. The normal displacement at 2 MHz is shown in Fig. 4.3 (a). At the phase shown in Fig. 4.3 (a) multiple spatial modes are observed. First, a dc offset corresponding to the conical mode can be seen. Additionally, a short wavelength mode can clearly be seen. This mode is also modulated by another, longer wavelength, mode. In order to determine the spatial modes present, this data was processed in space with an FFT. The incident and reflected field contains the conical mode (S_2), the S_1 mode, and the S_0 mode as depicted in the spectrum shown in Fig. 4.3 (b). The presence of only symmetric modes is expected since the incident mode is symmetric and the boundary is symmetric. Which modes are reflected and the magnitude of these reflected modes is determined by satisfying the stress free boundary condition at the edge.

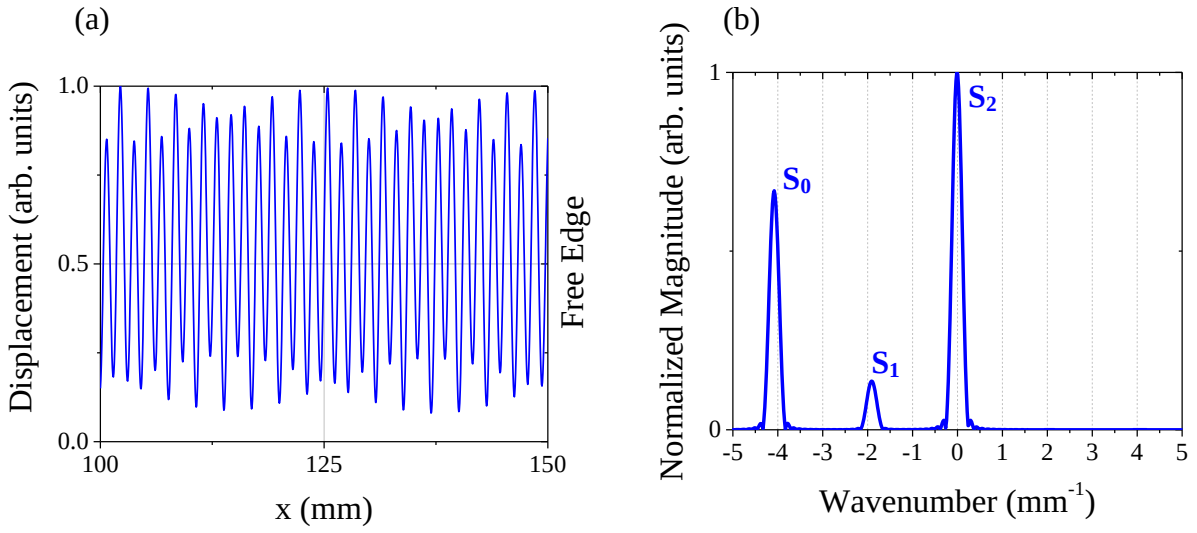

Fig. 4.3 (a) Normal displacement of plate at 2 MHz. (b) Spectrum of the incident and reflected wave field shown in (a).

Each incoming and outgoing mode contributes an in-plane and normal stress distribution along the edge of the plate and, for a free edge, the summation of these stresses must be zero. This problem is generally difficult to solve analytically because an infinite number of evanescent

modes must be considered in the reflected near field [1]. Accordingly, numerical techniques are often used except in the simplest of cases [2-7]. The relevant result of this experiment is that a conical point mode normally incident on a flat free edge mode converts and reflects an S_0 mode that can be strongly measured in the normal displacement. Additionally, we propose that a conical point mode has a loss of directionality, which means that these results should hold for any incident angle. The following Sections will explore the angle of reflection for mode converted waves from a conical point mode at broad angles. The results in the following Sections agree with the proposed loss of directionality.

4.3 Broad angle reflection of conical and near conical point Lamb waves from the free edge of a plate

In Section 4.2 it was demonstrated that when a conical point Lamb wave is incident on a free edge of the plate, mode conversion occurs upon reflection. This was shown for a plane wave at normal incidence. Here we consider broad angled reflection. The magnitude of the mode conversion is not considered here, but rather just the angle of reflection based on Snell's law:

$$\frac{k_I \sin(\theta_I)}{\omega_I} = \frac{k_R \sin(\theta_R)}{\omega_R}$$

$$\sin(\theta_R) = \frac{k_I}{k_R}\sin(\theta_I) \quad (when \quad \omega_I = \omega_R) \qquad (4.1).$$

$$\sin(\theta_R) = \frac{\lambda_R}{\lambda_I}\sin(\theta_I) \quad (when \quad \omega_I = \omega_R)$$

Where ω is frequency and the subscripts *I* and *R* are the incident wave and reflected wave, respectively. The angles in Eq. 4.1 are defined relative to the interface surface normal as illustrated in Fig. 4.4.

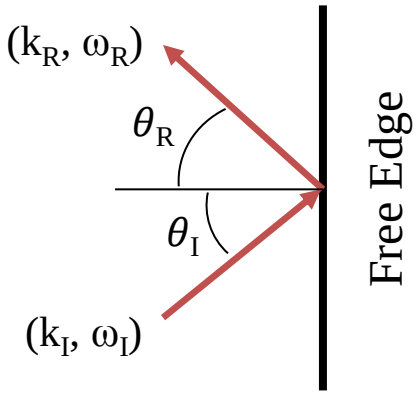

Fig. 4.4 Definition of incident angle (θ_I) and reflected angle (θ_R) for Lamb waves reflected from a free edge.

Consider the case were the incident wave is a conical point wave, $k_I = 0$ ($\lambda_I = \infty$). Examining Eq. 4.1, the reflected angle must be zero for all finite values of k_R and θ_I. This means that any mode converted wave that reflects from the boundary, when the incident wave is a conical point mode, must reflect normal to the interface. As such, the energy flow of the reflected field can be tailored and controlled by the geometry of the edge. A few examples of this concept are shown in Fig. 4.5.

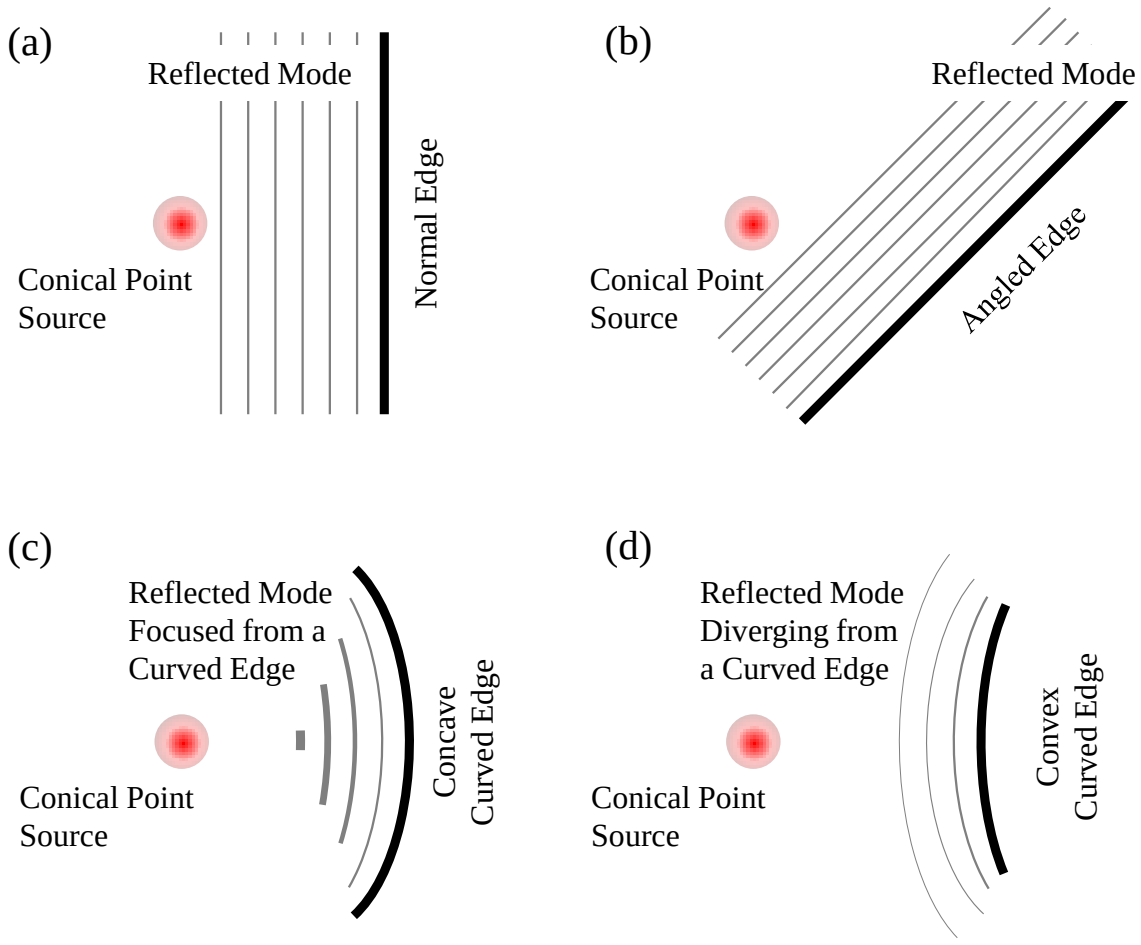

Fig. 4.5 Mode converted reflected field from an incident conical point mode for a normal edge (a), angled edge (b), concave curved edge (c), and convex curved edge (d).

Figs. 4.5 (a) and (b) shows that for the radially spreading source the mode converted reflected field is parallel to the edge and appears like it is emanating from a line source on the edge. In Fig. 4.5 (c) the field is reflected from a concave curved edge and the effect is that the field is lensed. On the other hand, when the field is reflected from a convex curved edge the reflected field spreads. One remarkable feature of the mode converted reflected fields in Fig. 4.5 are that they are independent of the source location. These examples show the conical point wave's loss of directionality.

Chapter 3 demonstrated that a 6061-O aluminum plate at room temperature had a ν very close to a degenerate case. It was also shown that very long wavelength Lamb waves could be effectively generated in this sample at room temperature, wavelengths ~ 220 mm. Here we consider how Lamb waves of this wavelength will approximate the conical point behavior illustrated in Fig. 4.5. This is accomplished by application of Snell's law and the wavenumbers of the plate modes at room temperature, as detailed in Table 4.1. Table 4.1 demonstrates that for any angle of incidence and for any reflected mode, the reflected angle will be $\theta_R < 1°$, relative to the interface normal. Further, the primary reflected mode is predicted to be the S_0 mode, and this mode will always be reflected < 0.4°. Consequently, near conical Lamb waves excited in the 6061-O aluminum plate at room temperature should demonstrate very similar behavior to the reflected wave fields shown Fig. 4.5

Table 4.2 Angles of reflection for a near conical point Lamb wave reflected from the free edge of a 6061-O aluminum plate.

Incident Angle	Reflected angle from an S_2 mode, λ = 220 mm			
	S_1, λ = 3.35 mm	*A_1, λ = 2.82 mm*	*S_0, λ = 1.57*	*A_0, λ = 1.38 mm*
0°	0°	0°	0°	0°
±15°	±0.23°	±0.19°	±0.11°	±0.09°
±30°	±0.44°	±0.37°	±0.20°	±0.18°
±45°	±0.62°	±0.52°	±0.29°	±0.25°

±60°	±0.76°	±0.64°	±0.35°	±0.31°
±75°	±0.84°	±0.71°	±0.40°	±0.35°
±90°	±0.87°	±0.74°	±0.41°	±0.36°

4.4 Experimental demonstration of conical point Lamb wave broad angle reflection from a curved free edge, resulting in mode converted field focusing

A conical point Lamb wave behaves as if it were temporally and spatially decoupled, meaning that the plate's surface displacement is oscillatory in time but stationary in space [8]. One result of this is that mode converted waves always reflect normal to the interface. In Fig. 4.5 it was demonstrated that a concave curved free edge would focus the field of mode converted waves. Here, a semi-circular edge is machined into a plate, near conical point Lamb waves are generated in the plate, and the reflected field is measured. The experimental setup is depicted in Fig. 4.6; the geometry of the semi-circle edge and the transducer location are also specified.

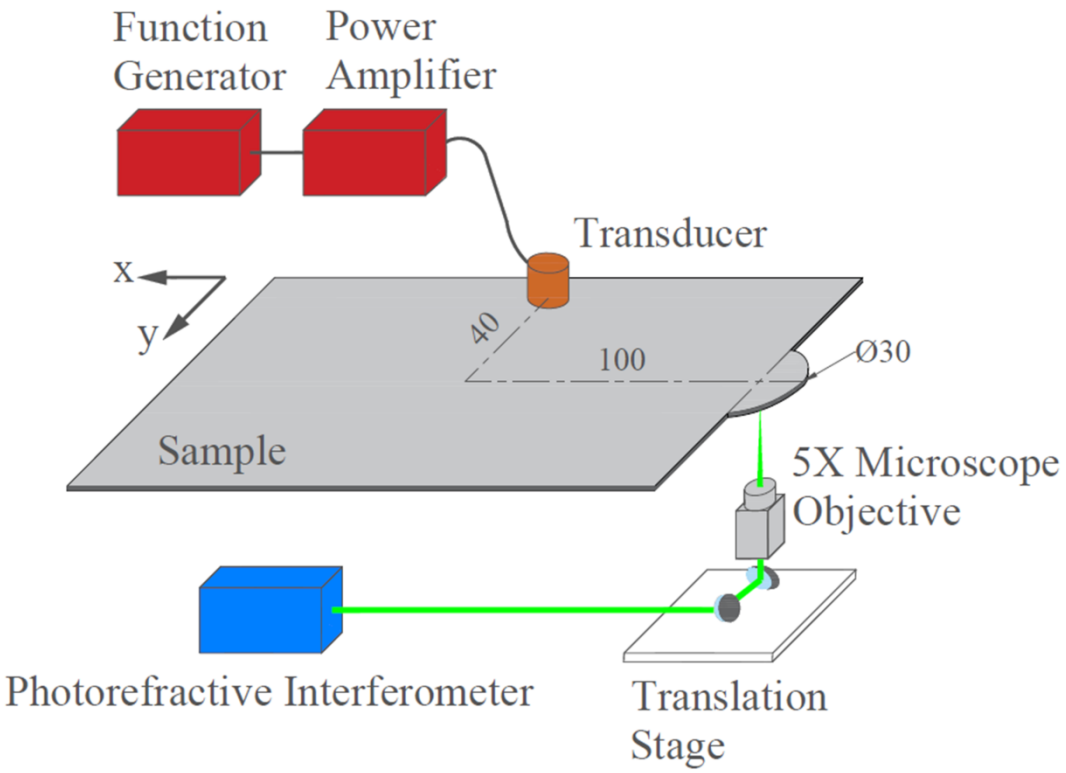

Fig. 4.6 Experimental setup for measured broad angled reflection of conical point Lamb waves from a semi-circle free edge of a 6061-O aluminum plate.

The transducer was located at a random position with respect to the semi-circle edge in order to demonstrate the invariance of the source location to the focusing effect. The transducer was driven with a 50-cycle tone burst at a frequency of 2.051 MHz, where the wavelength was 220 mm and the associated phase velocity was 4.5×10^5 m/s. The detection laser was scanned over a 35×35 mm^2 region of the plate, encompassing the semicircular feature, with a step size of 0.2 mm along each axis, and the normal surface displacement was measured at each spatial position. The time domains were recorded for 200 μs at a sampling rate of 50 MHz. Five-hundred (500) waveforms were averaged for each location. The data was processed using an FFT over a 60 to 100 μs time window. The magnitude and phase angle of the surface displacement at a frequency

of 2.051 MHz was then determined at each spatial position. The displacement amplitude at an arbitrary phase is shown in Fig. 4.7 (a).

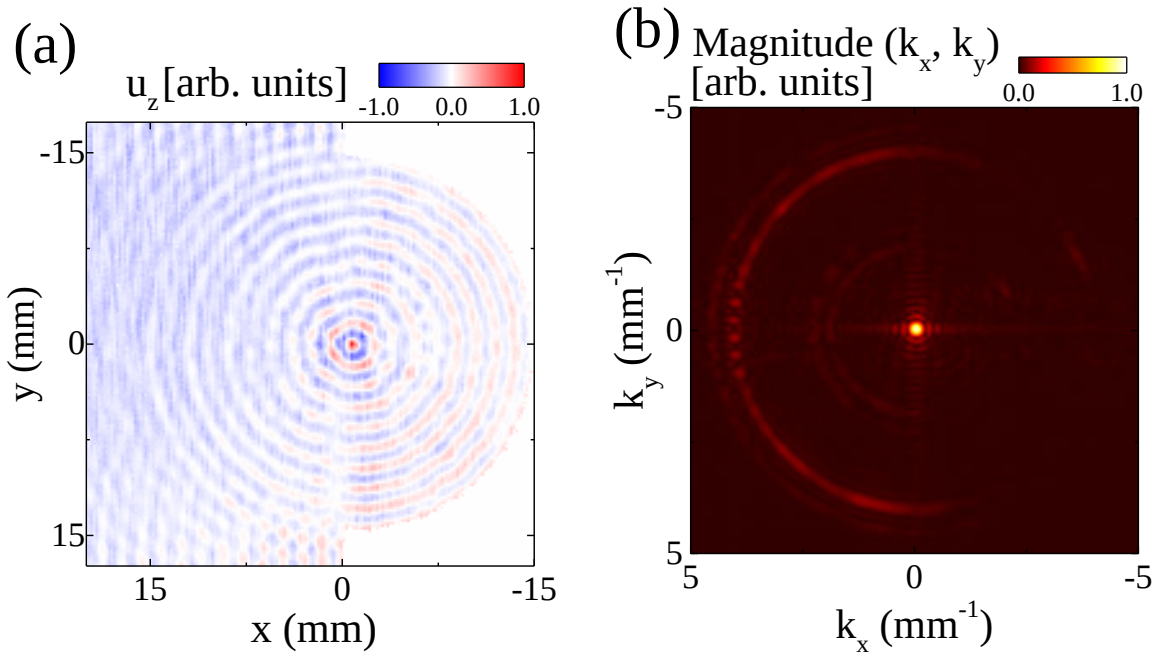

Fig. 4.7 (a) Normal displacement at a frequency of f = 2.051MHz from the experimental measurements. (b) Fourier domain representation of the measured wave field. The dominant modes are the incident S_2 mode near $k = 0$ and mode converted S_0 mode.

The near-degenerate S_2 mode has a wavelength much longer than the image size, therefore only contributing a dc offset to the image and little to no spatial structure. The primary spatial structure in Fig. 4.7 (a) is from the reflected S_0 mode ($\lambda = 1.57$ mm). The wave field of this reflected mode is seen to focus at the geometric center of the semi-circle edge. The displacement data in Fig. 4.7 (a) was processed with 2D FFT in the *x* and *y* spatial directions, the magnitude of which is shown in Fig. 4.7 (b). The magnitude image in Fourier space shown in Fig. 4.7 (b) gives the spectral content of the incident and reflected field. The field primarily consists of the incident

S_2 mode, which appears as a "hot spot" near (k_x, k_y) = (0, 0), and the reflected S_0 mode, which appears as a semicircle ring with a radius of $k \sim 4.00$ mm^{-1}. The magnitude of the S_0 ring is quite uniform over the full 180° of the semi-circular edge. This supports the claim that the incident near conical mode has an almost total loss of directionality. The mode conversion from the flat edge above and below the semi-circular region can also be observed in Fig. 4.7 (a) and is seen to be normal to edge, similar to the behavior predicted in Fig. 4.5 (a), and results in the light-dark pattern near $k_y = 0$ in Fig. 4.7 (b).

The reflected S_0 mode can be observed more clearly by spatially filtering the data in Fig. 4.7 (a) with a bandpass filter (k = 3.0 – 5.0 mm^{-1}), as shown in Fig. 4.8. (a).

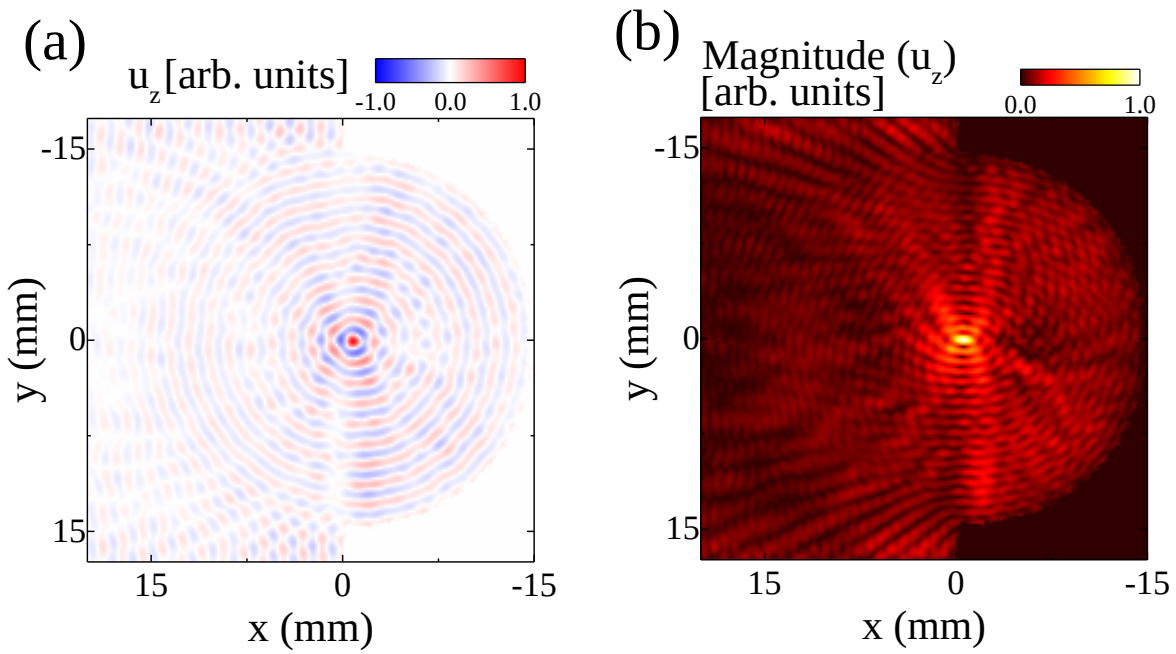

Fig. 4.8. (a) The displacement field in Fig. 4.7 (a) after a bandpass filter (k = 3.0 to 5.0 mm^{-1}) in order to isolate the S_0 mode arising from mode conversion from the plate edge. (b) Magnitude of the normal displacement field at 2.051 MHz showing focusing of the S_0 wave field at the center of the lens.

After spatial filtering, the reflected S_0 mode is clearly seen to nearly uniformly mode convert from the free edge and reflects at an angle normal to the edge, as evident by the focusing. This is similar to the predicted result sin Fig. 4.5 (c). As was previously noted, a remarkable feature of this type of system is that the focusing is independent of the source location. A magnitude plot of the filtered field is shown in Fig. 4.8 (b). Here it is observed that the field magnitude is highest at the geometric center of the semi-circular edge, again confirming that the edge acts as a lens for mode converted reflections from the near conical point incident field.

The lensing experiment was conducted with a 6061-O aluminum plate at room temperature, where the material's Poisson's ratio was 0.3349 which was close to the degenerate case of $\nu = \frac{1}{3}$. In Section 4.3 it is was shown that with this Poisson's ratio the angle of mode conversion reflection is very close to normal to the interface for any incident angle. In order to investigate any potential differences in the wave field behavior that could occur at a true degeneracy, a simulation was performed using PZFLEX identical to the experiment with the exception of Poisson's ratio, which was set to $\frac{1}{3}$. The excitation source was a circular normal force with a diameter matching that of the transducer, and the mechanical properties were selected to match the cooled specimen discussed earlier in Chapter 3. The temporal excitation profile and data processing approach where identical to the experiment. In this case, the degeneracy occurs at a frequency of 2.048 MHz. Fig. 4.9 (a) and Fig. 4.9 (b) give the calculated displacement field and that field in Fourier space, respectively. Fig. 4.9 (c) and Fig. 4.9 (d) show the calculated bandpass filtered displacement and displacement magnitude plot, respectively. A qualitative comparison between all experimental and simulation plots shows good agreement between the two. Specifically, both show angle independent mode conversion and normal reflection for the S_0 mode at the free edge.

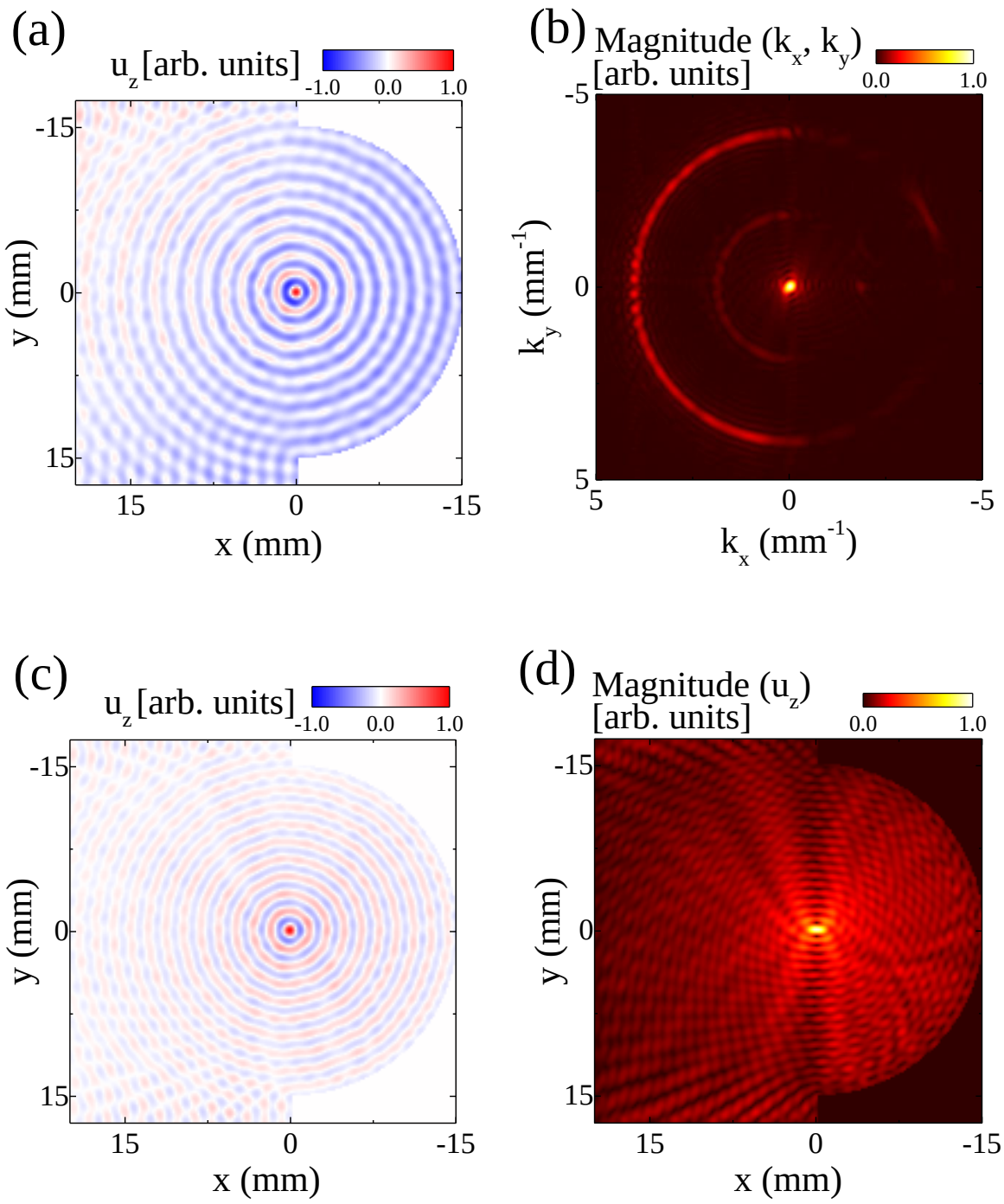

Fig. 4.9 (a) Normal displacement at a frequency of f = 2.048 MHz found from the numerical simulation. (b) Fourier domain representation of the measured wave field. The dominant modes are the incident S_2 mode near $k = 0$ and mode converted S_0 mode. (c) The displacement field in (a) after a bandpass filter (k = 3.0 to 5.0 mm^{-1}) in order to isolate the S_0 mode arising from mode conversion at the plate edge. (d) Magnitude of the normal displacement field at 2.048 MHz showing focusing of the S_0 wave field at the center of the lens.

Returning to the experimental data, the incident S_2 near conical point mode is examined. This was accomplished by first examining the time domain responses at four random locations in the lens as indicated in Fig. 4.10.

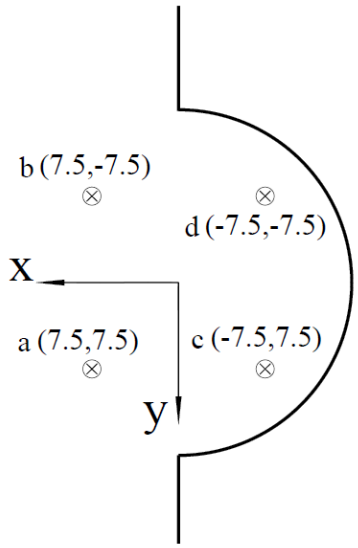

Fig. 4.10 Location of four random positions on the plate where the temporal responses of the S_2 mode are examined.

The data was low-pass filtered at a spatial frequency of 1.0 mm^{-1} in order to isolate the S_2 mode and the resulting wave forms are shown in Fig. 4.11 (a). The time traces show an initial transient tone burst, due to the 50 cycle tone burst, followed by a prolonged ringing. This is similar behavior to the theoretical response to an impulse that was shown in Chapter 2. Fig. 4.11 (b) depicts the time traces in Fig. 4.11 (a) zoomed-in between 90 and 95 μs. The surface displacement at all four of these points oscillates with a nearly identical phase; this is expected due to the unusually large wavelength of the S_2 mode. These results confirm the generation of the near conical point S_2 mode and show the spatial invariance of this field. The wavelength of

this incident mode can be estimated by inspecting the phase delay of the displacement response at 2.051 MHz, as shown in Fig. 4.12.

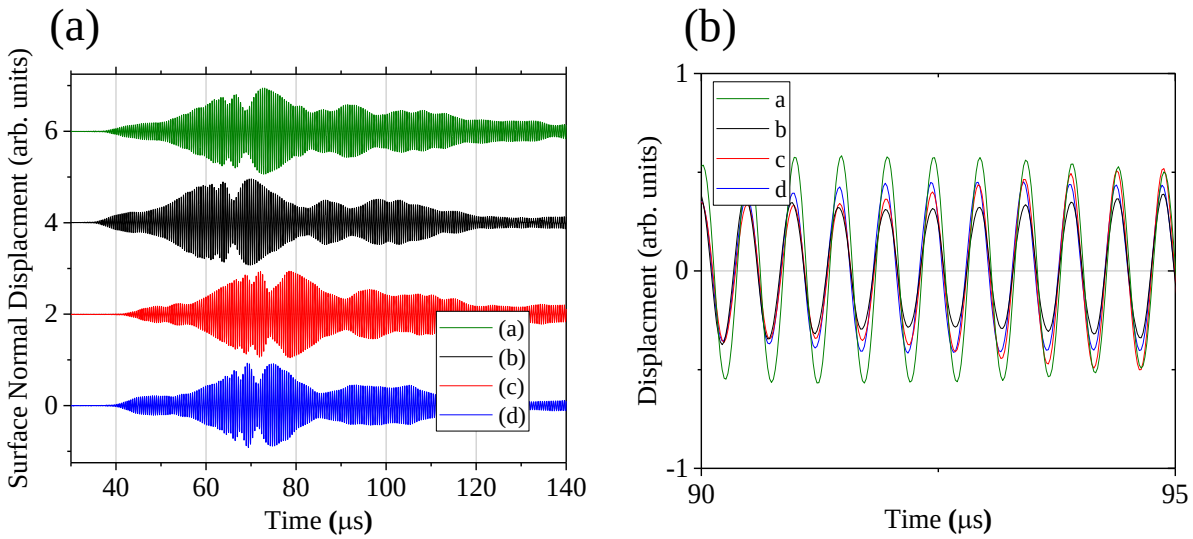

Fig. 4.11 (a) Time domain responses after a low-pass spatial filter (k = 1.0 mm^{-1}), in order to isolate the S_2 mode, at the four locations shown in Fig. 4.10. (b) Zoomed-in view of the time domain responses in (a) showing the uniform phase of the oscillations at the different spatial positions.

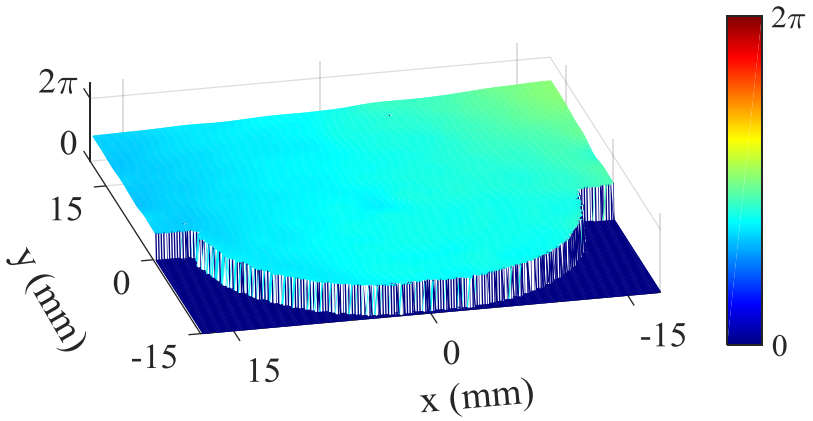

Fig. 4.12 Phase of the oscillation of the S_2 mode over the surface of the lens at 2.051 MHz. A low-pass spatial filter (k = 1.0 mm^{-1}) was used to isolate the S_2 mode.

The data was spatially low-pass filtered ($k = 1.0\ mm^{-1}$) and the phase angle found by using a temporal FFT of the wave forms in the 60–100 μs time window. The wavelength of the S_2 mode was estimated to be 190 mm, with an associated phase velocity of 3.9×10^5 m/s. Within the context of the ~ 30x30 mm^2 window in Fig. 4.12, the phase of the incident S_2 mode is nearly uniform at this frequency. The estimated wavelength of the S2 mode within the lens is slightly different that that predicted by the dispersion curve in Chapter 3. The dispersion curve in Chapter 3 was measured in the middle of the sample not along the edge where this experiment was performed. This discrepancy is likely due to thickness variation in the plate.

4.5. Conclusions and Significance of Findings

In this Chapter angle independent mode conversion of a Lamb wave with conical dispersion from the free edge of a plate was experimentally demonstrated. This behavior was similar to that previously demonstrated by refracting waves to and from a zero-index meta-material [9-10] and zero-index wave guides [11] at curved interfaces. Here, however, the existence of multiple spatial modes of propagation at the degenerate frequency allowed the creation of a lens by reflecting a Lamb wave from a semi-circular edge. Theory predicted that a conical point S_2 mode would mode convert primarily to an S_0 mode upon encounter a free edge and that the angle of reflection would be normal to the interface for all incident angles. This behavior was experimentally confirmed by focusing the reflected S_0 field from the semi-circular edge. The experiment showed that the mode conversion was uniform for the full 180° of the edge which confirmed that the conical point Lamb wave was spatially uniform. Examining time responses, the incident near conical point wave was observed to be oscillatory in time but have equal phase

throughout the region of observed space. This behavior confirms the hypothesis that a conical point wave is essentially decoupled in space and time.

Numerical simulation demonstrated that for the experimental geometry there was little difference between the behavior of the near conical case and the true degenerate case. The critical parameters to achieve focusing from a semi-circular edge are that the incident mode's wavelength be much longer than the reflected mode's wavelength and that the phase of the incident mode be nearly uniform over the entire geometry of the lens. These two conditions were satisfied in the experiment, where the incident mode's wavelength was two orders of magnitude larger than the reflected mode's wavelength and was 6-7 times larger than the entire lens.

The findings of this Chapter show that a simple plate, with elastic parameters such that conical dispersion (or near conical dispersion) exists at $k = 0$, can be used to control the flow of elastic energy in novel ways. Specifically it was shown that energy can be focused from the edge of a plate. It should also be possible to manipulate fields in other interesting ways including columnating a field from an interface and steering waves around 180° bends, to name a few.

4.6. References

[1] J. D. Achenbach, *Wave Propagation in Elastic Solids* (North-Holland, Amsterdam, 1973).

[2] I. Bartolia, A. Marzania, F. Lanza di Scaleaa, and E. Violab, “Modeling wave propagation in damped waveguides of arbitrary cross-section,” J. Sound Vib. 295, (2006).

[3] M. V. Predoi, M. Castaings, B. Hosten, and C. Bacon, “Wave propagation along transversely periodic structures,” J. Acoust. Soc. Am. 121, 4 (2007).

[4] M. Castaings and M. Lowe, “Finite element model for waves guided along solid systems of arbitrary section coupled to infinite solid media,” J. Acoust. Soc. Am. 123, 2 (2008).

[5] P. J. Torvik, “Reflection of Wave Trains in Semi-Infinite Plates,” J. Acoust. Soc. Am. 41, 346 (1967).

[6] R.D. Gregory and I. Gladwell, "The reflection of a symmetric Rayleigh-Lamb wave at the fixed or free edge of a plate," J. Elasticity 13(2), 185 (1983).

[7] B. Morvan, N. Wilkie-Chancellier, H. Duflo, A. Tinel, and J. Duclos, “Lamb wave reflection at the free edge of a plate,” J. Acoust. Soc. Am, 113(3), 1417 (2003).

[8] D. M. Stobbe and T. W. Murray, “Conical dispersion of Lamb waves in elastic plates,” Phys. Rev. B 96, 144101 (2017).

[9] X. Huang, Y. Lai, Z. H. Hang, H. Zheng, and C. T. Chan, “Dirac cones induced by accidental degeneracy in photonic crystals and zero-refractive-index materials,” Nat. Mater. 10, 582 (2011).

[10] F. Liu, X. Huang, and C. T. Chen, “Dirac cones at k = 0 in acoustic crystals and zero index acoustic materials,” Appl. Phys. Lett. 100, 071911 (2012).

[11] C. Zhang, C. T. Chan, and X. Hu, “Broadband focusing and collimation of water waves by zero refractive index,” Sci. Rep. 4, 6979 (2014).

Chapter 5

Scattering of Lamb waves with Conical Dispersion

5.1 Introduction

Elastic wave scattering from discontinuities in solids is a subject of great interest [1]. The main driver for this attention is the need for quantitative ultrasonic flaw characterization, with the goal to characterize the size, orientation, and shape of a discontinuity based on information obtained from scattered ultrasonic waves [2]. The exact solution for wave scattering problems has only been solved for a few idealized systems. In these cases, the flaw is generally a smooth closed surfaces such as a spheroid or planar surface with sharp edges [3]. The applicable theory for analyzing a scattering problem is often based on the product of the incident wave's wavenumber (k) and the general dimension of the discontinuity (a). For example, for spherical inclusions and $ka < 1$, the integral boundary Born approximation is valid and becomes more accurate as $ka \rightarrow 0$

[4]. Alternatively, when $ka > 1$ a geometric diffraction theory is generally used [5, 6]. Note that when the $ka > 1$ the problem is sometimes referred to as wave diffraction instead of wave scattering. For more complicated discontinuities a numerical approach is often used such as boundary element modeling or finite element modeling [1].

The more specific topic of elastic wave scattering in plates (Lamb waves) is also of great interest due to the prominent use of Lamb waves in non-destructive testing. Interpreting scattered Lamb wave fields is challenging due to the presence of multiple propagating modes and infinitely many complex modes. Even in the low frequency regime there are at minimum two propagating modes, a symmetric and an antisymmetric, and a third shear horizontal wave that can occur when these modes interact with a scatterer [7]. When the frequency is low and the scatterer has a simple geometry, analytical techniques can be used [8-13]. Lamb wave scattering for high frequencies, where many propagating and non-propagating modes must be considered, is generally studied with the aid of numerical modeling. For example, the finite element method (FEM) has been used [14,15], combinations of FEM and analytical solutions have been used [16,17], and a normal mode expansion and a boundary element method has been used [18]. Here, we examine how a Lamb wave with conical dispersion at $k = 0$ scatters from a finite sized hole in a plate. This topic is unexplored in the literature, owing to the fact that Lamb waves with conical dispersion are relative unexplored and had never been experimentally demonstrated. The approach will be to first use a simplified low frequency analytical model to examine wave scattering when $ka \rightarrow 0$, then a 3D finite element model and experiments are conducted to examine a Lamb wave scattering from a hole when $k = 0$, and finally 3D finite element models and experiment is used to show how a propagating Lamb wave at $k = 0$ can be used to hide scatterers in the long wavelength field.

5.2 Compression waves in a thin plate scattering from a hole

An analytical solution to the problem of a compressional wave incident on a hole in a thin plate is considered here. The aim of this analysis is to glean insight into how a Lamb wave with an infinite wavelength might interact with a finite sized hole. This is accomplished by examining how a single mode compressional wave scatters from a hole as its wavelength becomes large, with respect to a hole.

This simplified model considers a compressional wave in an infinitely extended elastic plate impinging on a finite sized hole in the plate [13]. A zero-order approximation of the three-dimensional equations of elasticity is used, where the displacement components are independent of the plate thicknesses. This requires that the frequency is low enough that only the S_0 mode and A_0 mode are present, or, at a frequency lower than all of the simple thickness mode resonances. Additionally, the low frequency complex wavenumber modes are ignored, which is valid as long as the wavelength is long with respect to the plate thicknesses [13]. Fig. 5.1 depicts the simplified scattering problem.

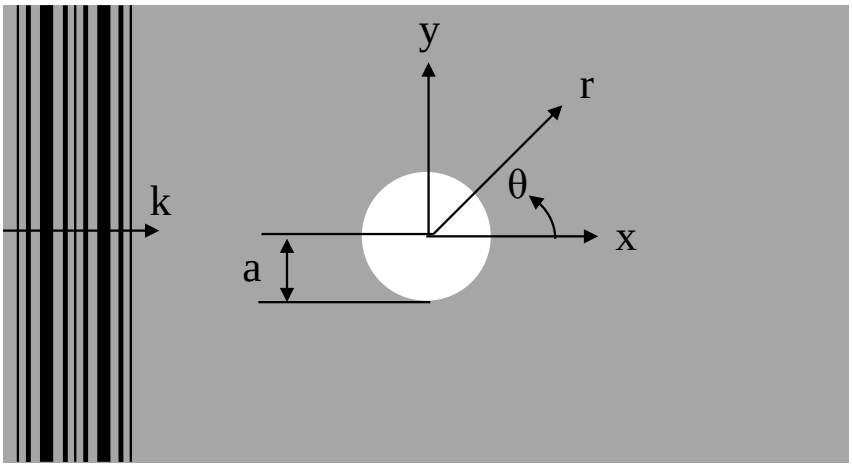

Fig. 5.1. Geometry of compression wave in a thin plate incident on a hole of radius *a*.

The general procedure for solving this problem is as follows:

1. Write out the incident field and scattered field potential functions in polar coordinates.
    a. Note that the incident field consists only of a dilatational potential and the scattered field contains a dilatational and equivoluminal potential (allowing for mode conversion to a shear wave)
    b. The incident and scattered potentials are represented by infinite series of Bessel and Hankel functions, respectively
2. The stress and displacement fields are written using the potentials.
3. The stress free boundary condition along the hole surface (σ_{rr} & $\sigma_{r\theta}$ = 0 @ r = a) are enforced, which then allows for the calculation of the unknown series coefficients.

This solution was implemented numerically using MATLAB® and is shown in Appendix C. An interesting feature of the normalized displacement and stress solutions are that the they depend only on the plate's Poisson's ratio (for an isotropic material) and the product of the incident

wave's wavenumber and the radius of the hole (*k*a) [12,13]. The displacement magnitude in the *x*-direction and the *y*-direction, around the surface of the hole, is shown in Fig. 5.2 for the case where the incident wave's wavelength is larger, but still similar in size, to the hole (*ka* = 1, or λ = 4πa) and Poisson's ratio was equal to ⅓.

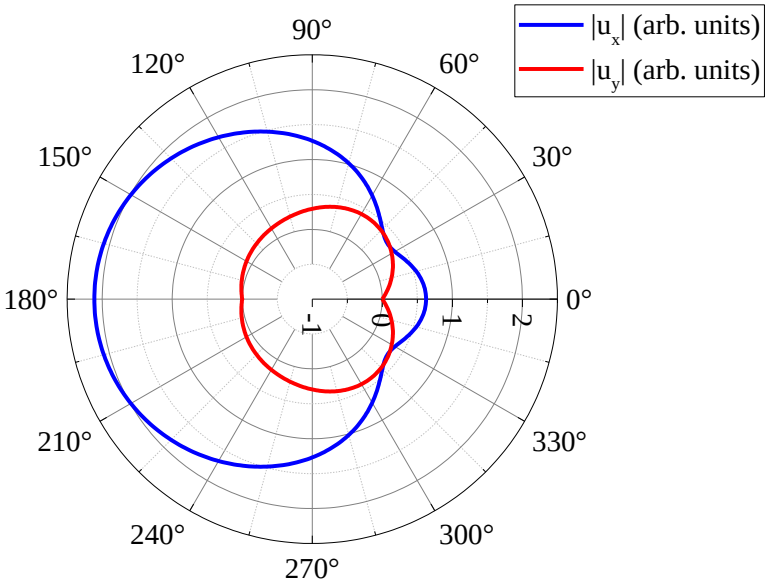

Fig. 5.2 Normalized displacement field magnitude at r = a from an incident compressional wave scattered from a hole in a thin plate, where *k*a = 1.

As a reference, the incident field, in absence of a hole, has a unit magnitude in the *x*-direction at every location and zero magnitude in the *y*-direction. In the case where *k*a = 1, the field has a "shadow" behind the hole, as evident by a magnitude less than unity from approximately 300° - 60° (behind the hole). Much of the incident mode is scattered back toward the source as seen by the increase in magnitude from unity in the *x*-direction around 180°. There is mode conversion to a shear wave (A_0) as evident by the non-zero displacement in the *y*-direction. The peak mode conversion occurs at around 60º and 300º. The behavior of an incident wave with a wavelength

much longer than the size of the hole was determined by setting $ka = 0.001$ and examining the displacement magnitude around the hole as shown in Fig. 5.3.

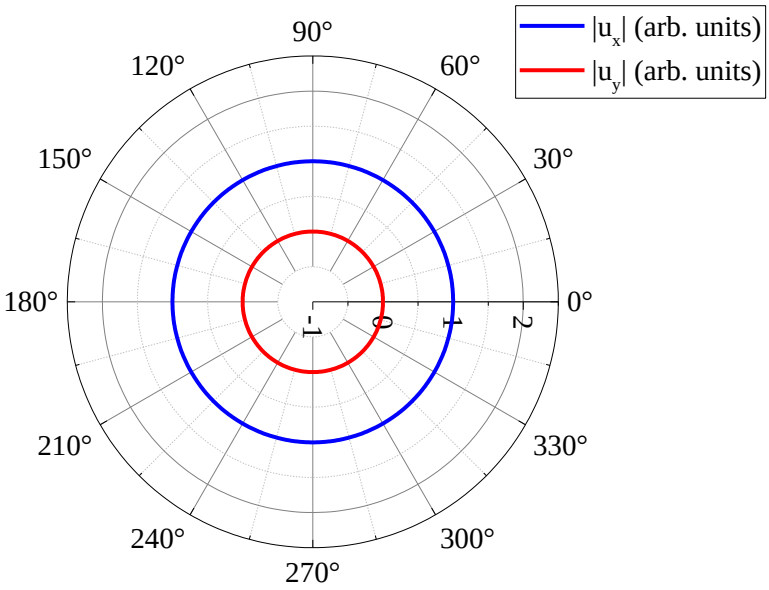

Fig. 5.3 Normalized displacement field magnitude at r = a from an incident compressional wave scattered from a hole in a thin plate, where $ka = 0.001$.

Here, there is no mode conversion or scattering of the incident wave field. The displacement magnitude in the x-direction is uniformly equal to unity around the hole and the displacement magnitude in the *y*-direction is uniformly equal to zero around the hole. In the case where $ka \rightarrow 0$ the incident and scattered displacement field is simply equal to the incident field when there is no hole. This result should not be surprising since instead of making the incident wavelength long with respect to the hole's radius we could have equivalently made the hole's radius small with respect to the wavelength. From this perspective, the limiting case of $ka \rightarrow 0$ would mean that the hole's radius tended to zero or that the hole disappeared. These results are interesting in the

context of a conical point Lamb wave because they imply that an incident wave with zero wavenumber will not scatter from any finite sized hole. However, the analytical solution here assumes no field dependency through the plate thickness and is only valid at frequencies below any of the simple thickness mode resonances. In the next section a 3D finite element simulation is used to study the behavior of a conical point Lamb wave scattering from a finite sized hole.

5.3 Numerical simulation of Lamb waves with conical dispersion at $k = 0$ scattering from a hole

In this section a numerical simulation is performed in order to investigate the scattering of a Lamb wave with conical dispersion at $k = 0$ from a finite sized hole in a plate. The simulation is performed using the finite difference software PZFLEX. A 1.5 mm thick (H) plate with longitudinal wave velocity (c_L) = 6.0 mm/μs and shear wave velocity (c_T) = 3.0 mm/μs is considered ($\nu = ⅓$). The plate was modeled on an orthogonal grid with element dimensions 50x50x25 μm^3 (x,y,z). A 6 mm diameter hole was located at the origin of the coordinate system and a continuous sinusoidal line force was applied normal to the top of the plate at x = -35 mm. The excitation had a Gaussian distribution in the x-direction, centered at x = -35, with a full width at half max (FWHM) of 12 mm. The simulation geometry is shown in Fig. 5.4. The normal displacement on the surface of the plate was measured. The source was smooth and spatially large enough to suppress the excitation of all higher wavenumber modes and only excite the S_2 mode at $k = 0$. The excitation frequency was 2.0 MHz (c_T/H) which is the coincident frequency of the first symmetric shear and first symmetric longitudinal simple thickness

resonances and has been shown to generate Lamb wave's with a finite group velocity and an infinite phase velocity (conical point Lamb waves).

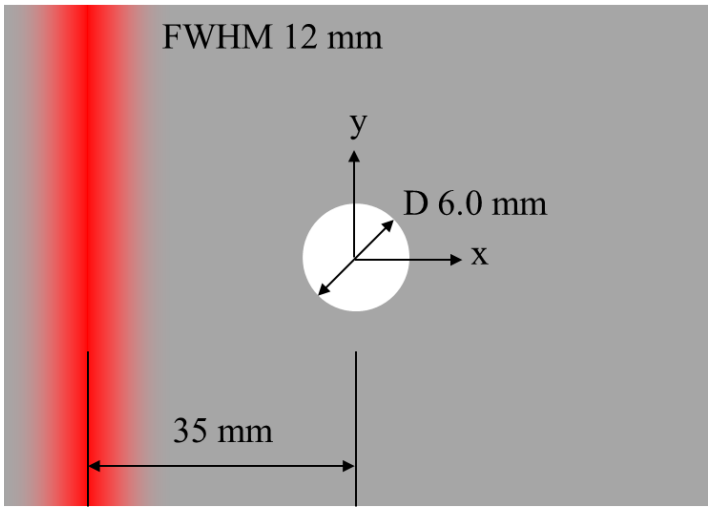

Fig. 5.4 Simulation geometry for Lamb wave with conical dispersion at $k = 0$ scattering from a finite sized hole in a plate.

The time domain waveforms were windowed between 10 - 14 μs, 16 - 20 μs, 23 - 27 μs, and 36 - 40 μs and in each case processed using a Fourier transform. The magnitude of the surface displacement at a frequency of 2.0 MHz was determined for each time window and at each spatial position, and the displacement amplitude is plotted in Fig. 5.5 (a) – (d). A low pass spatial filter ($k = 0.5$ mm^{-1}) was applied in order to suppress the higher spatial modes that arise as a result of mode conversion from the hole. Remarkably, the incident conical point Lamb wave appears to "flow" around the hole without any distortion. This is similar to the behavior observed in the simplified model shown in Section 5.2. However, in the simplified model when $ka \rightarrow 0$ there was no mode conversion from the hole.

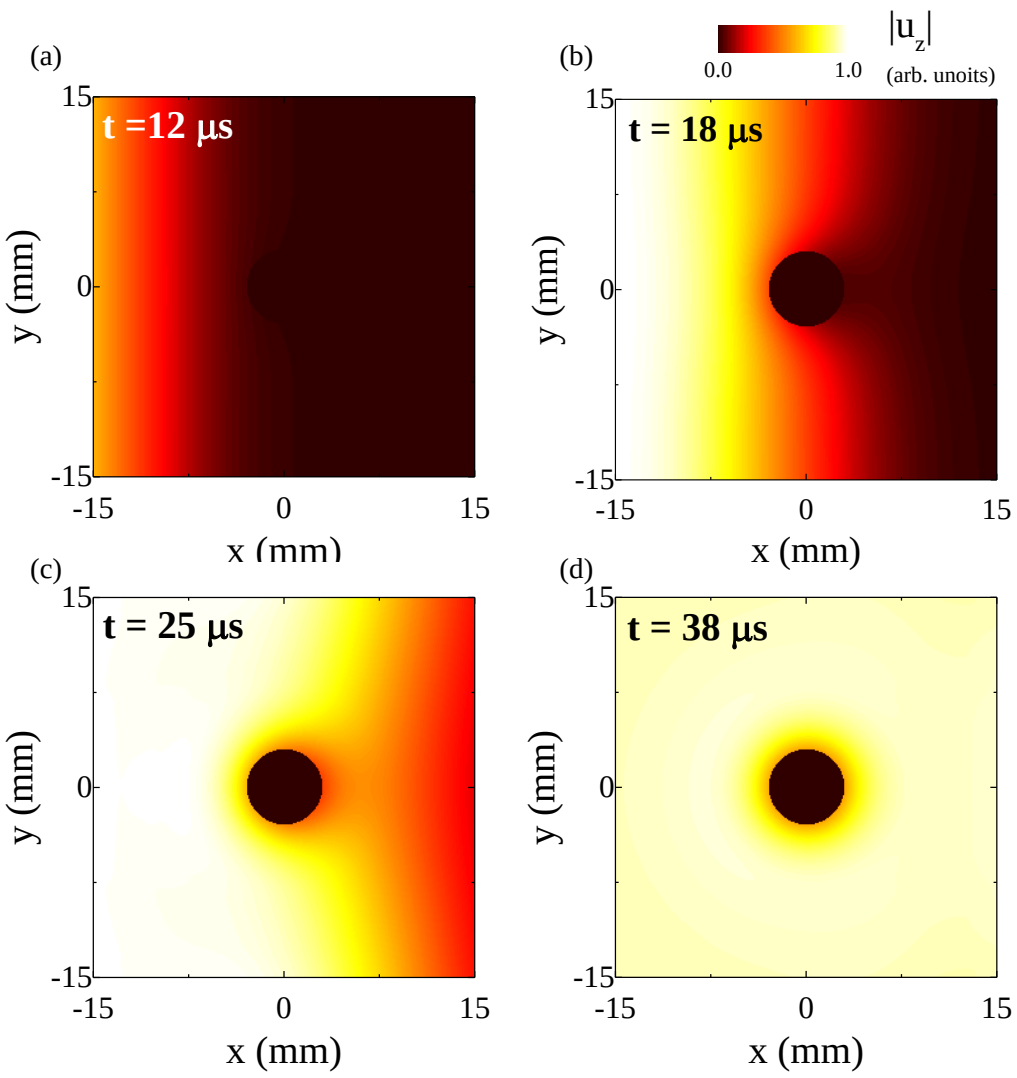

Fig. 5.5 Magnitude of normal displacement at a frequency of 2.0 MHz at various instants in time. The displacement is low pass filtered (k = 0.5 mm^{-1}). The hole in the plate has a 6 mm diameter and the plate has: c_T = 3.0 mm/μs, $c_L = 2c_T$, and H = 1.5 mm.

Here, the incident wave is observed to mode convert at the hole. This is expected since "A two-dimensional solution, however, contains shearing stresses in addition to the longitudinal stresses. As the component of longitudinal stress reflects from a free edge with a change in sign and the component of shear stress without, it is impossible for the superposition of a right-traveling wave

and a left-traveling wave of the same and single wavelength to produce the desired condition of zero traction on the end face" [19]. The mode converted field consists mainly of the S_0 mode and a smaller amount of the S_1 mode (these results agree with the findings in Chapter 4). The steady state mode converted field is shown in Fig. 5.6 (a), where a high pass filter (k = 3.0 mm^{-1}) was used to isolate the S_0 mode. The field in Fig. 5.6 (a) is shown in Fourier space in Fig 5.6 (b). The most salient feature of the mode converted field is that it is uniform in magnitude and phase around the hole. This observation is also confirmed by inspection of the magnitude in Fourier space, which is a 360º ring of uniform amplitude with a radius ~ 4 mm^{-1}. This means that the incident conical point field must also be uniform in magnitude and phase around the hole, since it is the source of the mode converted field. The incident Lamb wave field causes the hole to act as a pseudo-source for the mode converted field. However, the incident field itself appears unperturbed by the hole. Similar simulations were also performed where finite wavelength Lamb waves were instead excited. In these cases the presence of the hole caused perturbation to the incident field and the mode conversion was not perfectly uniform around the hole.

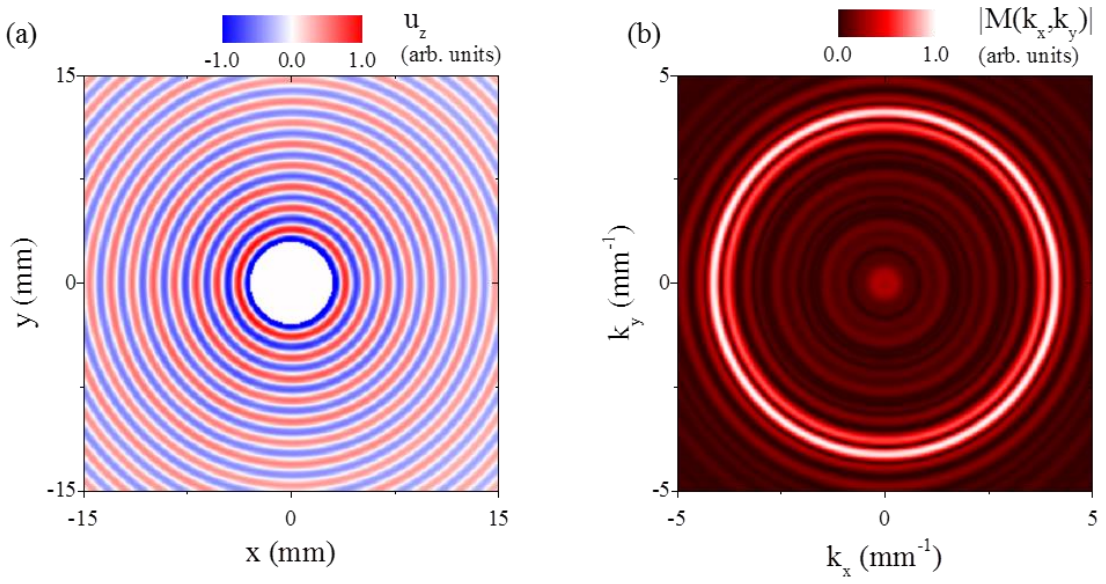

Fig. 5.6 Normal displacement at a frequency of 2.0 MHz at steady state (a). The field is high pass filtered (k = 3.0 mm^{-1}). (b) Fourier domain representation of field in (a).

5.3 Experimental results of Lamb waves with conical dispersion at k = 0 scattering from a hole

In this section the scattering of Lamb waves with conical dispersion at k = 0 from a hole in a plate is experimentally measured. To begin, the dispersion curve for a 305 x 305 mm^2 6061-O aluminum plate, with a measured thickness of 1.539 ± 0.003, was measured while the plate was cooled to approximately -5 ºC. The temperature was selected based on the Poisson's ratio measurements of the 6061-O aluminum plate in Chapter 3. At this temperature, the plate should exhibit conical dispersion at k = 0 because its Poisson's ratio will, on average, be = ⅓. Measuring the dispersion curve will confirm this and will give the frequency at which the degeneracy between the 1st symmetric longitudinal simple thickness resonance and 1st symmetric transverse simple thickness resonance occurs (conical point).

Lamb waves were excited using a contact transducer (Olympus v109) with an aperture of 12.7 mm coupled to the sample with a thin oil layer. The transducer was driven by a 5 cycle sine wave at 2.0 MHz from a function generator that was coupled to a 50 dB power amplifier. The resulting normal displacement of the sample was detected using an adaptive photorefractive crystal based interferometer which used a bismuth silicon oxide crystal. A 5.0 kHz, 3.0 kV field was applied to the crystal to enhance two-wave mixing gain. The laser source for the interferometer was a single longitudinal mode frequency doubled Nd:YAG laser with an output of 150 mW. The turning mirrors on the signal leg of the interferometer were mounted on a 2-axis translation stage in order to measure the displacement field over the plate surface. The output of the interferometer was sent through a 1.9 MHz analog high pass filter and recorded on a digital oscilloscope. Time domain responses were measured as the source to receiver distance was increased in 200 μm steps for a total distance of 20 mm, starting 100 mm away from the center of the transducer. The measured waveforms gave the temporal response as a function of distance and were processed with a two-dimensional FFT which then gave the temporal frequency as a function of spatial frequency. The wavenumber associated with the peak magnitude in Fourier space was found from 1.95 – 2.15 MHz in order to extract the dispersion curve of the S_2 mode near $k = 0$. This dispersion curve, along with the theoretical dispersion curve calculated using the Rayleigh-Lamb frequency equation, is shown in Fig. 5.7. The coincident frequency is found to be 2.04 MHz.

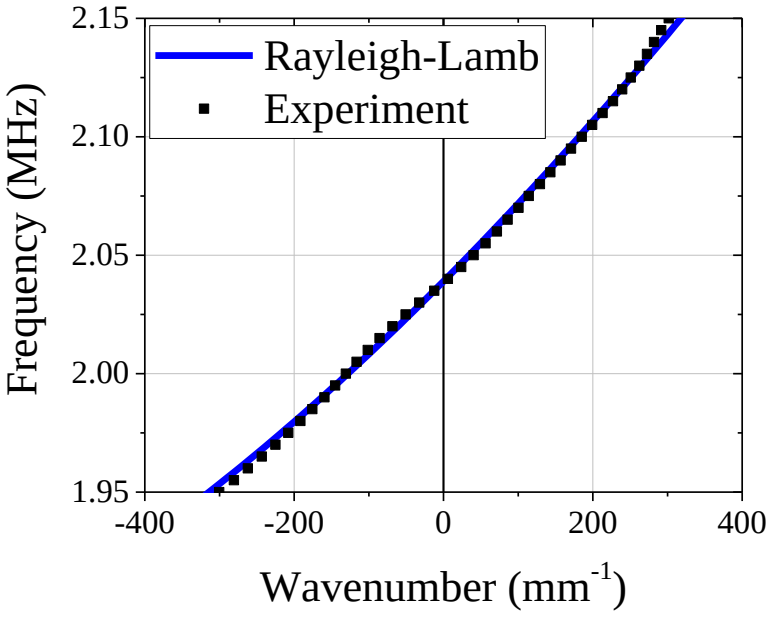

Fig. 5.7 Experimentally measured dispersion curve near $k = 0$ for a 6061-O aluminum plate cooled to ~ -5°C and theoretical curve (c_T = 3.138 mm/μs, $c_L = 2c_T$, and H = 1.539 mm).

Using the above results, the behavior of a conical point Lamb wave scattering from a hole in a plate is examined. A 6 mm diameter hole was drilled near the center of the plate. The excitation transducer was located 100 mm from the center of the hole. Lamb waves were excited by driving the transducer with a continuous 2.04 MHz sine wave from a function generator coupled to a power amplifier. The peak-to-peak amplitude from the function generator was 300 mV and the power amplifier gain was 50 dB. The output from the interferometer was fed to an rf lock-in amplifier. The reference signal for the lock-in came from the function generator. The lock-in time constant was 10 μs with a 12 dB per octave roll-off and the signal acquisition time was 70 μs. The plate was placed in a cooling chamber and cooled to ~ -5°C for the experiment. The experimental setup is shown in Fig. 5.8.

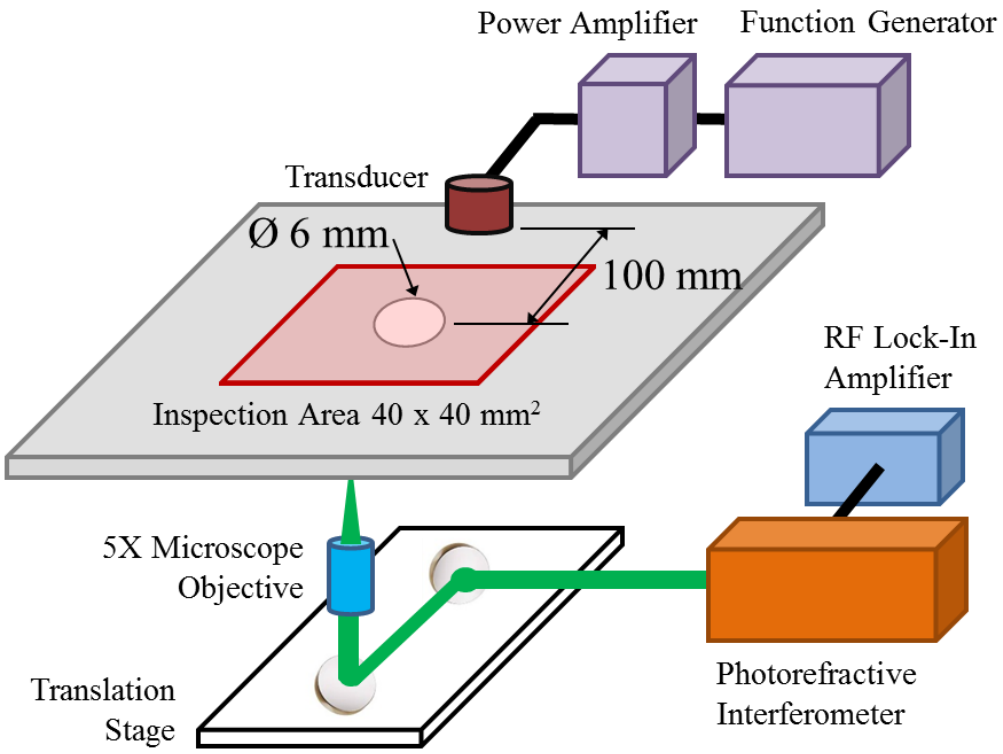

Fig. 5.8 Experimental setup for measuring scattering of Lamb waves with conical dispersion from a hole in a plate.

A simulation of the experiment was performed using PZFLEX where the model parameters were chosen to match the experiment. The experimental and numerical results are shown in Fig, 5.9. The results have some similar and some different features than the findings shown in Section 5.2. The raw data for the in-phase component of the displacement field is shown in Fig. 5.9 (a) and (d) for the simulation and experiment, respectively. One difference from the previous results is the presence of additional modes generated from the source, as evident by the nearly planar S_0 mode propagating in the *x*-direction. This is due to the top hat shape of the source which excites higher spatial modes due to its sharp edge. The primary modes

excited are the S_2 (conical point) mode and the S_0 mode. Because the S_0 mode is also mode converted (scattered) from the hole, the steady state results shows interference between the incident S_0 field and scattered S_0 field. The presence of the conical point mode appears as a DC offset in the displacement data. The behavior of the conical point Lamb wave can be observed by applying a low pass filter ($k = 0.5$ mm^{-1}) to the data, as shown for the displacement magnitude in Fig. 5.9 (b) and (e) for the simulation and experiment, respectively and for the displacement phase angle in Fig (c) and (f) for the simulation and experiment, respectively. The magnitude and phase of the conical point mode appears unperturbed by the hole. There is a small amount of spatial variation in the magnitude due the geometric decay of the source and from variations in the interferometer sensitivity for the experimental data. The geometric decay was not present in the previous results because a line source was used. The phase is almost perfectly uniform around the hole. These results confirm that in the long wavelength limit ($k \rightarrow 0$), a conical point Lamb wave will flow around a finite sized hole and the field distal to the hole is undisturbed.

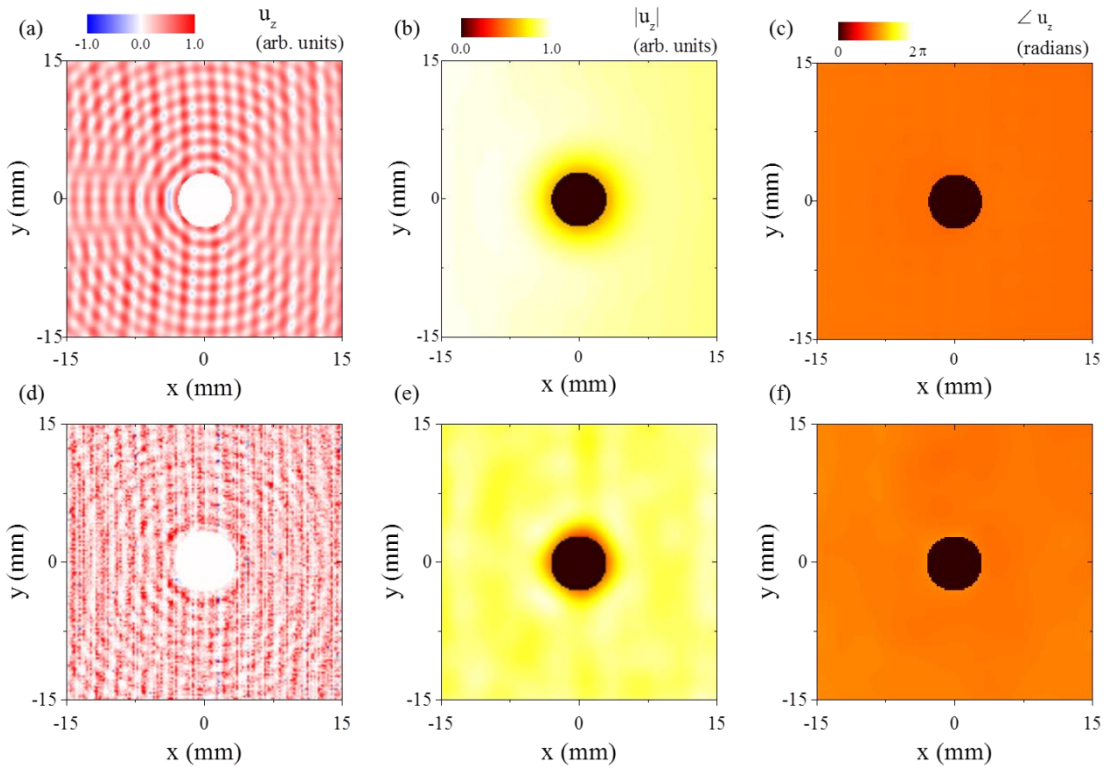

Fig. 5.9 Raw data for the in-phase normal displacement of a plate subject to a CW excitation at 2.04 MHz. The simulation results are shown in (a) and the experimental results shown in (d). The magnitude of the normal displacement after processing with a low pass filter (k = 0.5 mm^{-1}) for the simulation (b) and experiment (e). The phase angle of the normal displacement after processing with a low pass filter (k = 0.5 mm^{-1}) for the simulation (c) and experiment (f).

5.4. Simulations demonstrating pseudo cloaking of finite sized scatterers using Lamb waves with conical dispersion at $k = 0$

It has been demonstrated that Lamb waves with extremely long wavelength, due to conical dispersion at $k = 0$, will "flow" around a finite sized hole and that the distal field is unperturbed. This means that the hole is essentially invisible or cloaked in the long wavelength field. A striking demonstration of this phenomenon can be achieved by creating a small, symmetric, thickness change in the plate distal to hole. In the thinner section of the plate the dispersion curves are shifted and consequently the incident waves will undergo mode conversion at the

interface. The goal here is to design the step so that a conical point Lamb wave will uniquely convert to at least one other mode in the thinner portion of the plate. If the hole is actually cloaked, this mode converted field should be independent of the presence or geometry of the hole. Also, because the conical point wave has an infinite phase velocity, if the interface is flat the mode converted field will also consist of plane waves (as shown in Chapter 4).

The thickness step in the plate is chosen by examination of the dispersion curves. Specifically, Fig. 5.10 shows the dispersion curves for a plate with c_T = 3.0 mm/μs, $c_L = 2c_T$, and H_1 = 1.5 mm, and H_2 = 1.4 mm.

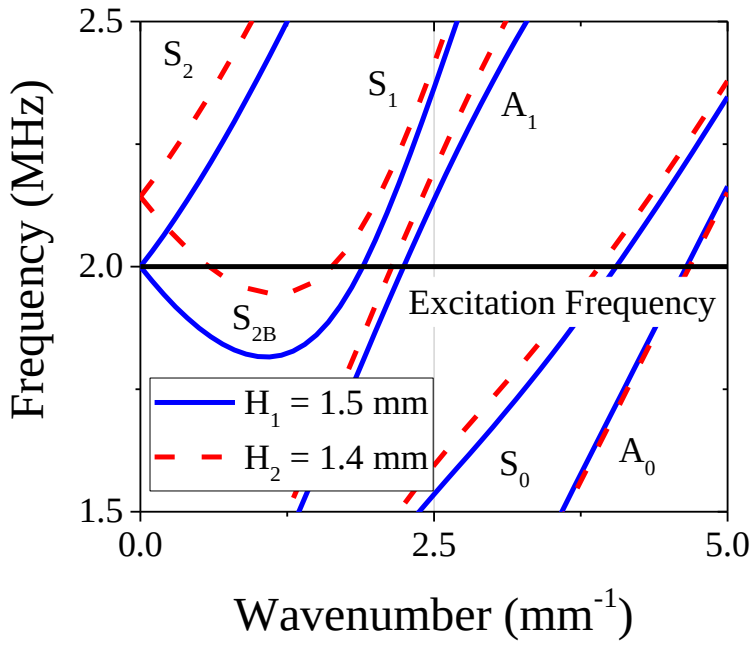

Fig. 5.10 Dispersion curves for plate with c_T = 3.0 mm/μs, c_L = 2cT, H_1 = 1.5 mm, and H_2 = 1.4 mm. At the coincident frequency (2 MHz) in the thicker side of the plate, the thinner side of the plate has an S_{2B} mode at k ~ 0.6 mm^{-1}.

At the conical point frequency in the 1.5 mm thick plate there exist an S_{2B} mode in the thinner side of the plate with $k = 0.6$ mm^{-1}. Simulations confirm that when incident waves from a top hat source, consisting of the conical point mode, S_1 mode, and S_0 mode, mode convert at the interface to the 1.4 mm thick portion of the plate, only the conical point wave mode converts to this S_{2B} mode. This is likely due to the long, with respect to the other incident modes, wavelength of the S_{2B} mode.

A finite difference simulation was performed where Lamb waves were excited in a plate by a 12.5 mm diameter top hat force applied normal to the surface. The excitation frequency was 2.0 MHz. The excitation source was located 40 mm in the *x*-direction from a 20 mm diameter hole. The source was also located 80 mm in the *x*-direction from a symmetric step in the plate thickness. The elastic properties and thicknesses of the plate were the aforementioned parameters in the dispersion curves shown in Fig. 5.10. The normal displacement is shown at times = 12, 23, 44, and 110 μs in Fig. 5.11 (a), (b), (c), and (d), respectively. The source is observed to generate mainly the conical point mode and secondarily the S_0 mode (as previously shown). The conical point mode is seen to "flow" around the hole, as demonstrated in Section 5.2. Here, however, there is a mode converted field at a thickness change in the plate. The mode converted S_{2B} field arises uniquely from the incident conical point mode. This field is observed to consist of plane waves and does not show any perturbation from the 20 mm diameter hole. These results again confirm that the conical point Lamb wave flows around the hole without distortion. The mode converted field from the conical point Lamb wave can also be observed as a circular field emanating, in phase, from the around hole. As previously noted, this field consists mostly of the S_0 mode.

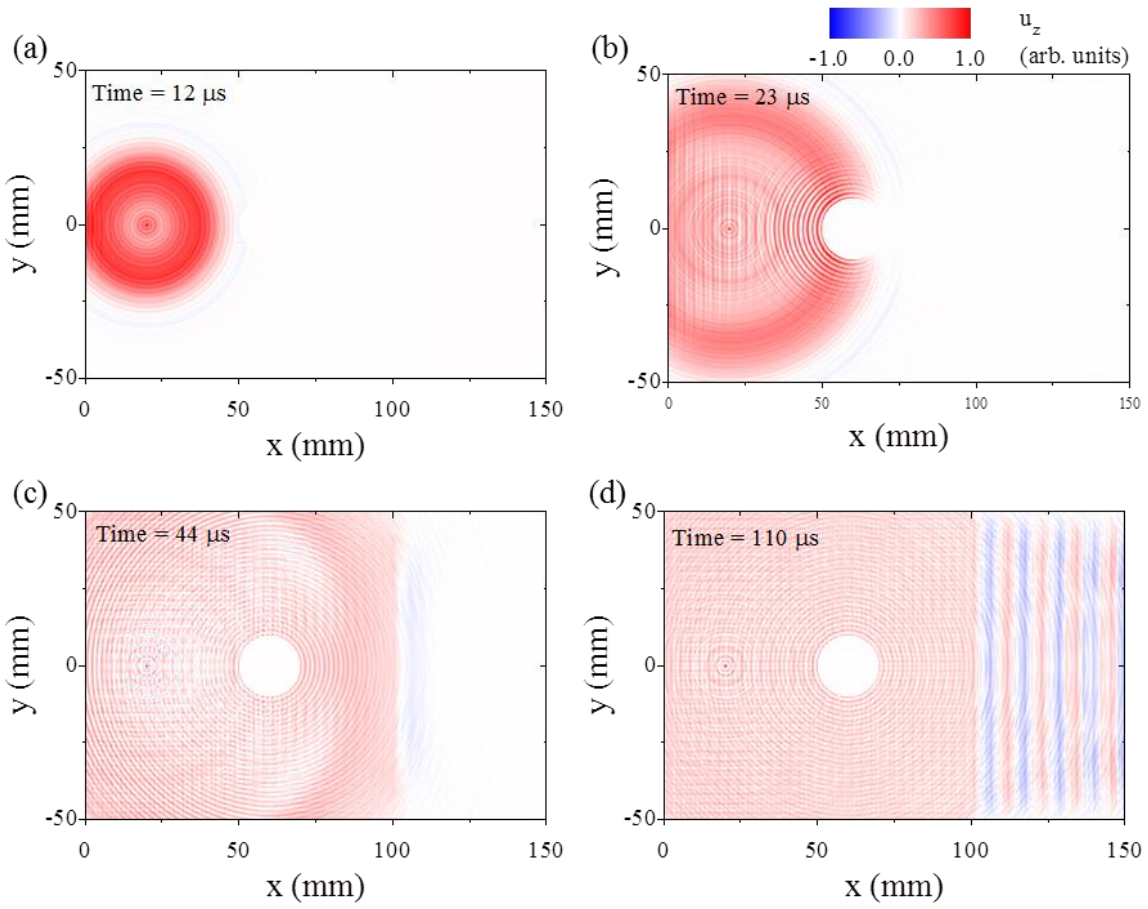

Fig. 5.11 Simulation results showing the normal displacement for a Lamb wave with conical dispersion at $k = 0$ propagating on a plate with a 20 mm diameter hole centered at $x = 60$ mm and a symmetric thickness step of 50 μm at $x = 100$ mm. The displacement is shown at t = 12, 23, 44, and 110 μs in (a), (b), (c), and (d), respectively.

Similar simulations were run with no hole, multiple holes, and a slit (aperture). The steady normal displacement field for no hole, one 20 mm diameter hole, three 24 mm diameter holes, and a 14 mm wide aperture are shown in 5.12 (a), (b), (c), and (d), respectively. Each of the results in Fig 5.12 exhibits a mode converted S_{2B} field consisting of plane waves. In each case, the mode converted S_{2B} mode appears spatially uniform in the *y*-direction. The magnitude of the S_{2B} field is observed to decrease in the cases where scatterers are present, with the most

noticeable effect in 5.12 (c) and (d), where the scatterers constituent a significant portion of the plate's cross-sectional area.

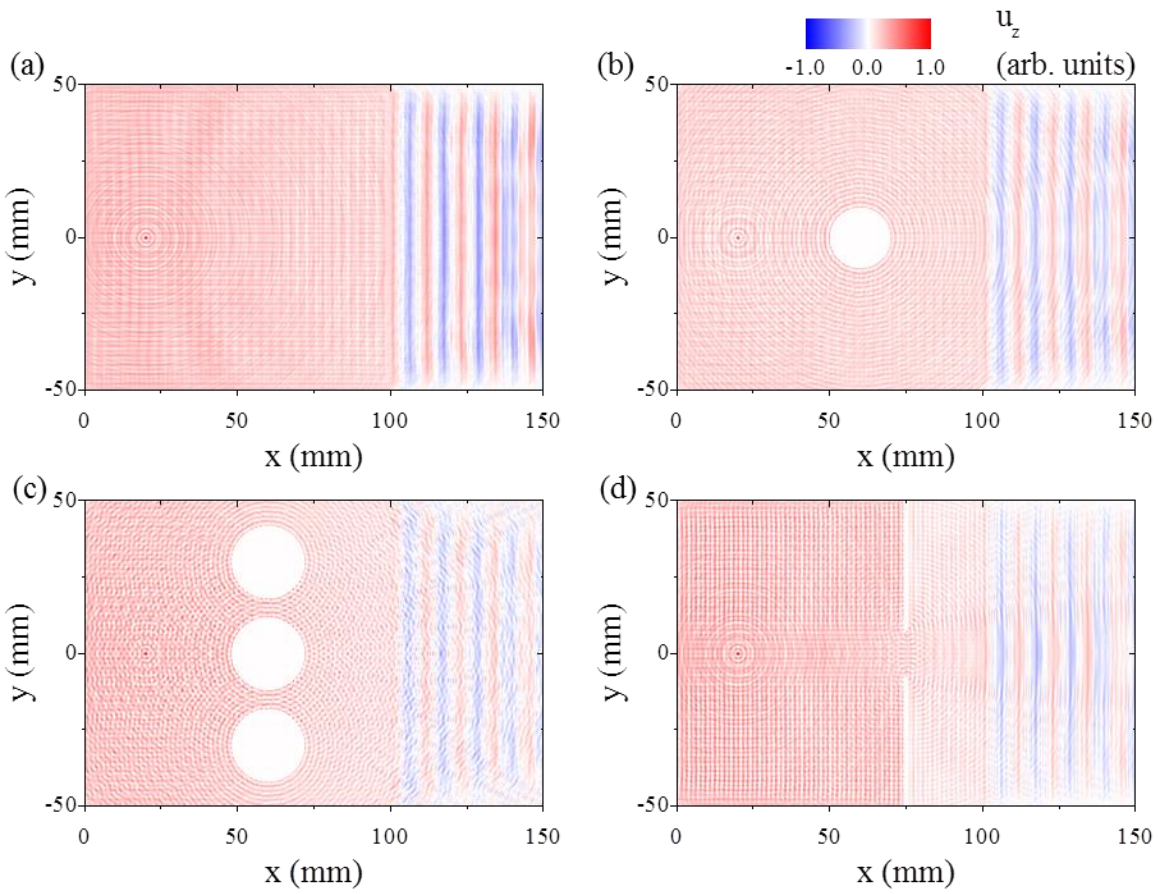

Fig. 5.12 Simulation results showing the steady state normal displacement field for a Lamb wave with conical dispersion at $k = 0$ propagating on a plate with a symmetric thickness step of 50 μm at $x = 100$ mm and various scattering geometry. (a) No hole. (b) One 20 mm diameter hole located at $x = 60$ mm. (c) Three 24 mm diameter holes $x = 60$ mm, (d) A 14 mm wide aperture located at $x = 75$ mm.

The source of this magnitude decrease is likely from the conical point mode losing energy due to mode conversion. Interestingly, the magnitude reduction appears to be spatially uniform distal to the scatterers, unlike the shadowing effect that occurs when finite wavelength waves scatter from

holes. These simulations demonstrate how a Lamb wave with conical dispersion can be used to hide the presence of finite sized scatterers.

5.5. Experimental demonstration of pseudo cloaking a finite sized hole using Lamb waves with conical dispersion

The previous section used numerical simulations to show that Lamb waves with conical dispersion at $k = 0$ can be used to hide scatterers when observing a distal mode converted field. Here, the same principle is demonstrated experimentally. The 610 x 305 mm^2 6061-O aluminum plate used in the experiments from Chapter 4 was used here. To begin, about half of the plate was dipped in an acid bath in order to symmetrically remove material. The thickness after dipping was measured to be 1.450 ± 0.003 mm. Then, a 20 mm diameter hole was drilled in the thicker side of the plate, 48 mm away from the thickness step. Near conical point Lamb waves were excited in the plate using the experimental procedure previously detailed in Section 5.3, with the exception that the transducer was driven at 2.051 MHz. Previous experiments have shown that at this frequency an S_2 mode can be effectively generated which has a wavelength of approximately 200 mm. A diagram of the experimental setup is shown in Fig. 5.13.

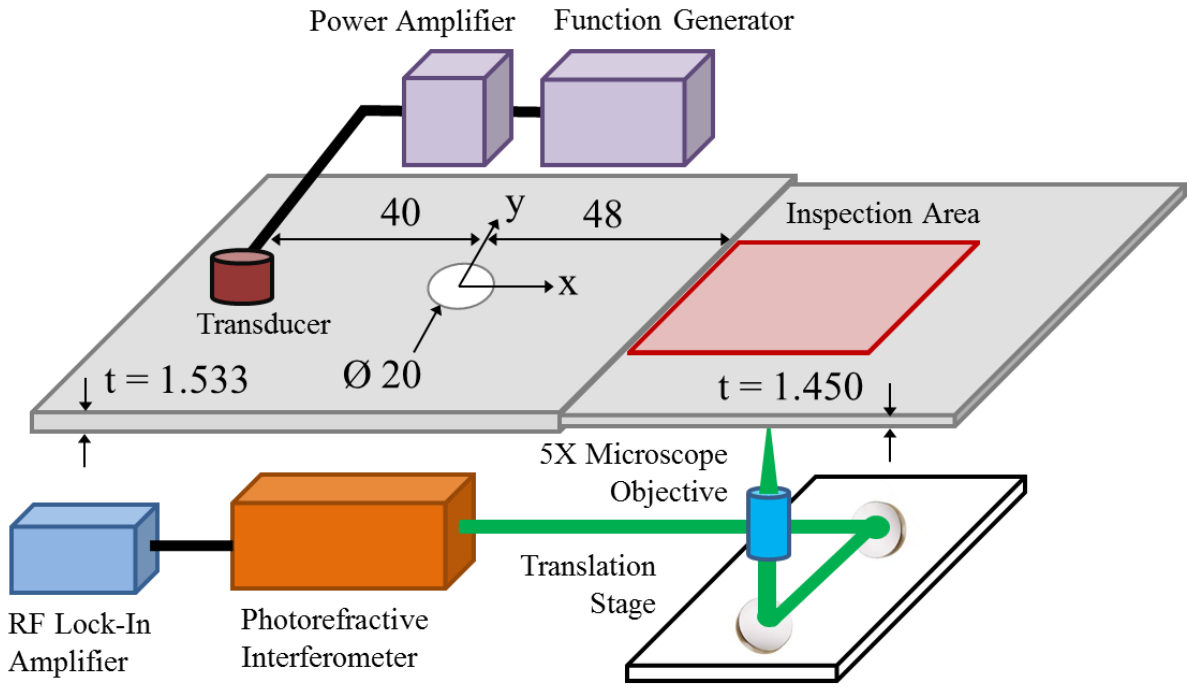

Fig. 5.13 Experimental setup for demonstrating pseudo cloaking of hole in a plate by a Lamb with conical dispersion by measuring a mode converted field distal to the hole.

The normal displacement was measured in the mode converted field over the 58 x 60 mm^2 area depicted in Fig. 5.13. The dispersion curves for both sides of the plate are shown in Fig. 5.14 where the excitation frequency is indicated. The elastic constants and thickness for the plate at room temperature were previously measured to be c_T = 3.125 mm/μs, c_L =6.272, and H = 1.533 mm.

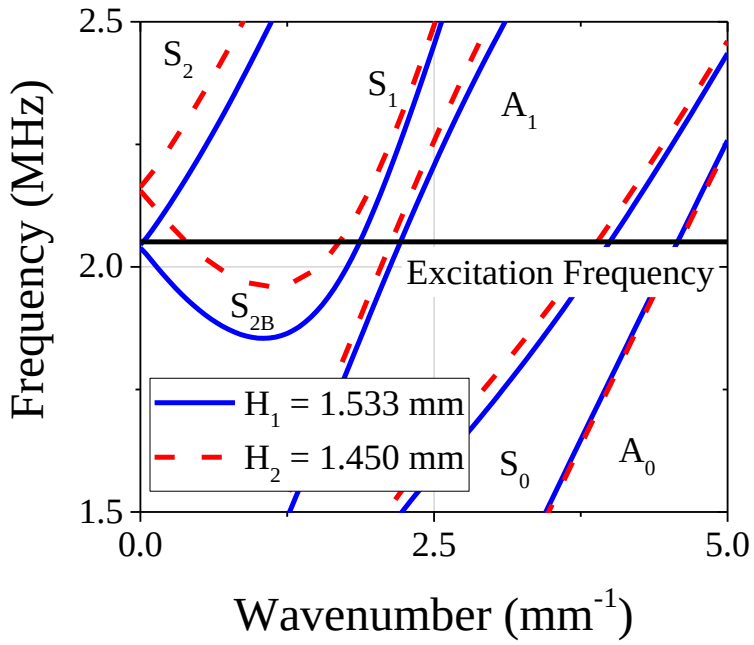

Fig. 5.14 Dispersion curves for plate with c_T = 3.125 mm/μs, c_L = 6.272 mm/μs, H_1 = 1.533 mm, and H_2 = 1.450 mm. At 2.051 MHz the S_2 mode in the thicker side of the plate has a wavelength ~ 200 mm and in the thinner side of the plate the S_{2B} mode has a wavelength ~ 14.5 mm.

The raw data for the in-phase component of the normal displacement is shown in Fig. 5.15 (a) and processed with a low pass filter (k = 1.0 mm^{-1}) in Fig. 5.15 (b). The displacement field consists of plane waves and appears unperturbed by the presence of the hole. These results again confirm that in the long wavelength a Lamb wave will "flow" around a finite sized hole and effectively hide it when observing the distal field or a mode converted distal field originating from the conical point wave.

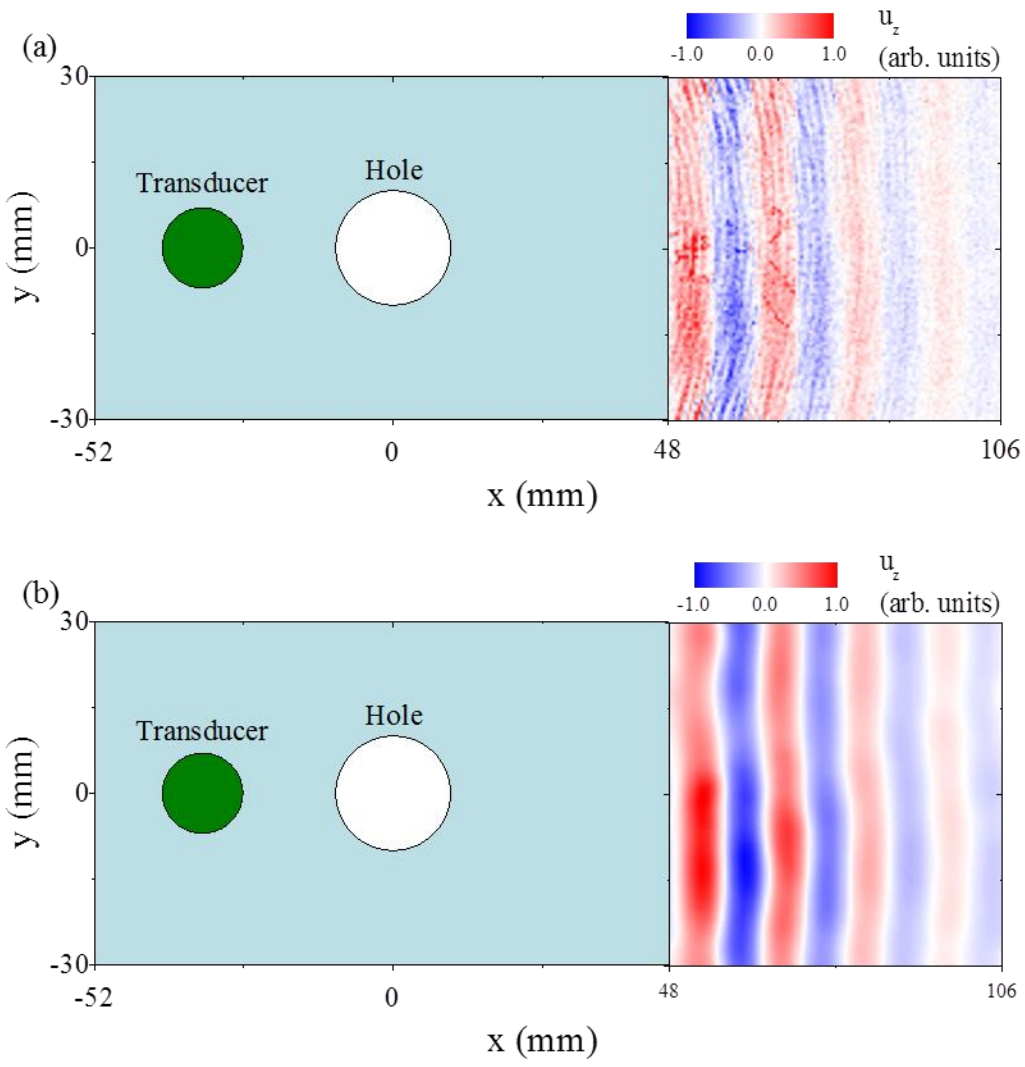

Fig. 5.15 Normal displacement of mode converted field distal to a 20 mm diameter hole in a 6061-O aluminum plate. The in-phase component of the raw data is shown in (a) and the after a low pass (k = 1.5 mm^{-1}) is shown in (b).

5.6. Conclusions and Significance of Findings

Numerical simulation and experiment demonstrate that a Lamb wave with conical dispersion at k = 0 will flow around a finite sized hole in a plate without field distortion. The incident Lamb wave mode converts from the hole. The mode converted field will look like it

emanates from a source with the same geometry as the scatterer. That is, it will be equal in magnitude and phase along the boundary of the scatterer. The incident field was observed to lose energy due to mode conversion distal to scatterers. This energy loss was small and only noticeable in cases where the scatterers constituted a significant portion of the plate's cross-sectional area.

Numerical simulation and experiment showed how a conical point Lamb wave can be used to hide scatterers when observing the distal field. Specifically, a small symmetric thickness change in a plate was used to observe a mode converted field from a conical point Lamb wave distal to various scatterers. When measuring only the S_{2B} mode converted field, without knowledge of the source strength, it was not possible to determine the presence, number, or size of the scatterers.

These are the first findings into how a Lamb wave with conical dispersion at $k = 0$, excited at the $k = 0$ frequency, interact with holes and other scatterers in a plate. These results indicate that such waves are undisturbed by the presence of one more finite sized scatterers with the exception of energy lost due to mode conversion.

5.7. References

[1] J. L. Rose, *Ultrasonic Waves in Solid Media* (Cambridge University Press 1999).

[2] L. Adler and J. D. Achenbach, "Elastic Wave Diffraction by Elliptical Cracks: Theory and Experiment," JNE 1, 2 (1980).

[3] Jan D. Achenbach, Laszlo Adler, D. Kent Lewis, and Harry McMaken, "Diffraction of ultrasonic waves by penny-shaped cracks in metals: Theory and experiment," J. Acoust. Soc. Am, 113(3), 1417 (2003).

[4] J. E. Gubernatis, E. Domany, J. A. Krumhansl, and M. Huberman, "The Born approximation in the theory of the scattering of elastic waves by flaws," J. Appl. Phys. 48, 2812 (1977).

[5] J. B. Keller, "Geometrical Theory of Diffraction," J. Opt. Soc. Am. 52, 116-130 (1962).

[6] J. D. Achenbach and A. K. Gautesen, "Geometrical theory of diffraction for three-D elastodynamics," J. Acoust. Soc. Am 61, 413 (1977).

[7] T. Grahn, "Lamb wave scattering from a circular partly through-thickness hole in a plate." Wave Motion 37, 1 (2003).

[8] D. M. Stobbe and T. W. Murray, "Conical dispersion of Lamb waves in elastic plates," Phys. Rev. B 96, 144101 (2017).

[9] S. Rokhlin, "Diffraction of Lamb waves by a finite crack in an elastic layer," J. Acoust. Soc. Am. 67, 1157 (1980).

[10] L. J. Crane, M. D. Gilchrist, and J. J. H. Miller, "Analysis of Rayleigh–Lamb wave scattering by a crack in an elastic plate," Comput. Mech.19, 6 (1997).

[11] X. Wang, C. Ying, M. Li, "Scattering of antiplane shear waves by a circular cylinder in a traction free plate," J. Acoust. Soc. Am. 108, 913 (2000).

[12] C. C. Mow and L. J. Mente, "Dynamic Stresses and Displacement Around Cylindrical Discontinuities Due to Plane Harmonic Shear Waves," J. Appl. Mech. 30 (1963).

[13] Y. Pao, "Dynamical Stress Concentration in an Elastic Plate," J. Appl. Mech. 29 (1962).

[14] O. Diligent, T. Grahn, A. Boström, P. Cawley, and M. Lowe, "The low-frequency reflection and scattering of the S_0 Lamb mode from a circular through-thickness hole in a plate: finite element, analytical and experimental studies," J. Acoust. Soc. Am. 112, 2589 (2002).

[15] M. Koshiba, S. Karakida, and M. Suzuki, "Finite-element analysis of Lamb wave scattering in an elastic plate waveguide," IEEE Trans. Sonics Ultrason. 31 (1984).

[16] Y. Al-Nasser, S. Datta, and A. Shah "Scattering of Lamb waves by a normal rectangular strip weldment," Ultrasonics, 29, 2 (1991).

[17] Z. Chang and A. Mal, "Scattering of Lamb waves from a rivet hole with edge cracks," Mech. Mater. 31, 3 (1999).

[18] Y. Cho and J.L. Rose, "An elastodynamic hybrid boundary element study for elastic guided wave interaction with a surface breaking defect," Int. J. Solids Struct. 37, 30 (2000).

[19] P. J. Torvik, "Reflection of Wave Trains in Semi-Infinite Plates," J. Acoust. Soc. Am. 41, 346 (1967).

Chapter 6

Conclusions

6.1 Summary of work

Lamb waves exhibit conical dispersion at zero wavenumber in isotropic homogenous plates for discrete values of Poisson's ratio. At these values of Poisson's ratio (v) longitudinal simple thickness resonances and shear simple thickness resonances, of the same symmetry, occur at the same frequency and degenerate. In the case of degeneracy, the dispersion curves become linear at zero wavenumber instead of parabolic. This occurs because of the interaction between the stress and displacement fields of the two coincident simple thickness resonances. In Chapter 2 the group velocity of a Lamb wave resulting from coincident simple thickness resonances was calculated by deriving the velocity of energy transport along the wave guide using the displacement field solutions of the two simple thickness resonances. The result agreed with the group velocity previously calculated by Mindlin, who considered the slope of the dispersion

curve for $k \rightarrow 0$ in the degenerate case. The theoretical response of a plate to an impulsive force was considered for the degenerate case of $\nu = ⅓$. The displacement response showed that a wave with an infinite phase velocity propagated away from the source at a finite group velocity and left the plate "ringing" in its wake. The ringing frequency was equal to the degenerate frequency and the vibrations were spatially in-phase (uniform).

In Chapter 3 a laser source was used to excite zero group velocity resonances in aluminum plates in order to measure Poisson's ratio with a high degree of accuracy. Poisson's ratio was also measured as a function of temperature in order to determine at what temperature to cool a 6061-O aluminum plate in order to induce conical dispersion. The frequency dispersion, while the plate was cooled, and linear dispersion in the vicinity of zero wavenumber was confirmed in the transition from forward to backward propagating Lamb wave modes. This experiment confirmed the previously predicted conical dispersion of Lamb waves in the case of degeneracy between simple thickness resonances of the same symmetry. These results show that given the correct material parameters a simple plate can support propagating waves with an infinite wavelength.

In Chapter 4 the broad angle reflection of Lamb waves with conical dispersion from a free edge were studied using experiment and simulation. It was shown that mode converted reflection always occurred at an angle normal to the interface, agreeing with Snell's law. Experiment and simulation showed how a curved edge of a plate could be used to focus mode converted reflections from a conical point wave. Specifically, an experiment was conducted where an S_0 mode was lensed from a semi-circular edge. The experiment showed that the mode conversion was uniform for the full 180° of the edge. This confirmed that the incident conical

point Lamb wave was spatially uniform. Examining time traces of just the incident mode also confirmed that it was oscillatory in time but spatially uniform.

In Chapter 5 the scattering behavior of Lamb waves with conical dispersion was investigated. It was demonstrated that Lamb waves with conical dispersion flow around finite sized scatterers without field distortion. The conical point wave field did lose energy due to mode conversion from the scatterer, but the phase of unperturbed. The mode converted field emanated from around the scatterer with unvarying magnitude and phase and made the scatterer appear as a pseudo-source for the mode converted field. Numerical simulation and experiment also showed that a conical point Lamb wave hides scatterers in the long wavelength field. Observing a mode converted field from just the conical point wave distal to the scatterers, it was not possible to determine the presence, number, or size of the scatterers.

6.2 Future work

Based on this author's research on Lamb waves with conical dispersion with zero wavenumber, the following are suggestions for improvement and additional topics on this work.

A source of complication when performing the experiments detailed in this thesis was the need to cool the plate in order to induce a true degeneracy. This involved implementing a cooling apparatus capable of reaching and maintaining -5 ^{o}C while allowing access for detection and sometimes excitation lasers. The setup was cumbersome and made isolating the sample from vibration extremely difficult. One solution to this problem is to create a plate that has a degenerate value of Poisson's ratio at room temperature. One technique suggested by Maznev was to create a bi-layer sample. This could be done by iteratively spin coating material onto a

plate and then measuring ν until the desired value was reached. However, another approach could be to design an alloy which intrinsically had a degenerate value of ν. This approach seems possible based on the measurements made by this author on aluminum alloys. The aluminum alloys tested all had ν very close to ⅓, with 6061-O being the closest. The tested alloys only differed by small amounts or alloying elements or by the type of heat treatment. These differences manifested in small differences in ν between the alloys. It is likely that an alloy could be designed which had $\nu \approx \frac{1}{3}$ at room temperature. This would allow greatly simplify the experiments. It would also make for an interesting new type of alloy, where this alloy would be distinguished by having conical dispersion or zero index of refraction at specific frequencies.

An improvement for experimentally studying Lamb waves with conical dispersion would be to use a source function that is Gaussian in space. Simulations and experiments demonstrated that transducers generate high spatial modes in addition to the conical mode. Transducers were selected over a laser based thermo-elastic source, which would have been Gaussian, because they generate normal forces, which were shown to couple into the conical mode much more efficiently than shear forces. The presence of these additional modes from the source complicates data interpretation. For instance, if the source only generated the conical point mode, the wavelength could be measured with extremely high accuracy by merely examining the phase delay between waveforms at two spatial locations. One way to generate a Gaussian normal force is to use a laser excitation and locally constrain the normal displacement of the sample. This was technique was briefly explored by this author; however, there was difficulty in getting repeatable measurements.

The following are some ways that Lamb waves with conical dispersion could be used to manipulate wave fields in other novel ways and possibly create devices. A conical point wave is

uniform in space. One consequence of this is that anywhere a wave mode converts from the conical point wave, at an interface, will be in phase. For example, imagine a conical point wave excited in a large plate with multiple exit locations located at different distances from the source. The mode converted waves at each exit interface will be in phase regardless of distance from the source. The conical point wave can be thought of as synchronizing all of the mode converted fields. This synchronization is interesting because it is independent of the position of the source or the exit points.

The scattering behavior of a conical point Lamb wave was studied in this manuscript but there are still some questions about the physics and ways a wave field could be manipulated. The most striking feature noted was how a conical point wave flows around holes without any distortion and with a small uniform decrease in magnitude, which was a result of energy lost to mode conversion. It would be interesting to quantify the energy lost to mode conversion in terms of the shape and size of the scatterer(s). Another interesting question is whether or not there is a type of scatterer that makes the steady state field of the conical point wave distal to the scatterer zero. This would represent a form of total reflection instead of the near total transmission that has been demonstrated with “free” holes. A scatterer that acts as an energy sink may have this effect.

In addition to the items listed above, there are other interesting wave field phenomena that have been demonstrated in the literature using zero-index of refraction meta-materials. This author would suggest that similar phenomena may exist in simple plates that exhibit conical dispersion.

Bibliography

A. A. Houck, J. B. Brock, and I. L. Chuang, “Experimental Observation of a Left-Handed Material That Obeys Snell’s Law”, Phys. Rev. Lett. 90, 137401 (2003).

A. A. Maznev and A. G. Every, “Surface acoustic waves with negative group velocity in a thin film structure on silicon”, Appl. Phys. Lett. 95, 011903 (2009).

A. A. Maznev, Dirac cone dispersion of acoustic waves in plates without phononic crystals, J. Acoust. Soc. Am. 135, 577 (2014).

A. Blouin and J. P. Monchalin, “Detection of ultrasonic motion of a scattering surface by two-wave mixing in photorefractive GaAs crystal,” Appl. Phys. Lett. 65, 932 (1994).

A. E. Love, *Some Problems of Geodynamics* (Cambridge University Press, Cambridge 1911).

A. E. Love, *Mathematical Theory of Elastic Systems* (McGraw-Hill Inc., New York 1944).

A. H. Meitzler, “Backward-Wave Transmission of Stress Pulses in Elastic Cylinders and Plates”, J. Acoust. So. Am. 38, 835 (1965).

A. Ramakrishna, “Physics of negative refractive index materials,” Rep. Prog. Phys. 68, 449 (2005).

A. L. Shuvalov, and O. Poncelet, “On the backward Lamb waves near thickness resonances in anisotropic”, Int. J. Solids Struct. 45, (2008).

A. Sukhovich, B. Merheb, K. Muralidharan, J. O. Vasseur, Y. Pennec, P. A. Deymier, and J. H.Page, "Experimental and theoretical evidence for subwavelength imaging in phononic crystals." Phys. Rev. Lett. 102, 154301 (2009).

B. A. Auld, *Acoustic Fields and Waves in Solids* (John Wiley and Sons, New York 1973).

B. Morvan, N. Wilkie-Chancellier, H. Duflo, A. Tinel, and J. Duclos, “Lamb wave reflection at the free edge of a plate,” J. Acoust. Soc. Am, 113(3), 1417 (2003).

B. Gérardin, J. Laurent, C. Prada, and A. Aubry, “Negative reflection of Lamb waves at a free edge: Tunable focusing and mimicking phase conjugation,” J. Acoust. Soc. Am. 140, 591 (2016).

C. C. Mow and L. J. Mente, “Dynamic Stresses and Displacement Around Cylindrical Discontinuities Due to Plane Harmonic Shear Waves,” J. Appl. Mech. 30 (1963).

C. M. Grünsteidl, I. A. Veres, and T. W. Murray, “Experimental and numerical study of the excitability of zero group velocity Lamb waves by laser-ultrasound.” J. Acoust. Soc. Am. 138, 242 (2015).

C. Prada. O. Balogun and T. W. Murray, “Laser-based ultrasonic generation and detection of zero-group velocity Lamb waves in thin plates,” Appl. Phys. Lett. 87, 194109 (2005).

C. Prada, D. Clorennec, and D. Royer, “Local vibration of an elastic plate and zero-group velocity Lamb modes,” J. Acoust. Soc. Am. 124, 203 (2008).

D. Clorennec, C. Prada, and D. Royer, “Local and noncontact measurements of bulk acoustic wave velocities in thin isotropic plates and shells using zero group velocity Lamb modes,” J. Appl. Phy. 101, 034908 (2007).

C. Prada, D. Clorennec, and D. Royer, Power law decay of zero group velocity Lamb modes, Wave Motion 45 (2008).

C. Zhang, C. T. Chan, and X. Hu, "Broadband focusing and collimation of water waves by zero refractive index," Sci. Rep. 4, 6979 (2014).

D. Clorennec, C. Prada, D. Royer, and T. W. Murray, "Laser impulse generation and interferometer detection of zero group velocity Lamb mode resonance," Appl. Phys. Lett. 89, 024101 (2006).

D. C. Worlton, "Experimental confirmation of Lamb waves at megacycle frequencies," J. Appl. Phys. 32 (1961).

D. M. Stobbe and T. W. Murray, "Conical dispersion of Lamb waves in elastic plates," Phys. Rev. B 96, 144101 (2017).

D. M. Stobbe and T. W. Murray, "Scattering of Lamb waves with conical dispersion in elastic plates", In Progress (2018).

E. A. Birt, "Damage detection in carbon-fibre composites using ultrasonic Lamb waves," Insight 40 (1998).

E. Cubukcu, K. Aydin, E. Ozbay, S. Foteinopoulou, and C. M. Soukoulis, "Electromagnetic waves: Negative refraction by photonic crystals", Nature (London) 423, 604 (2003).

E. R. Lapwood, *Philosophical Transactions of the Royal Society London,* 242 (1949).

F. D. Philippe, T. W. Murray, and C. Prada, "Focusing on Plates: Controlling Guided Waves using Negative Refraction", Sci. Rep. 5, 11112 (2015).

F. Liu, Y. Lai, X Huang, and C. T. Chan, Dirac cones at k = 0 in phononic crystals, Phys. Rev. B 84, 224113 (2011).

F. Liu, X. Huang, and C. T. Chen, Dirac cones at k = 0 in acoustic crystals and zero index acoustic materials, Appl. Phys. Lett. 100, 071911 (2012).

F. Liu and Z. Liu, Elastic Waves Scattering without Conversion in Metamaterials with Simultaneous Zero Indices for Longitudinal and TransverseWaves, Phys. Rev. Lett. 115, 175502 (2015).

G. Lamè, *Lessons on the mathematical theory of the elasticity of solid bodies,* Paris (1852).

H. Lamb, *Proceedings of the London Mathematical Society,* 21 (1890).

H. Lamb, *Philosophical Transactions of the Royal Society London,* 203 (1904).

I. A. Veres, C. Grunsteidl, D. M. Stobbe, and T. W. Murray, "Broad angle negative reflection and focusing of elastic waves from a plate edge," Phy. Rev. B. 93, 174304 (2016).

I. Bartolia, A. Marzania, F. di Scaleaa, and E. Violab, "Modeling wave propagation in damped waveguides of arbitrary cross-section," J. Sound Vib. 295 (2006).

I. Tolstoy, and E. Usdin, "Wave Propagation in Elastic Plates: Low and High Mode Dispersion", J. Acoust. So. Am. 29, 1 (1957).

Jan D. Achenbach, Laszlo Adler, D. Kent Lewis, and Harry McMaken, "Diffraction of ultrasonic waves by penny-shaped cracks in metals: Theory and experiment," J. Acoust. Soc. Am, 113(3), 1417 (2003).

J. B. Keller, “Geometrical Theory of Diffraction,” J. Opt. Soc. Am. 52, 116-130 (1962).

J. D. Achenbach and A. K. Gautesen, “Geometrical theory of diffraction for three-D elastodynamics,” J. Acoust. Soc. Am 61, 413 (1977).

J. D. Achenbach, *Wave Propagation in Elastic Solids* (North-Holland, Amsterdam, 1973).

J.D. Achenbach, “Quantitative nondestructive evaluation,” Int. J. Solids Struct. 37 (2000).

J. B. Pendry and S. A. Ramakrishna, “Focusing light using negative refraction,” 2003 J. Phys. Condens. Matter 15 6345.

J. B. Pendry, “Negative Refraction Makes a Perfect Lens”, Phys. Rev. Lett. 85, 3966 (2000).

J. B. Spicer, A.D.W. McKie, and J.W. Wagner, “Quantitative theory for laser ultrasonic waves in a thin plate,” Appl. Phys. Lett. 57, 1882 (1990).

J. E. Gubernatis, E. Domany, J. A. Krumhansl, and M. Huberman, “The Born approximation in the theory of the scattering of elastic waves by flaws,” J. Appl. Phys. 48, 2812 (1977).

J. Hao, W. Yan, and M. Qiu, Super-reflection and cloaking based on zero index metamaterial, Appl. Phys. Lett. 96, 101109 (2010).

J. L. Rose, *Ultrasonic Waves in Solid Media* (Cambridge University Press 1999).

J. Laurent, D. Royer, and C. Prada, “Temporal behavior of laser induced elastic plate resonances,” Wave Motion 51 (2014).

J. Miklowitz, *The Theory of Elastic Waves and Waveguides* (North Holland Publishing Company 1978).

L. Adler and J. D. Achenbach, “Elastic Wave Diffraction by Elliptical Cracks: Theory and Experiment,” JNE 1, 2 (1980).

L.. Cagniard, *Reflection and Refraction of Progressive Seismic Waves* (Mc-Graw-Hill Inc. New York, 1962).

L. J. Crane, M. D. Gilchrist, and J. J. H. Miller, “Analysis of Rayleigh–Lamb wave scattering by a crack in an elastic plate,” Comput. Mech.19, 6 (1997).

L. Pochhammer, *Journal of Mathematics (Germany)*, 81 (1876).

Lord Rayleigh, *Proceedings of the London Mathematical Society,* 17 (1887).

Lord. Rayleigh, *Proceedings of the London Mathematical Society*, 20 (1889).

M. A. Biot, “General theorems on the equivalence of group velocity and energy transport,” Phys. Rev. 105 (1957).

M. Castaings and M. Lowe, “Finite element model for waves guided along solid systems of arbitrary section coupled to infinite solid media,” J. Acoust. Soc. Am. 123, 2 (2008).

M. Cès, D. Clorennec, D. Royer, and C. Prada, “Thin layer thickness measurements by zero group velocity Lamb mode resonances,” Rev. Sci. Instrum. 82, 114902 (2011).

M. Ibanescu, S. G. Johnson, D. Roundy, C. Luo, Y. Fink, and J. D. Joannopoulos, “Anomalous Dispersion Relations by Symmetry Breaking in Axially Uniform Waveguides”, Phy. Rev. Lett. 92, 6 (2004).

M. Germano, A. Alippi, A. Bettucci, and G. Mancuso, “Anomalous and negative reflection of Lamb waves in mode conversion”, Phys. Rev. B 85, 012102 (2012).

M. Koshiba, S. Karakida, and M. Suzuki, “Finite-element analysis of Lamb wave scattering in an elastic plate waveguide,” IEEE Trans. Sonics Ultrason. 31 (1984).

M. Lemistre, D.L. Balageas, “Structural health monitoring system based on diffracted Lamb wave analysis by multiresolution processing,” Smart Mater. Struct. 10 (2001).

M. Notomi, “Theory of light propagation in strongly modulated photonic crystals: Refractionlike behavior in the vicinity of the photonic band gap”, Phys. Rev. B 62, 10696 (2000).

M. R. Lindeburg, *Mechanical Engineering Reference Manual* (Professional Publications Inc., 2006).

M. Silveirinha and N. Engheta, Tunneling of Electromagnetic Energy through Subwavelength Channels and Bends using ε-Near-Zero Materials, Phys. Rev. Lett. 97, 157403 (2006).

M. V. Predoi, M. Castaings, B. Hosten, and C. Bacon, “Wave propagation along transversely periodic structures,” J. Acoust. Soc. Am. 121, 4 (2007).

M. Z. Silva, R. Gouyon, and F. Lepoutre, “Hidden corrosion detection in aircraft aluminium structures using laser ultrasonics and wavelet transform signal analysis,” Ultrasonics 41 (2003).

N. Fang, H. Lee, C. Sun, and X. Zhang, “Sub–Diffraction-Limited Optical Imaging with a Silver Superlens”, Science 308, 534 (2005).

N. Fang, D. Xi, J. Xu, M. Ambati, W. Srituravanich, C. Sun, and X. Zhang, “Ultrasonic metamaterials with negative modulus”, Nature Materials 5, 452-456 (2006).R. A. Shelby, D. R.

Smith, and S. Schultz, “Experimental Verification of a Negative Index of Refraction”, Science 292, 77 (2001).

O. Balogun, T. W. Murray, and C. Prada, “Simulation and measurement of the optical excitation of the zero group velocity Lamb wave resonance in plates,” J. Appl. Phy. 102, 064914 (2007).

O. Diligent, T. Grahn, A. Boström, P. Cawley, and M. Lowe, “The low-frequency reflection and scattering of the S_0 Lamb mode from a circular through-thickness hole in a plate: finite element, analytical and experimental studies,” J. Acoust. Soc. Am. 112, 2589 (2002).

P. L. Marston, “Negative group velocity Lamb waves on plates and applications to the scattering of sound by shells”, J. Acoust. Soc. Am. 38, 835 (1965).

Q. Wei, Y. Cheng, and X. Liu, Acoustic total transmission and total reflection in zero-index metamaterials with defects, Appl. Phys. Lett. 102, 174104 (2013).

R. D. Gregory and I. Gladwell, "The reflection of a symmetric Rayleigh-Lamb wave at the fixed or free edge of a plate," J. Elasticity 13(2), 185 (1983).

R. B. Nelson and S. B. Dong, “High Frequency Vibrations and Waves in Laminated Orthotropic Plates,” J. Sound Vib. 30 (1973).

R. Craster and S. Guenneau, “Acoustic metamaterials: Negative refraction, imaging, lensing and cloaking”, Springer-Verlag, London, (2012).

R. D. Mindlin, *An Introduction to the Mathematical Theory of Vibrations of Elastic Plates* (World Scientific, Singapore, 2016).

R. Liu, Q. Cheng, T. Hand, J. J. Mock, T. J. Cui, S. A. Cummer, and D. R. Smith, Experimental Demonstration of Electromagnetic Tunneling Through an Epsilon-Near-Zero Metamaterial at Microwave Frequencies, Phys. Rev. Lett. 100, 023903 (2008).

R. Stonely, *Proceedings of the London Mathematical Society*, 106 (1924).

S. A. Cummer, "Simulated causal subwavelength focusing by a negative refractive index slab", Appl. Phys. Lett. 95, 011903 (2003).

S. B. Dong and K. H. Huang, "Edge Vibrations in Laminated Composite Plates," J. Appl. Mech. 52 (1972).

S. B. Dong and R. B. Nelson, "On Natural Vibrations and Waves in Laminated Orthotopic Plates," J. Appl. Mech. (1972).

S. Bramhavar, C. Prada, A. A. Maznev, A. G. Every, T. B. Norris, and T. W. Murray, "Negative refraction and focusing of elastic lamb waves at an interface", Phys. Rev. B 83, 014106 (2011).

S.D. Holland, D. Chimenti, Air-coupled acoustic imaging with zero-group-velocity Lamb modes, Appl. Phys. Lett. 83, 2704 (2003).

S. D. Poisson, *Royal Academy of Science Paris*, 8 (1829).

S. Rokhlin, "Diffraction of Lamb waves by a finite crack in an elastic layer," J. Acoust. Soc. Am. 67, 1157 (1980).

S. Yang, J. H. Page, Z. Liu, M. L. Cowan, C. T. Chan, and P. Sheng, "Focusing of Sound in a 3D Phononic Crystal", Phys. Rev. Lett. 93, 024301 (2004).

Sylvain Mezil, Francois Bruno, Samuel Raetz, Jérôme Laurent, Daniel Royer, and Claire Prada, "Investigation of interfacial stiffnesses of a tri-layer using Zero-Group Velocity Lamb Modes" J. Acoust. Soc. Am. 138, 3202 (2015).

S. Zhang, L. Yin, and N. Fang, "Focusing Ultrasound with an Acoustic Metamaterial Network", Phys. Rev. Lett. 102, 194301 (2009).

Tables of Physical andChemical Constants, 16th ed. (Longmans, Green Co., 1995), 2.1.4 Hygrometry. Kaye & Laby Online, Version 1.0 (2005).

T. Grahn, "Lamb wave scattering from a circular partly through-thickness hole in a plate." Wave Motion 37, 1 (2003).

T. J. Delph, G. Herrmann, and R. K. Kaul, On coalescence of frequencies and conical points in the dispersion spectra of elastic bodies, Int. J. Solids Struct. 13, 423 (1977).

V. C. Nguyen, L. Chen, and K. Halterman, Total Transmission and Total Reflection by Zero IndexMetamaterials with Defects, Phys. Rev. Lett. 105, 233908 (2010).

V. G. Veselago and E.E. Narimanov , "The left hand of brightness: past, present, and future of negative index materials", Nature Material 5, (2006).

X. Huang, Y. Lai, Z. H. Hang, H. Zheng, and C. T. Chan, Dirac cones induced by accidental degeneracy in photonic crystals and zero-refractive-index materials, Nat. Mater. 10, 582 (2011).

X. Wang, C. Ying, M. Li, "Scattering of antiplane shear waves by a circular cylinder in a traction free plate," J. Acoust. Soc. Am. 108, 913 (2000).

Y. Al-Nasser, S. Datta, and A. Shah "Scattering of Lamb waves by a normal rectangular strip weldment," Ultrasonics, 29, 2 (1991).

Y. Cho and J.L. Rose, "An elastodynamic hybrid boundary element study for elastic guided wave interaction with a surface breaking defect," Int. J. Solids Struct. 37, 30 (2000).

Y. Pao, "Dynamical Stress Concentration in an Elastic Plate," J. Appl. Mech. 29 (1962).

Z. Chang and A. Mal, "Scattering of Lamb waves from a rivet hole with edge cracks," Mech. Mater. 31, 3 (1999).

Z.A.B. Ahmad and U. Gabbert, "Simulation of Lamb wave reflections at plate edges using the semi-analytical finite element method," Ultrasonics 52 (2012).

Appendix A: Numerical Study of Backward Propagating Lamb Waves

David M. Stobbe[1] and Todd W. Murray[1]

[1]*Department of Mechanical Engineering, University of Colorado at Boulder, Boulder, CO 80309*

Abstract

Elastic wave guides are capable of supporting backward propagating waves over certain frequency wavenumber spaces. For the case of a homogenous and isotropic plate, a Lamb wave at a specific frequency and wavenumber can occur as a forward propagating mode or as a backward propagating mode, depending on the plate thickness. Negative refraction will occur when a forward mode converts to a backward mode *(and vice versa)*. This paper explores mode conversion between forward and backward propagating Lamb waves using numerical simulations of elastic plates. Steering and focusing a Lamb wave field using negative refraction is demonstrated and analyzed. Mode conversion between forward and backward modes as a function of incident angle and interface geometry is also explored. Finally, it is demonstrated that a point source can be partially cancelled by an adjacent anti-source by employing forward and backward Lamb waves. We propose that an understanding of the existence and behavior of backward propagating Lamb waves may lead to unique ways of manipulating acoustic energy for the purpose of nondestructive testing and the creation of new acoustic devices.

I. Introduction

Recent work in acoustics and optics has shown that wave fields can be controlled and manipulated in novel ways using backward propagating waves. Materials that display backward wave motion are known to exist in electro-magnetic and mechanical metamaterials [1-4], photonic and phononic crystals [5-7], and mechanical and electro-magnetic wave guides [0-13]. One unique quality of materials that support backward waves is that they have a negative index of refraction [14]. Negative refraction can lead to unusual physical behavior including focusing a wave field from a flat interface [15-24]. Backward waves behave such that their phase velocity (c_p) and group velocity (c_g) are anti-parallel. A forward propagating wave converted to a backward propagating wave *(or vice versa)* will undergo negative refraction, meaning that the angle of refraction will be greater than the interface normal. Recent experiments have demonstrated that negative refraction can be used to create a flat tunable acoustic lens with a simple elastic plate [22,24]. This was accomplished by mode converting a forward propagating Lamb wave to a backward propagating Lamb wave *(and vice versa)* at a simple geometric trough in a plate.

The existence of backward propagating mechanical waves was first mentioned by Lamb [25]. Backward wave propagation in plate waveguides *(Lamb waves)* was first discussed in detail by Tolstoy and Usdin [0]. Lamb waves are generally dispersive and exhibit both normal and anomalous dispersion and consist of both propagating and decaying modes according to the Rayleigh – Lamb dispersion relationship [26]:

$$\frac{\omega^4}{c_T^2} = 4k^2q^2\left(1 - \frac{p}{q}\frac{\tan(ph+\alpha)}{\tan(qh+\alpha)}\right),\ with\ \ q^2 = \frac{\omega^2}{c_T^2} - k^2,\ p^2 = \frac{\omega^2}{c_L^2} - k^2,\ and\ \ \alpha \in \left\{0, \frac{\pi}{2}\right\} \qquad (1)$$

where c_L, c_T, ω, k, and 2h are the longitudinal wave speed, shear wave speed, angular frequency, wave number, and plate thickness, respectively. The modes of wave propagation are defined as symmetric *(α = 0)* or anti-symmetric *(α = π/2)* according to their displacement about the plate mid-plane. The frequency and wavenumber space that backward waves occur can be identified by plotting the dispersion mode curves on an ω versus k plot as shown in Fig. 1. The phase and group velocities are defined as: $c_p = \omega/k$ and $c_g = d\omega/dk$, respectively. Examining Fig. 1 it is clear that, for a 1 mm thick aluminum plate, the S_2 mode exhibits opposite signed phase and group velocities in the range of 2.85 – 3.15 MHz, colored red in Fig. 1. This portion of the S_2 mode is referred to as the S_{2B} mode and for this portion of this mode backward wave propagation will occur. In general, backward wave regions are possible in all of the modes except for the first three: A_0, S_0, and A_1. The frequency and wavenumber space in which backward waves exist, for a given mode, is a function of the material's Poisson's ratio [0]. Additionally, changing the thickness of a plate will shift the dispersion curve up and down and compress and extend it. Using this property, a plate can be designed with two different thicknesses, where one thickness supports a forward propagating mode and the other thickness supports a backward propagating mode, at the same frequency. For example, an aluminum plate that is 1.2 mm thick on one half and 1.0 mm thick on the other half will support a forward S_2 mode and a backward S_{2B} mode, respectively, over the frequency range of 2.85 – 3.15 MHz.

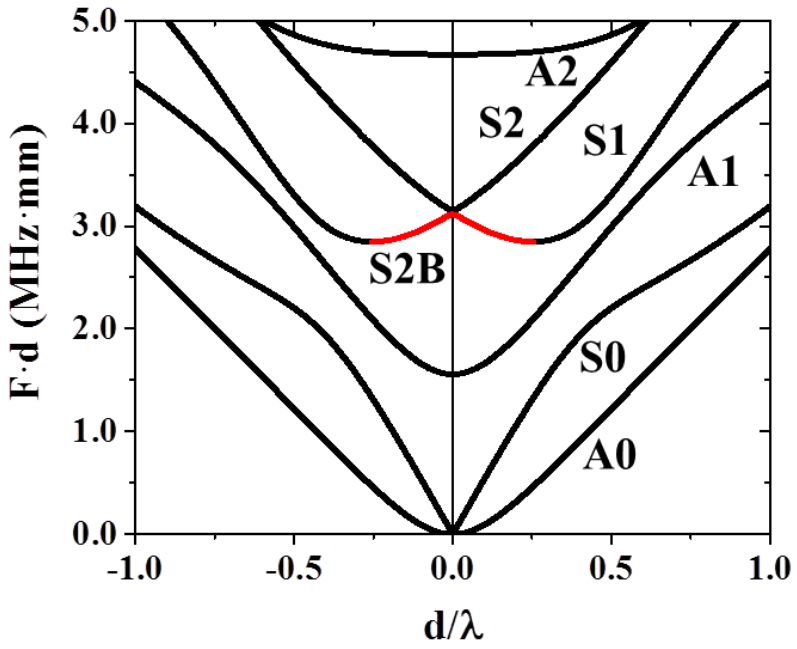

Fig. 1: Dispersion curve for 1.0 mm thick aluminum plate. The first six propagating modes are shown. The sections in red are the backward wave portions of the S_2 mode and are labeled as S_{2B}.

These two modes will cross at a wavenumber of 0.131 mm^{-1}, as shown in Fig. 2 (a). Consequently, when excited near this frequency and wavenumber, a forward propagating S_2 mode can be partially mode converted to a backward propagating S_{2B} mode at the thickness change. This mode conversation will result in negative refraction of the S_{2B} mode. In general, if a plate experiences an abrupt change in thickness, a propagating Lamb wave will mode convert at the thickness change, reflecting some modes and transmitting others. The composition of the modes reflected and transmitted depends on satisfying the interface boundary conditions, which, in the case of a symmetric step, are traction free on the free interface surfaces and particle continuity of velocity and stress at the material interface. These types of interface problems are traditionally solved using finite element or semi-analytical finite element techniques [27-29].

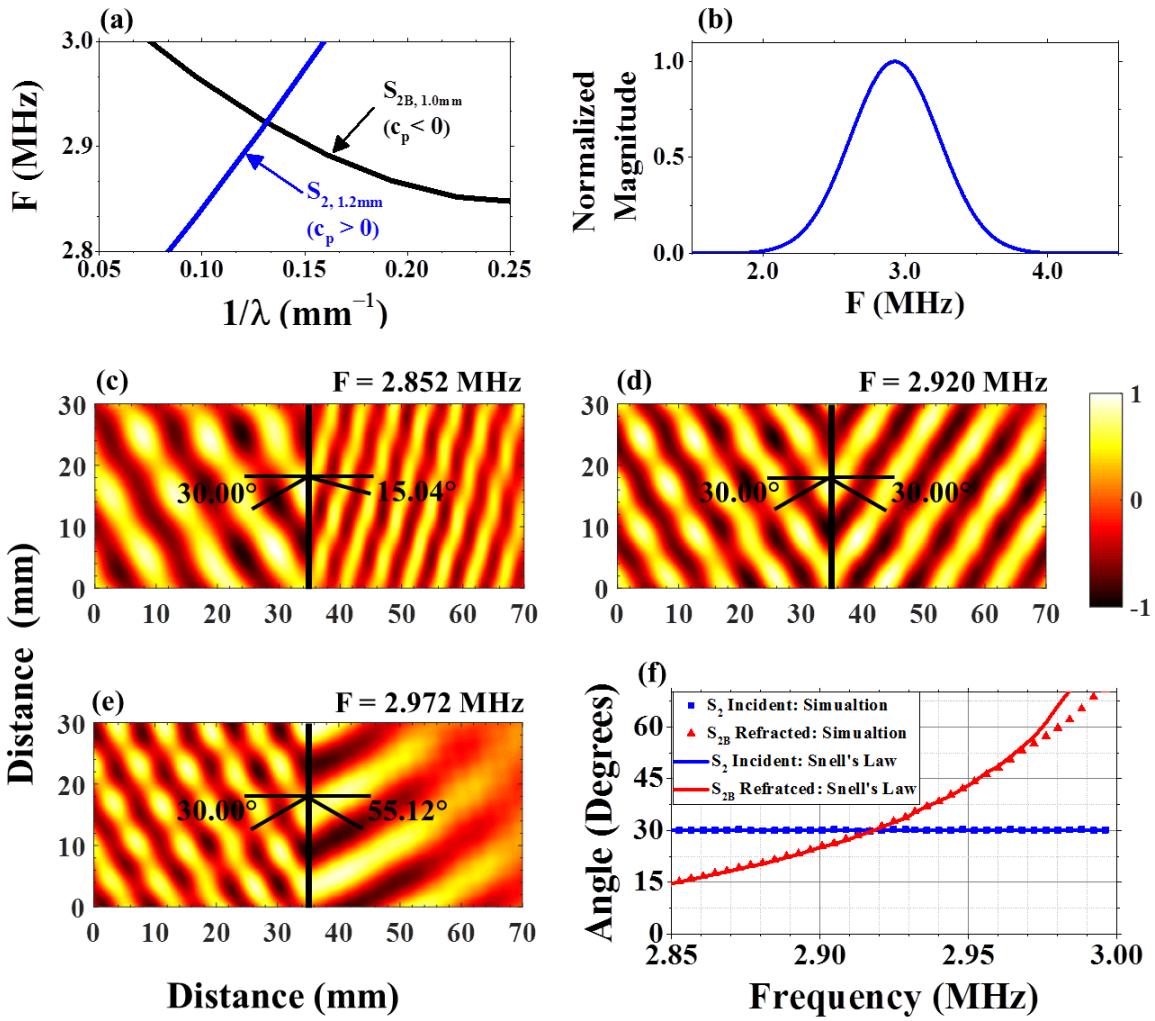

Fig. 2. (a) Portion of the dispersion curves for a 1.2 mm and 1.0 mm thick aluminum plate. For an excitation frequency near 2.92 MHz the modes are seen to cross at a wavenumber of 0.131 mm^{-1}. (b) The frequency spectrum of the excitation source. The center frequency is the crossing point of the S_2 and S_{2B} modes. The out-of-plane surface displacement at 2.853, 2.920, and 2.972 MHz are shown in (c), (b), and (e), respectively. (f) The angle of refraction as a function of frequency based on the simulation results (red triangles) and Snell's law (red line).

Even the much simpler case of a Lamb wave reflected from a free edge, where the only boundary condition is traction free on the free surface, is generally solved using numerical methods, with the exception of normal incident cases [30-32].

This paper uses finite element time domain commercial software (PZFlex, Weidlinger associates, Mountain View, CA) to explore the behavior of forward and backward Lamb wave mode conversion in simple plate structures. Aspects of negative refraction are examined including Lamb wave steering and quantifying the ideal focusing resolution of an acoustic lens. The mode conversion efficiency between forward and backward Lamb waves as a function of temporal frequency, angle of incidence, and interface geometry is also explored. Finally, a demonstration of partial source annihilation using backward propagating Lamb waves is demonstrated.

II. Negative refraction of a plane wave as a function of frequency.

Negative refraction of a plane wave is studied using a broadband frequency excitation on a plate that consists of two thicknesses. At each excitation frequency, an S_2 mode is excited and mode converted to an S_{2B} mode at the thickness change. The angle of refraction is calculated and explored as a function of the excitation frequency.

An aluminum plate 152 mm in length *(x-axis)* and 83.6 mm in width *(y-axis)* is considered. The plate is 1.2 mm thick *(z-axis)* on the left half and 1.0 mm thick on the right half. At the middle of the plate is a symmetric 0.1 mm step on the top and bottom. The plate is considered homogenous and isotropic with c_L and c_T equal to 6.31 mm/μs and 3.11 mm/μs, respectively. A line source is excited at 30° to the interface normal and is applied as a surface normal pressure. The source magnitude is spatially scaled by a 4.5 mm full width half max (FWHM) Gaussian curve. The size and geometry of the source is chosen to suppress excitation of higher wavenumber modes. Temporally, the source is a Gaussian enveloped 3.5 μs pulse train

with a broadband frequency response centered at 2.922 MHz and a FWHM of 0.73 MHz, the frequency spectrum of the source is shown in Fig. 2 (b). This source is chosen in order to excite modes in the vicinity of the crossing point shown in Fig. 2 (a).

An FEM is used to model the plate using an orthogonal grid with element dimensions: *69x69x50 μm^3 (x,y,z).* The top, bottom, and free interface surfaces are traction free and the remaining exterior surfaces are energy absorbing. During the simulation the out-of-plane surface displacement of every grid point, on the top of the plate, is sampled at 39.4 MHz. The total simulation time is 100 μs. The frequency response at each point is calculated every 4.0 kHz via FFT. The out-of-plane surface displacement at 2.853, 2.920, and 2.972 MHz is shown in Fig. 2 (c) through (e). These images are processed with a 2^{nd} order Butterworth low pass filter, cutoff wavenumber 0.233 mm^{-1}. It is evident that an S_2 mode is generated on the left side of the plate and then mode converts to an S_{2B} mode on the right side of the plate, by inspection of the wavenumbers and comparison to the dispersion curves. It is also clear that the S_{2B} mode undergoes negative refraction at the interface. As the excitation frequency becomes smaller than the crossing point frequency, the magnitude of the S_{2B} wavenumber becomes larger than the magnitude of the S_2 wavenumber and the refraction angle tends to the interface normal, as depicted in Fig. 2 (c). As the excitation frequency becomes larger than the crossing point frequency, the magnitude of the S_{2B} wavenumber becomes smaller than the magnitude of the S_2 wavenumber and the refraction angle tends to the interface parallel, as depicted in Fig. 2 (e). For the case where the excitation frequency is equal to crossing point frequency, the magnitude of the S_{2B} wavenumber is equal to the magnitude of the S_2 wavenumber and the angle of refraction will be equal, but opposite in sign, to the incident angle, as shown in Fig. 2 (d).

The angle of refraction is determined by examining the displacement field in Fourier space. The angle is found by plotting the magnitude of the 2D spatial FFT on a wavenumber versus wavenumber axes *(k_x-k_y)*. The angle of a vector from the origin to the peak response gives the angle of refraction. The angle of negative refraction as a function of excitation frequency is shown in Fig. 2 (f). These results are shown together with the theoretical results found by using Snell's law: $\sin(\theta_I)/c_{pI} = \sin(\theta_R)/c_{pR}$, where θ_I, θ_R, c_{pI}, and c_{pR} are the angle of incidence, angle of refraction, incident phase velocity, and refracted phase velocity, respectively. The angles of negative refraction calculated in the simulation are in good agreement with those predicted by Snell's law. The results in Fig. 2 (f) show that by modulating the excitation frequency the angle of negative refraction can be steered toward and away from the interface normal. These results show how to control the direction of energy flow, past the surface normal, using backward propagating Lamb waves.

III. Mode conversion efficiency as a function of incident angle.

Mode conversion between an S_2 mode and an S_{2B} mode, at the crossing point, is examined as a function of incident angle. Two approaches are taken, one where plane waves are generated at different discrete incident angles and another in which a point source is used to examine a continuous range of incident angles. The mode conversion efficiency is quantified by comparing the FFT magnitude of the refracted field and the incident field. These studies are conducted via FEM of an aluminum plate which is 1.2 mm thick on one side and 1.0 mm thick on the other side. The interface between the two thicknesses is a 0.1 mm symmetric step. The excitation sources are continuous wave (CW) 2.917 MHz sinusoidal surface normal pressures that are

spatially scaled by 4.5 mm FWHM Gaussian curves. The excitation frequency is determined by generating simulation based dispersions curves for a 1.2 mm thick plate and for a 1.0 mm thick plate and then finding the aforementioned crossing point. The simulation based crossing point is within 0.2% of the analytical based crossing point. The error is due to the numerical approximation of the grid size. The out-of-plane surface displacement of every grid point on the top of the plate is sampled at 39.4 MHz.

The out-of-plane surface displacement field at 100 μs, for a line source incident at 45°, is shown in Fig. 3 (a). This image is processed with a 2^{nd} order Butterworth low pass filter, cutoff wavenumber 0.233 mm^{-1}. Examining the wavenumber of the incident and refracted wave fields in Fig. 3 (a), it is clear that the source generates an S_2 mode which then mode converts to an S_{2B} mode at the interface, and that the S_{2B} mode undergoes negative refraction. The incident and refracted angles are equal but opposite in sign because the source is exited at the crossing point. Some of the incident S_2 mode is reflected at the interface as evident by the interference pattern adjacent to the interface. Equal sized portions of the incident and refracted wave fields are examined in Fourier space. The mode conversion efficiency is then calculated by comparing the maximum value of the 2D spatial FFT magnitude for the S_{2B} mode and the S_2 mode. This ratio is shown in Fig. 3 (d) for discrete incident angles of 0, 15°, 30°, 45°, and 60°, by the red squares. This ratio is greater than unity in some cases because the refracted wave field occurs in a thinner plate.

The out-of-plane surface displacement at 100 μs for a point source is shown in Fig. 3 (b). This image is processed with a 2^{nd} order Butterworth low pass filter, cutoff wavenumber 0.233 mm^{-1}. Similar to the previous case, the source generates an S_2 mode which converts to an S_{2B} mode at the interface and undergoes negative refraction. Large angle negative refraction is

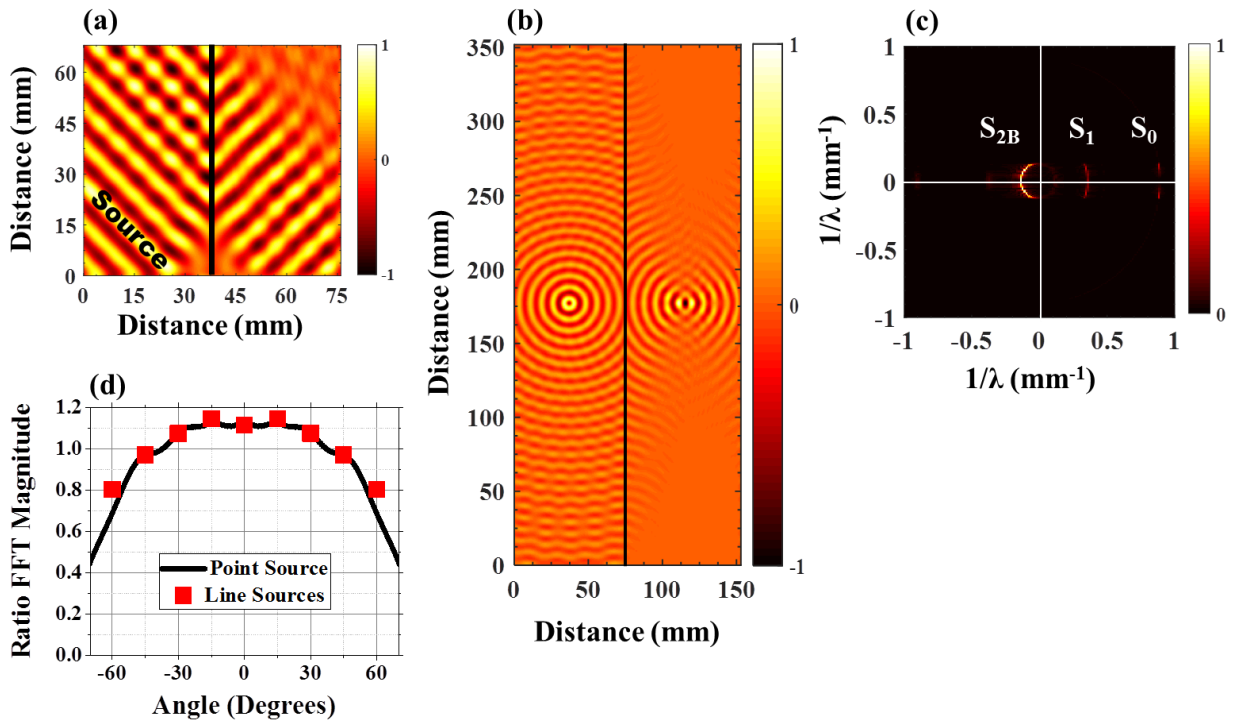

Fig. 3. (a) The out-of-plane surface displacement of a plane wave, incident at 45°, on a plate with a symmetric thickness step. (b) The out-of-plane surface displacement of a point source on a plate with a symmetric thickness step. In both (a) and (b) the left side of the plate supports a forward propagating Lamb wave (S_2 mode) and the right side of the plate supports a backward propagating Lamb wave (S_{2B} mode), at the excitation frequency. (c) Fourier domain representation of the wave field on the left side of the plate is shown in (b). The refracted modes are labeled and consist of the backward propagating S_{2B} mode and the forward propagating S_1 and S_0 modes. (g) The ratio of the FFT magnitude between the refracted S_{2B} mode and the incident S_2 mode as a function of angle of incidence.

observed in Fig. 3 (b). For any incident angle, the refracted angle is always equal but opposite in sign. Because of this, a focus is observed in the refracted field. The refracted field is examined in Fourier space. The magnitude of the 2D spatial FFT is shown in Fig. 3 (c). The refracted modes are labeled in this image by comparison with the dispersion curve. The S_{2B} mode appears on the -k_x side of the spectrum and occurs at angles up to about 70°, which was the maximum incident angle of the FEM geometry. Mode conversion to the S_{2B} mode occurred at all tested angles. The

S_1 mode and the S_0 mode both appear on the $+k_x$ side of the spectrum. Mode conversion to the S_1 mode occurs up to about 21° and mode conversion to the S_0 mode occurs up to about 8.5°. The largest possible angle of refraction is given by: $\theta_R = \sin^{-1}(k_I/k_R)$, and occurs for an incident angle of 90°. Using this relation, the maximum angles of refraction for the S_1 mode and the S_0 mode are calculated to be 21.4° and 8.9°, respectively, which is in good agreement with the simulation results. The ratio of the refracted field's 2D spatial FFT magnitude to the incident field's 2D spatial FFT magnitude is computed. This ratio is used to measure the mode conversion efficiency between the S_2 mode and the S_{2B} mode and is shown in Fig. 3 (d). The results of the point source and the line sources are in agreement. The results show that the mode conversion is fairly uniform for angles up to around 45°. Above 45° the mode conversion efficiency begins to degrade. The relative invariance in mode conversion with incident angle should allow for the creation an acoustic lens with good focusing resolution.

IV. Focusing resolution of an acoustic lens.

A flat acoustic lens is created using an aluminum plate that is 1.2 mm thick and has a 30.5 mm long symmetric trough in the middle. The trough is 1.0 mm thick and is referred to as the lens. This acoustic lens is geometrically similar to the one experimentally demonstrated in the literature [22-24]. The plate is 319.4 mm in length by 121.7 mm in width. A surface normal pressure is applied 15.21 mm to the left of the trough. The excitation source is a CW 2.917 MHz sinusoidal surface normal pressure that is spatially scaled by 4.5 mm FWHM Gaussian curve. The plate is analyzed with an FEM having the aforementioned properties. On a portion of the plate, the out-of-plane surface displacement of every grid point is sampled at 52.6 MHz. The out-

of-plane surface displacement at 90 μs is shown in Fig. 4 (a). The displacement magnitude is shown in Fig. 4 (b). These images are not filtered. In both the displacement and magnitude plots the field is observed to focus near the center of the lens and again in the plate past the lens. The focus in the lens is due to negative refraction from the S_2 mode to the S_{2B} mode. The second focus is due to negative refraction from the S_{2B} mode to the S_2 mode. The magnitude of the focus past the lens is smaller than the source magnitude due to energy lost in reflections at each interface, lost to mode conversion into non-focusing modes, and in non-propagating modes generated by the source. The magnitude of the focus in the lens is subject to similar losses; however, because the lens is thinner a direct magnitude comparison to the source is not insightful. The resolution of each focus is quantified by examining the lateral field distribution through the focal point. The displacement at 2.917 MHz is evaluated using an FFT over 90.0 μs to 95.1 μs *(15 cycles)*. The squared displacement along the entire width of the plate is computed at a length of x = 47.02 mm and is shown in Fig. 4 (c) by the red circles. The same calculation is made at a length of x = 74.12 mm and is shown in Fig. 4 (d) by the red circles. Each focus resolution is compared to the standard diffraction theory given by [24]:

$$I \propto \left(\frac{\sin(ka\sin(\theta))}{ka\sin(\theta)}\right)^2 \qquad (2)$$

where k is the wavenumber, a is the lateral distance from the focal point, and sin(θ) is the numerical aperture. For a numerical aperture of unity, diffraction limited, the FWHM resolution is 3.39 mm. The FWHM resolution of the focus within the lens is 3.52 mm and in the plate past the lens is 3.79 mm. The Lamb wave acoustic lens is observed to have nearly diffraction limited focusing resolution. This occurs because the mode conversion is fairly uniform over a large numerical aperture and there are no defects present. It does not appear possible to achieve

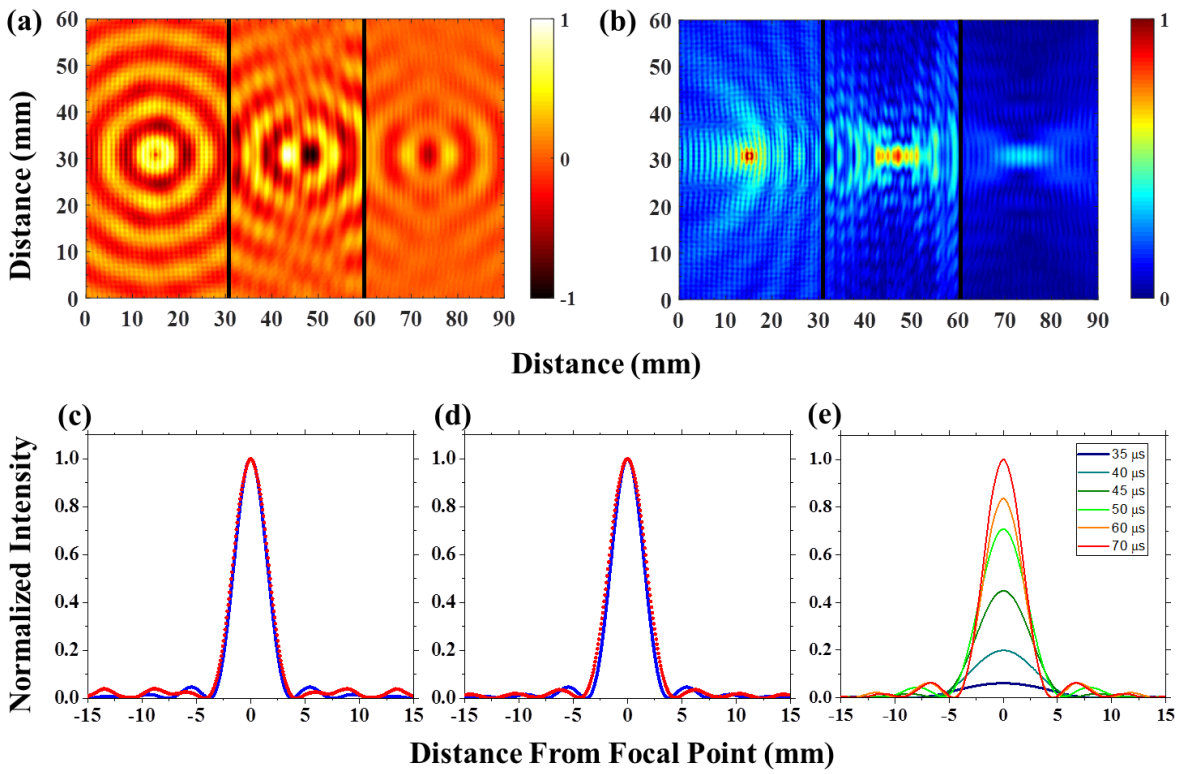

Fig. 4. (a) The out-of-plane surface displacement of a point source on a plate with a symmetric thickness trough (lens) in the center. (b) The out-of-plane surface displacement magnitude. At the excitation frequency, the left side of the plate supports a forward propagating Lamb wave (S_2 mode), the middle of the plate supports a backward propagating Lamb wave (S_{2B} mode), and the right side of the plate supports a forward propagating Lamb wave (S_2 mode). The result of this geometry is that the Lamb wave field focuses in the lens and again past the lens. The lateral intensity distribution is shown for the focus in the lens (x = 47.02 mm) and for the distal focus (x = 74.12 mm) in (c) and (d), respectively. (e) The temporal evolution of the distal focus is shown by comparing the lateral intensity distribution through the focus at times prior to steady state.

subwavelength focusing with the acoustic lens as currently constructed. This would require mode conversion to backward propagating or backward evanescent modes with shorter wavelengths, which would necessarily result in a mismatched phase velocity to the incident wave and therefore a negative refraction angle not equal in magnitude to the incident angle. This non-matched negative refraction angle would focus with aberration.

The temporal evolution of the focus after the lens is studied by examining the focus resolution at various times prior to steady state, as shown in Fig. 4 (e). The resolution is observed to temporally evolve, becoming better over time. This illustrates that the focus occurs because the individual rays propagate away from the source, undergo negative refraction at the interface, and then coalesce at the same point in space and arrive in phase. The rays at higher angles travel further and thus take longer to reach the focal point. The focus evolution occurs over a relatively long time. This focusing time could be made even longer by utilizing a system with a crossing point closer to the zero group velocity point.

V. Negative refraction between modes other than an S_2 mode and an S_{2B} mode.

Previous results in this paper examined mode conversion between a forward propagating S_2 mode and backward propagating S_{2B} mode; however, mode conversion between other forward and backward propagating modes is possible and is demonstrated. A forward propagating anti-symmetric A_1 mode and the previously discussed backward propagating symmetric S_{2B} mode are considered. Fig. 5 (a) shows the dispersion curves for a 0.55 mm thick aluminum plate and a 1.00 mm thick aluminum plate. It is observed that at F = 2.917 MHz the A_1 and S_{2B} modes cross at a wavenumber equal to 0.129 mm^{-1}. An aluminum plate 0.55 mm thick on one side and 1.0 mm thick on the other side is examined. The transition between these two thicknesses is an asymmetric 0.45 mm step. The choice to use an asymmetric step was made by examination of the A_1 and S_{2B} normal and in-plane displacement mode shapes. Comparing the mode shapes indicated that the interface continuity boundary condition, between these two modes, would more readily be satisfied by an asymmetric step than by a symmetric step. The A_1 mode is

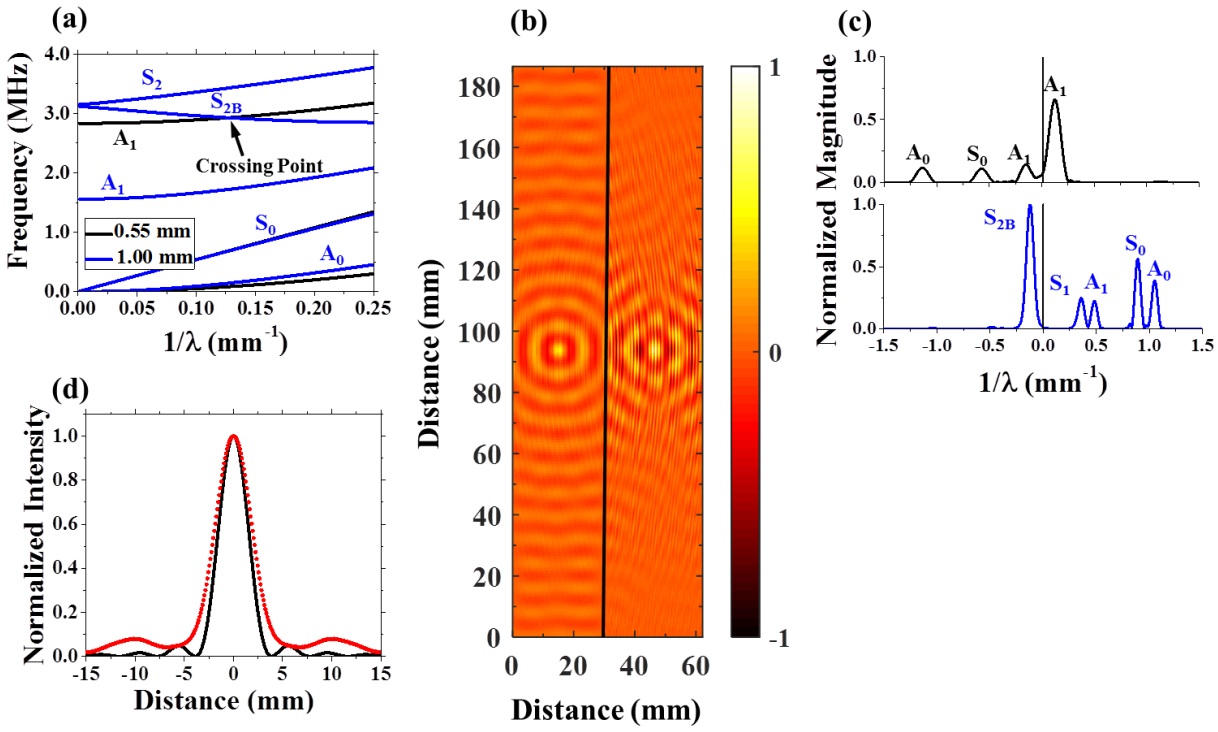

Fig. 5. (a) Dispersion curves for aluminum plates of 0.55 mm and 1.0 mm thicknesses. (b) The out-of-plane surface displacement of a point source on a plate with an asymmetric thickness step. At the excitation frequency, the left side of the plate supports a forward propagating Lamb wave (A_1 mode) and the right side of the plate supports a backward propagating Lamb wave (S_{2B} mode). (c) The spatial frequency spectrum of the incident, reflected, and transmitted waves along a line at y = 93.26 mm (through the center of the source). (d) The normalized lateral intensity distribution at x = 48.31 mm.

excited in the center of the 0.55 mm thick side of the plate using a CW 2.917 MHz sinusoidal surface normal pressure scaled by a FWHM 5.49 mm Gaussian curve. The system is analyzed with an FEM consisting of an orthogonal grid space of *50x50x50 μm^3 (x,y,z)*. Fig. 5 (b) shows the out-of-plane surface displacement at 127 μs. Examining the refracted field it is seen that the S_{2B} mode, among other modes, is converted to at the interface. The incident, reflected, and transmitted spatial frequency spectra at y = 93.25 mm are shown in Fig. 5 (c). The incident spectrum shows that the excitation source effectively generates the A_1 mode on the 0.55 mm

thick side of the plate. The reflected spectrum shows that, at normal incidence, the A_1, S_0, and A_0 modes are reflected from the interface. The transmitted spectrum shows that, at normal incidence, the S_{2B}, S_1, A_1, S_0, and A_0 modes are transmitted. The S_{2B} mode undergoes negative refraction as evident by the focus in the refracted field and by the negative wavenumber in the frequency spectrum. The focusing resolution of the refracted wave field is evaluated using the previously detailed lateral distribution methodology and the results are shown in Fig. 5 (d). The FWHM resolution of the focus is 4.28 mm. The FWHM of the diffraction limit is 3.44 mm. The quality of the resolution gives an indication that the mode conversion is fairly uniform as a function of angle of incidence. The focus resolution in this case is not as good as it is in the S_2 mode to the S_{2B} mode case *(or vice versa).*

Another case that is investigated is where a forward propagating A_2 mode is crossed with a backward propagating A_{2B} mode. This is accomplished using a fused silica plate that is 2.3 mm thick on one side and 2.0 mm thick on the other side, with a 0.15 mm symmetric step. Poisson's ratio (ν) for fused silica is 0.17, which is necessary to get backward wave motion in the A_2 mode [0]. The results are not presented here, but good mode conversion was achieved and an FWHM focusing resolution of 4.94 mm was observed as compared to the diffraction limit of 4.16 mm.

These results demonstrate that mode conversion between forward propagating modes and backward propagating modes can occur between modes of different families and can occur with good efficiency. Also, negative refraction by crossing two anti-symmetric modes was observed and again occurred with good efficiency. The modes that are reflected and transmitted at the interface are determined by satisfying the interface boundary conditions. If a backward mode is necessary to satisfy these conditions, then it will be transmitted or reflected accordingly.

VI. Mode conversion efficiency for varied interface conditions.

The transmission efficiency of an S_2 mode through a negative index lens is investigated. Two approaches are taken; one where the material properties of the lens are varied and the other where the lens interface geometry is varied.

The first case considered is where the material properties of the lens are changed. The shape of a plate's dispersion curve depends on the plate's material properties. Changing the material stiffness (E) and/or ν shifts the curve up and down and stretches and compresses it. Fig. 6 (a) shows an aluminum plate with a constant thickness and an insert with different material properties. At F = 2.917 MHz and k = 0.131 mm^{-1}, this aluminum plate supports an S_2 mode and the insert supports an S_{2B} mode, for a set of (E,ν) pairs. The insert will act as a lens. Transmission efficiency of the S_2 mode through this lens, at normal incidence, is studied for a range of (E,ν) pairs. One hundred and fifty four 2D plane strain FEM simulations are performed. Each simulation examines a value of ν between 0.136 – 0.373 for the lens material. Each simulation represents the plate on an orthogonal grid with element dimensions *50x50 μm^2 (x,z).* The out-of-plane surface displacement is sampled on the top of the plate 46 mm prior to the lens, the 46 mm lens, and 46 mm after the lens. For each case the spatial frequency spectrum is computed by FFT. The transmission ratio is calculated as the FFT magnitude of the S_2 mode after and before the lens. The transmission ratio as a function of ν is shown in Fig. 7 (b). The maximum transmission ratio is 92% and occurs when the lens material properties are ν = 0.279 and E = 113 GPa. For this case the spatial frequency spectrum of the incident, reflected, and transmitted waves are shown in Fig. 6 (c). The incident spectrum shows that the S_2 mode and the S_0 mode are generated by the source excitation. Nearly an equal magnitude S_0 mode is reflected at the interface and a small S_2 mode is reflected at the interface. After passing through the lens,

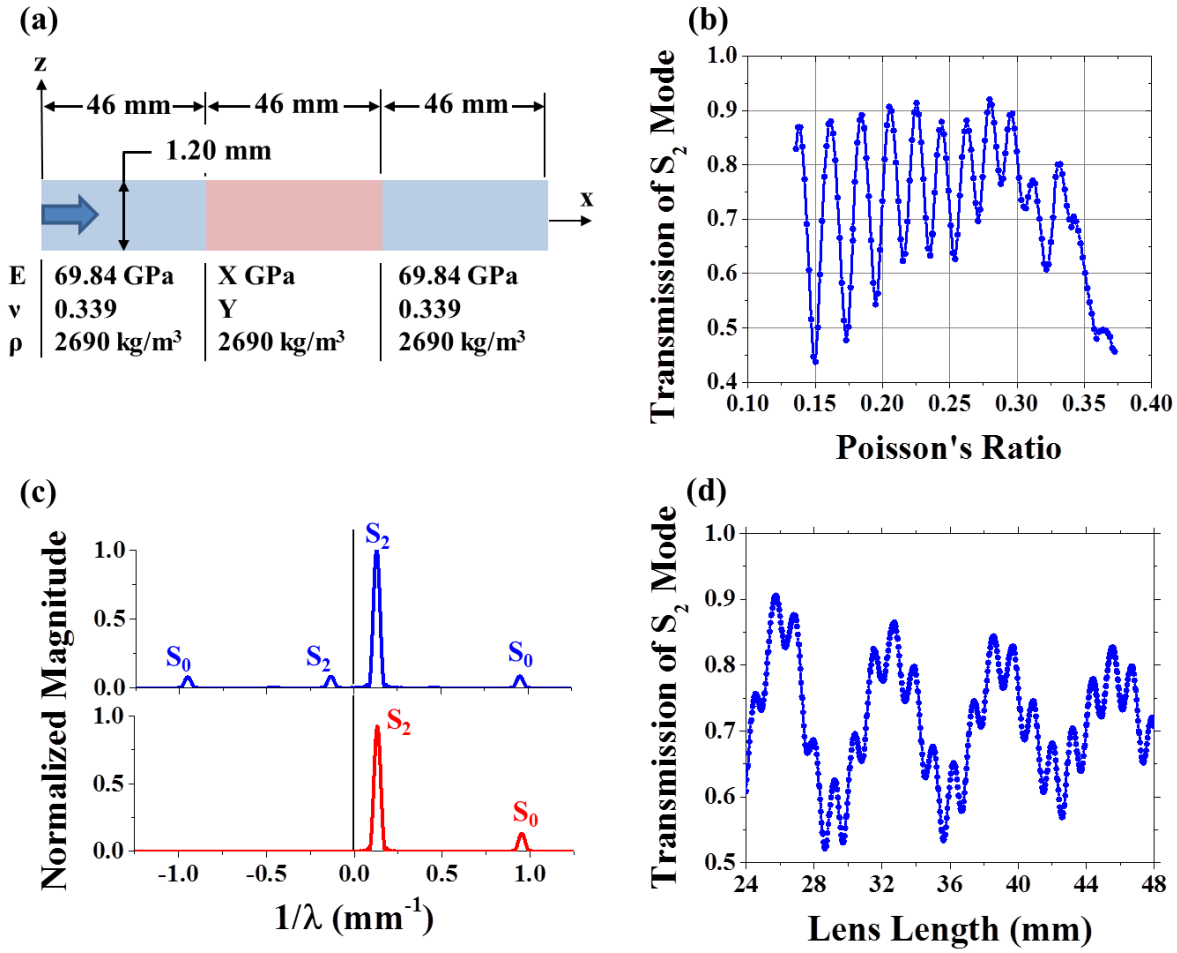

Fig. 6. (a) Cross section of an aluminum plate with a material insert in the center. At the excitation frequency, the left side of the plate supports a forward propagating Lamb wave (S_2 mode), the material insert (lens) supports a backward propagating Lamb wave (S_{2B} mode), and the right side of the plate supports a forward propagating Lamb wave (S_2 mode). (b) The transmission efficiency of the S_2 mode as a function of the material inserts' Poisson's ratio. (c) The spatial frequency spectrum of the incident, reflected, and transmitted Lamb waves when the material insert properties are: $\nu = 0.279$, $E = 113$ GPa, and $\rho = 2690$ kg/m^3. (d) Transmission of the S_2 mode versus material insert length when the material insert's properties are: $\nu = 0.339$, $E = 102$ GPa, and $\rho = 2690$ kg/m^3.

the resulting spectrum consists of the S_2 mode and the S_0 mode. The magnitude of the S_2 mode is smaller than that of source and the magnitude of the S_0 mode is slightly greater than that of the source. The S_2 mode transmission through the lens results in some mode conversion to the

S_0 mode. The transmission of the S_2 mode appears to oscillate with respect to ν. However, studying a fixed ν case and varying the length of the lens results in an oscillatory response as well, as shown in Fig. 6 (d). The spatial frequencies of this oscillation are close to the wavenumbers of the S_0 mode and the S_{2B} mode in the lens material. This suggests that the oscillatory dependence is caused by the relative phase of the modes within the lens. Additionally there may be a resonant effect occurring in the lens, as evident by the decaying envelope of the oscillations with increasing lens length. These results show that the previous oscillations with respect to ν should be viewed as an envelope of possible transmission values, where maxima and minima may be obtained by changing the lens length.

Next the case is considered where the material of the plate remains constant but the geometry of the interface is changed from a step to a linear slope. An aluminum plate with a symmetric linear sloped thickness change is depicted in Fig. 7 (a). The grade of this slope is varied between 90° and 3.8°. Additionally, the total length of the lens is varied between 45 mm and 47 mm in 0.5 mm increments. A 2D plain strain FEM is used to simulate each case. The transmission ratio of the S_2 mode through the sloped interface lenses is shown in Fig. 7 (b). The peak transmission is 93% and occurs when the interface slope is 3.8° and the lens length is 46.5 mm. The spatial frequency spectrum of the incident, reflected, and transmitted waves are shown for this case in Fig. 7 (c). The spectra show that the sloped interface reduces the mode conversion of the S_2 mode to the S_0 mode through the lens, as evident by the relatively small magnitude of the transmitted S_0 mode. In general the transmission improves with a more gradual transition between the two plate thicknesses. The transmission is also affected by the length of the lens as shown in Fig. 7 (b). This affect appears to diminish has the interface slope becomes smoother. These results show that a smooth linear transition between plate thicknesses will result

in mode conversion from an S_2 mode to an S_{2B} *(and vice versa)* with less mode conversion to other modes.

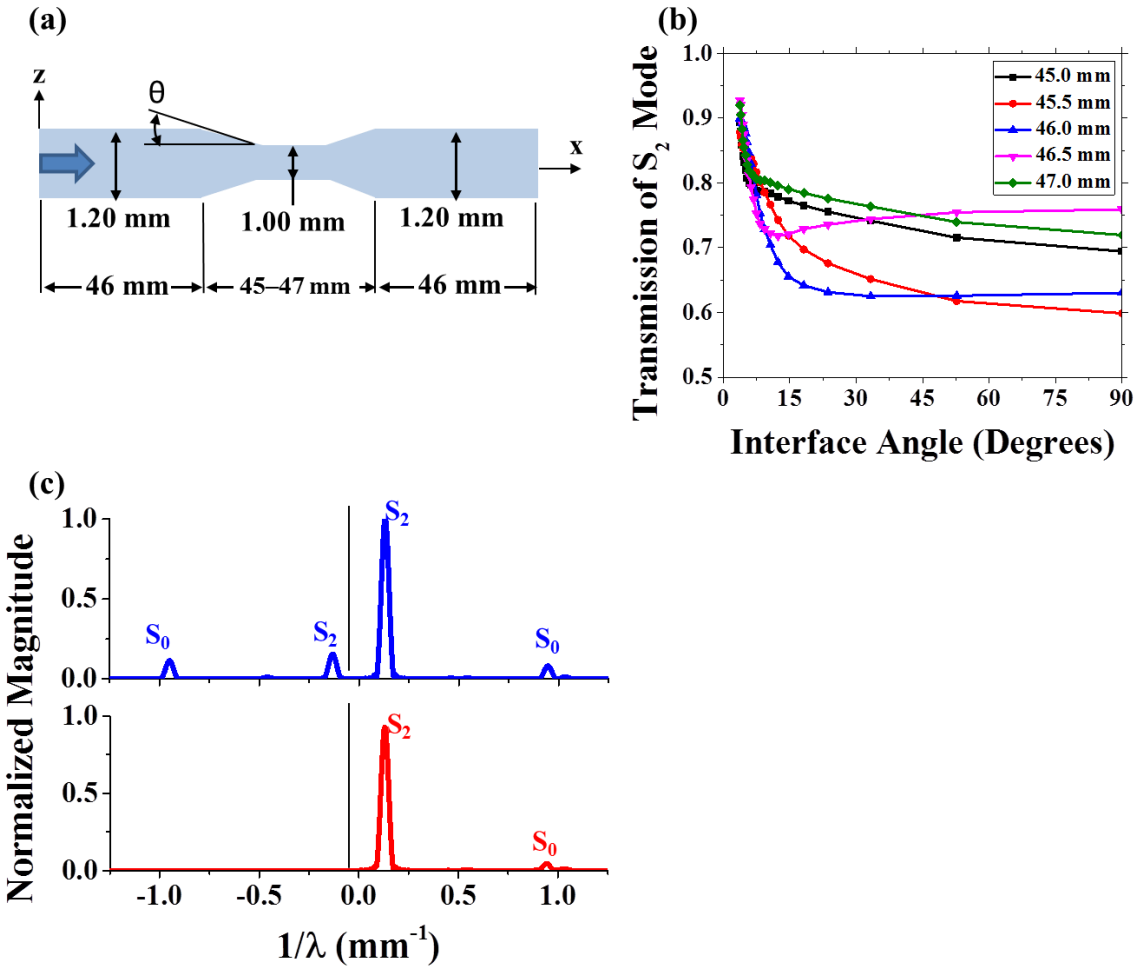

Fig. 7. (a) Cross section of an aluminum plate with symmetric linear transitions between two thicknesses. At the excitation frequency, the left side of the plate supports a forward propagating Lamb wave (S_2 mode), the middle of the plate (lens) supports a backward propagating Lamb wave (S_{2B} mode), and the right side of the plate supports a forward propagating Lamb wave (S_2 mode). (b) The transmission efficiency of an S_2 mode versus interface angle for several lens lengths. (c) The spatial frequency spectrum of the incident, reflected, and transmitted Lamb waves when the lens length is 46.5 mm and interface angle is 3.8°.

VII. Partial source annihilation using forward and backward propagating waves.

A method of partially annihilating the displacement field of a point source using an adjacent anti-source is presented [33]. This is illustrated using an aluminum plate measuring 122.4 mm in length by 122.4 mm in width. Half of the plate is 1.2 mm thick and the other half is 1.0 mm thick; there is a 0.1 mm symmetric step along the middle of the plate. Two excitation sources are used; both are CW 2.917 MHz sinusoidal surface normal pressures spatially scaled by 4.5 mm FWHM Gaussian curves. The source to be partially annihilated is located 7.65 mm to the left of the interface. The anti-source is located 7.65 mm to the right of the interface and is excited 180° out of phase, relative to the other source. The system is analyzed with an FEM using an orthogonal grid with element dimensions *69x69x50 μm3 (x,y,z).* Fig. 8 (a) shows the out-of-plane surface displacement field at 1 μs. This is prior to any interaction between the source and anti-source. The source consists mostly of a forward propagating S_2 mode and the anti-source consists mostly of a backward propagating S_{2B} mode. The sources are observed to be 180° out of phase. Fig. 8 (b) and (c) show the displacement field at 10.0 μs and 20.0 μs, respectively. These two images show the transient interaction between the source and anti-source displacement wave fields. Destructive interference occurs for regions not in-between the source and anti-source. In-between the sources the waves are traveling in opposite directions and a standing wave results. Fig. 8 (d) shows the displacement field near steady state, at 50 μs. In this image nearly half of the source's displacement field is cancelled by the anti-source. Nearly half of the anti-source's displacement field has a reduced magnitude. This occurs because the mode conversion efficiency is not the same between the S_2 mode and S_{2B} mode as it is between the S_{2B} mode and S_2 mode. There may be an interface condition in which these two are equal, and in such a case the entire wave field not in-between sources would be cancelled. The displacement images in Fig. 8 (a)

through (d) are each processed with a 2nd order Butterworth low pass filter, cutoff wavenumber 0.233 mm^{-1}. These results show that it is possible to partially annihilate a portion of a point source using an anti-source by application of negative refraction between forward and backward propagating Lamb waves. This simulation also demonstrates that a backward propagating S_{2B} mode can be effectively generated by application of a surface normal pressure of appropriate spot size.

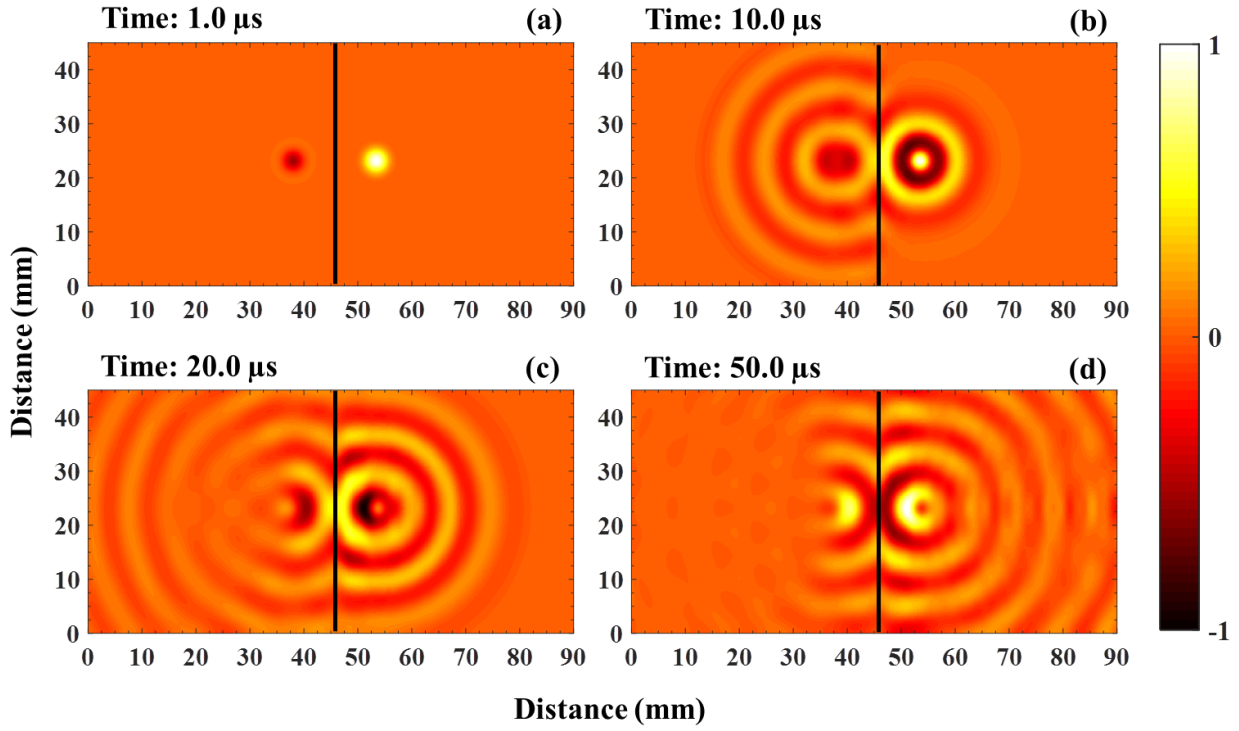

Fig. 8. The out-of-plane surface displacement at: 1.0, 10.0, 20.0, and 50.0 µs for two point sources on a plate with a symmetric thickness step. At the excitation frequency, the left side of the plate supports a forward propagating Lamb wave (S_2 mode) and the right side of the plate supports a backward propagating Lamb wave (S_{2B} mode). The sources are 180° out of phase. At steady state (d), the source on the right side of the plate is observed to partially cancel a portion of the source on the left side of the plate.

VIII. Conclusions.

Wave fields can be controlled in novel ways using systems that support both forward propagating and backward propagating waves. One way these systems are unique is that forward and backward waves undergo negative refraction when they convert from one to the other. A simple homogenous elastic plate, with one or more thickness changes, is a system that supports both forward and backward propagating waves at the same excitation frequency. Therefore, a simple plate can be used to investigate the behavior and applications of backward propagating waves and negative index materials. Here it is shown that an aluminum plate with a symmetric thickness step can be used to steer a plane wave at a range of angles, greater than surface normal, by modulating the excitation frequency. It is also shown that the mode conversion between forward propagating Lamb waves (S_2 mode) and backward propagating Lamb waves (S_{2B} mode) is fairly uniform with angle of incidence. Consequently, a flat acoustic lens created using an aluminum plate with a symmetric trough (lens) is shown to focus the wave field within the lens and after the lens and the focal resolution is nearly perfectly diffraction limited. It is further shown that mode conversion and negative refraction can occur between antisymmetric (A_1) and symmetric (S_{2B}) modes and between only antisymmetric modes (A_2-A_{2B}). Next, the total transmission of a forward propagating Lamb wave (S_2 mode) through a lens (S_{2B} mode) is explored for various interface conditions. It is determined that a linear sloped interface reduced the mode conversion to other modes and 93% transmission of the S_2 mode was achieved, at normal incidence. Finally, the ability to partially annihilate nearly half of a point source's wave field (S_2 mode) is demonstrated by application of a backward Lamb wave (S_{2B} mode) anti-source.

Acknowledgement

D. M. Stobbe and T. W. Murray gratefully acknowledge the support of this research by the National Foundation under Grant CMMI 1335426.

References

1. R. A. Shelby, D. R. Smith, and S. Schultz, “Experimental Verification of a Negative Index of Refraction”, Science 292, 77 (2001).

2. A. A. Houck, J. B. Brock, and I. L. Chuang, “Experimental Observation of a Left-Handed Material That Obeys Snell’s Law”, Phys. Rev. Lett. 90, 137401 (2003).

3. N. Fang, D. Xi, J. Xu, M. Ambati, W. Srituravanich, C. Sun, and X. Zhang, “Ultrasonic metamaterials with negative modulus”, Nature Materials 5, 452-456 (2006).

4. S. Zhang, L. Yin, and N. Fang, “Focusing Ultrasound with an Acoustic Metamaterial Network”, Phys. Rev. Lett. 102, 194301 (2009).

5. A. Sukhovich, B. Merheb, K. Muralidharan, J. O. Vasseur, Y. Pennec, P. A. Deymier, and J. H.Page, "Experimental and theoretical evidence for subwavelength imaging in phononic crystals." Phys. Rev. Lett. 102, 154301 (2009).

6. M. Notomi, “Theory of light propagation in strongly modulated photonic crystals: Refractionlike behavior in the vicinity of the photonic band gap”, Phys. Rev. B 62, 10696 (2000).

7. E. Cubukcu, K. Aydin, E. Ozbay, S. Foteinopoulou, and C. M. Soukoulis, “Electromagnetic waves: Negative refraction by photonic crystals”, Nature (London) 423, 604 (2003).

8. I. Tolstoy, and E. Usdin, “Wave Propagation in Elastic Plates: Low and High Mode Dispersion”, J. Acoust. So. Am. 29, 1 (1957).

9. A. H. Meitzler, “Backward-Wave Transmission of Stress Pulses in Elastic Cylinders and Plates”, J. Acoust. So. Am. 38, 835 (1965).

10. P. L. Marston, “Negative group velocity Lamb waves on plates and applications to the scattering of sound by shells”, J. Acoust. Soc. Am. 38, 835 (1965).

11. M. Ibanescu, S. G. Johnson, D. Roundy, C. Luo, Y. Fink, and J. D. Joannopoulos, “Anomalous Dispersion Relations by Symmetry Breaking in Axially Uniform Waveguides”, Phy. Rev. Lett. 92, 6 (2004).

12. A. L. Shuvalov, and O. Poncelet, “On the backward Lamb waves near thickness resonances in anisotropic”, Int. J. Solids Struct. 45, (2008).

13. A. A. Maznev and A. G. Every, “Surface acoustic waves with negative group velocity in a thin film structure on silicon”, Appl. Phys. Lett. 95, 011903 (2009).

14. V. G. Veselago, “The electrodynamics of substances with simultaneously negative values of ε and μ”, Soviet Physics Uspekhi, 10, 4 (1968).

15. J. B. Pendry, “Negative Refraction Makes a Perfect Lens”, Phys. Rev. Lett. 85, 3966 (2000).

16. S. A. Cummer, “Simulated causal subwavelength focusing by a negative refractive index slab”, Appl. Phys. Lett. 95, 011903 (2003).

17. E. Cubukco, K. Aydin, E. Ozbay, S. Foteinopoulou, and C. M. Soukoulos, “Electromagnetic waves: Negative refraction by photonic crystals”, Nature 423, (2003).

18. S. Yang, J. H. Page, Z. Liu, M. L. Cowan, C. T. Chan, and P. Sheng, “Focusing of Sound in a 3D Phononic Crystal”, Phys. Rev. Lett. 93, 024301 (2004).

19. N. Fang, H. Lee, C. Sun, and X. Zhang, “Sub–Diffraction-Limited Optical Imaging with a Silver Superlens”, Science 308, 534 (2005).

20. S. A. Ramakrishna, “Physics of negative refractive index materials,” Rep. Prog. Phys. 68, 449 (2005).

21. V. G. Veselago and E.E. Narimanov , “The left hand of brightness: past, present, and future of negative index materials”, Nature Material 5, (2006).

22. S. Bramhavar, C. Prada, A. A. Maznev, A. G. Every, T. B. Norris, and T. W. Murray, “Negative refraction and focusing of elastic lamb waves at an interface”, Phys. Rev. B 83, 014106 (2011).

23. R. Craster and S. Guenneau, “Acoustic metamaterials: Negative refraction, imaging, lensing and cloaking”, Springer-Verlag, London, (2012).

24. F. D. Philippe, T. W. Murray, and C. Prada, “Focusing on Plates: Controlling Guided Waves using Negative Refraction”, Sci. Rep. 5, 11112 (2015).

25. H. Lamb, “On Group Velocity”, Proc. Lond. Math. Soc. 1, 473 (1904).

26. J. D. Achenbach, Wave Propagation in Elastic Solids, North-Holland, Amsterdam, (1980).

27. I. Bartolia, A. Marzania, F. Lanza di Scaleaa, and E. Violab, “Modeling wave propagation in damped waveguides of arbitrary cross-section”, J. Sound Vib. 295, (2006).

28. M. V. Predoi, M. Castaings, B. Hosten, and C. Bacon, “Wave propagation along transversely periodic structures”, J. Acoust. Soc. Am. 121, 4 (2007).

29. M. Castaings and M. Lowe, “Finite element model for waves guided along solid systems of arbitrary section coupled to infinite solid media”, J. Acoust. Soc. Am. 123, 2 (2008).

30. P. J. Torvik, “Reflection of Wave Trains in Semi-Infinite Plates”, J. Acoust. Soc. Am. 41, 346 (1967).

31. R.D. Gregory and I. Gladwell, "The reflection of a symmetric Rayleigh-Lamb wave at the fixed or free edge of a plate." J. Elasticity 13(2), 185 (1983).

32. B. Morvan, N. Wilkie-Chancellier, H. Duflo, A. Tinel, and J. Duclos, “Lamb wave reflection at the free edge of a plate” J. Acoust. Soc. Am, 113(3), 1417 (2003).

33. Y. Lai, H. Zheng, Z. Q. Zhang, and C. T. Chan, “Manipulating sources using transformation optics with ‘folded geometry’”, J. Opt. 13, 2 (2010).

Appendix B: M-File for SAFE method of calculating dispersion curves and mode curves for an elastic plate.

```
%M-file for generating dispersion curves using SAFE method for an isotropic
%plate of constant thickness

close all
clear all

%Define plate properties

rho = 2690;     %density (kg/m^3)
H = 1.5e-03;    %total thickness in (m)
cT=3000;    %Shear wave speed (m/s)
cL=6000;    %Longitudinal wave speed (m/s)

% sig = 0.3349;     %Use Poisson's ratio and shear wave speed
% cL = sqrt(cT^2*(2*(1-sig))/(1-2*sig));      %longitudinal wave speed m/s

lam = rho*(cL^2-(2*cT^2));  %Lame constant 1
nu = rho*cT^2;      %Lame constant 2

% Calculate matrix stiffness values from Lame constants
C11 = lam+(2*nu);
C12 = lam;
C22 = lam+(2*nu);
C66 = nu;

%Defines the wavenumber range and increments for the solution (m^-1)
zeta = 0:100:5000;

%Define number of elements through thickness
num_elem = 200;

%Calculate element thickness (m)
h = H/num_elem;

%Number of DOF based on number of elements
N = (4*(num_elem-1))+6;

%Loop over the wavenumber space
mm=1;
for mm = 1:length(zeta);

    %Initial size of matrices
    Kg = zeros(N);
    Mg = zeros(N);
```

```
    for n=1:num_elem;
        %get element matrices
        [k,m] = quad_element(C11,C12,C22,C66,rho,h,zeta(mm));
        %put in matrix
        mid = 4*n-(1/2);
        Kg(mid-2.5:mid+2.5,mid-2.5:mid+2.5) = Kg(mid-2.5:mid+2.5,mid-
2.5:mid+2.5) + k ;
        Mg(mid-2.5:mid+2.5,mid-2.5:mid+2.5) = Mg(mid-2.5:mid+2.5,mid-
2.5:mid+2.5) + m ;
    end

    %solve eigen value problem
    v = eig(Kg,Mg);
    %eigen values are w^2 rads/s
    Omega(:,mm) = sqrt(abs(v));

end


%Plot dispersion curves in F (Hz) versus wavenumber (mm^-1)
figure(10);
plot(10^-3*zeta,10^-6*(1/(2*pi))*(Omega(:,:)),'k-','linewidth',2)
%Set axis range for display
axis([0 5 0 5])
xlabel('Wavenumber (mm^{-1})')
ylabel('Frequency (MHz)')




%M-file for generating mode shapes using SAFE method for an isotropic
%plate of constant thickness

close all
clear all

%Define plate properties

rho = 2690;     %density (kg/m^3)
H = 1.533e-03;    %total thickness in (m)
cT=3125;    %Shear wave speed (m/s)
cL=6272;    %Longitudinal wave speed (m/s)

% sig = 0.3349;     %Use Poisson's ratio and shear wave speed
% cL = sqrt(cT^2*(2*(1-sig))/(1-2*sig));      %longitudinal wave speed m/s

lam = rho*(cL^2-(2*cT^2));  %Lame constant 1
nu = rho*cT^2;      %Lame constant 2

% Calculate matrix stiffness values from Lame constants
C11 = lam+(2*nu);
C12 = lam;
C22 = lam+(2*nu);
C66 = nu;
```

```
%Defines the wavenumber of interest (m^-1)
zeta = 500;

%Define number of elements through thickness
num_elem = 200;

%Calculate element thickness (m)
h = H/num_elem;

%Number of DOF based on number of elements
N = (4*(num_elem-1))+6;

%Loop over the wavenumber space
mm=1;
for mm = 1:length(zeta);

    %Initial size of matrices
    Kg = zeros(N);
    Mg = zeros(N);

    for n=1:num_elem;
        %get element matrices
        [k,m] = quad_element(C11,C12,C22,C66,rho,h,zeta(mm));
        %put in matrix
        mid = 4*n-(1/2);
        Kg(mid-2.5:mid+2.5,mid-2.5:mid+2.5) = Kg(mid-2.5:mid+2.5,mid-
2.5:mid+2.5) + k ;
        Mg(mid-2.5:mid+2.5,mid-2.5:mid+2.5) = Mg(mid-2.5:mid+2.5,mid-
2.5:mid+2.5) + m ;
    end

    %solve eigen value problem, request eigen vectors in addition to eigen
    %values
    [d,v] = eig(Kg,Mg);
    Omega(:,mm) = sqrt(abs(diag(v)));

end


%Plot dispersion curves in F (Hz) versus wavenumber (mm^-1)
figure(1);
plot(10^-3*zeta,10^-6*(1/(2*pi))*(Omega(:,:)),'k-','linewidth',2)
%Set axis range for display
axis([0 5 0 5])
xlabel('Wavenumber (mm^{-1})')
ylabel('Frequency (MHz)')

%Select mode of interest 1 = A0, 2 = So, 3 = A1, ect.
ii = 3;

%Put x and y displacement in separate arrays
mode_x = d(1:2:end,ii);
mode_y = d(2:2:end,ii);
```

```
start = 1;
%Calculate displacements/strain/stress from element shape function definition
for kk = 1:num_elem
    x2b = (0:1/9:1);

    %Displacement
    ux = (mode_x(start).*(1-3.*x2b+2.*x2b.*x2b))+(mode_x(start+1).*(4.*x2b-
4.*x2b.*x2b))+(mode_x(start+2).*(2.*x2b.*x2b-x2b));
    uy = (mode_y(start).*(1-3.*x2b+2.*x2b.*x2b))+(mode_y(start+1).*(4.*x2b-
4.*x2b.*x2b))+(mode_y(start+2).*(2.*x2b.*x2b-x2b));

    %Strain
    ep11 = zeta*-1*ux;
    ep22 = (1/h).*( (-1*mode_y(start).*(-3+4*x2b)) + (-1*mode_y(start+1).*(4-
8*x2b)) + (-1*mode_y(start+2).*(4*x2b-1)) );

    ep12_a = (1/h).*( (-1*mode_x(start).*(-3+4*x2b)) + (-
1*mode_x(start+1).*(4-8*x2b)) + (-1*mode_x(start+2).*(4*x2b-1)) );
    ep21_a = zeta*1*uy;

    ep12 = 1/2*(ep12_a+ep21_a);

    %Stress
    sig11 = ( (lam+2*nu)*ep11 ) + ( lam*ep22 );
    sig22 = ( (lam+2*nu)*ep22 ) + ( lam*ep11 );
    sig12 = 2*nu*ep12;

    %Energy flux along the plate
    en_flux = (-1*sig11.*ux) - (-1*sig12.*uy);

    start=start+2;

    if kk==1;

        x2_tot = [-H/2 + ((kk-1)*h) + (x2b*h)];
        ux_tot = [ux];
        uy_tot = [uy];
        ep11_tot = [ep11];
        ep22_tot = [ep22];
        ep12_tot = [ep12];
        sig11_tot = [sig11];
        sig22_tot = [sig22];
        sig12_tot = [sig12];
        en_flux_tot = [en_flux];

    else

        x2_tot = [ [x2_tot(1:end-1)],[-H/2 + ((kk-1)*h) + (x2b*h)] ];
        ux_tot = [[ux_tot(1:end-1)],[ux]];
        uy_tot = [[uy_tot(1:end-1)],[uy]];
        ep11_tot = [[ep11_tot(1:end-1)],[ep11]];
        ep22_tot = [[ep22_tot(1:end-1)],[ep22]];
        ep12_tot = [[ep12_tot(1:end-1)],[ep12]];
```

```
        sig11_tot = [[sig11_tot(1:end-1)],[sig11]];
        sig22_tot = [[sig22_tot(1:end-1)],[sig22]];
        sig12_tot = [[sig12_tot(1:end-1)],[sig12]];
        en_flux_tot = [[en_flux_tot(1:end-1)],[en_flux]];

    end

end

%Plot results
figure(2);
hold on
plot(ux_tot,1000*x2_tot,'r','LineWidth',2)
grid on;
ylabel('Position Along Thickness')
xlabel('Normed Displacment')
legend('In Plane: U1')
xlim([-1.5 1.5])
ylim(1000*[-H/2 H/2])
grid on

figure(3);
hold on
plot(uy_tot,1000*x2_tot,'r','LineWidth',2)
grid on; hold on;
ylabel('Position Along Thickness')
xlabel('Normed Displacment')
legend('Out of Plane: U3')
xlim([-1.5 1.5])
ylim(1000*[-H/2 H/2])
grid on

figure(4); plot(10^-14*sig11_tot,1000*x2_tot,'r','LineWidth',2)
grid on; hold on;
ylabel('Position Along Thickness')
xlabel('Stress')
legend('Sig11')
xlim([-1.5 1.5])
ylim(1000*[-H/2 H/2])
grid on

figure(5); plot(10^-14*sig22_tot,1000*x2_tot,'r','LineWidth',2)
grid on; hold on;
ylabel('Position Along Thickness')
xlabel('Stress')
legend('Sig22')
xlim([-1.5 1.5])
ylim(1000*[-H/2 H/2])
grid on

figure(6); plot(10^-14*sig12_tot,1000*x2_tot,'r','LineWidth',2)
grid on; hold on;
ylabel('Position Along Thickness')
xlabel('Stress')
legend('Sig12')
```

```
xlim([-1.5 1.5])
ylim(1000*[-H/2 H/2])
grid on

figure(7); plot(10^-14*en_flux_tot,1000*x2_tot,'r','LineWidth',2)
grid on; hold on;
ylabel('Position Along Thickness')
xlabel('Energy Flux Density')
title('Average Energy Flux Density')
xlim([-1.5 1.5])
ylim(1000*[-H/2 H/2])
grid on




function [k,m] = quad_element(c11,c12,c22,c66,rho,h,z)

%This function returns a 6x6 matrix which contains the elemental stiffness
%and elemental mass matrix for a 1D safe element that consists of 3 nodes
%and uses quadratic shape functions

%alpha = H / ( pi * zeta * h );

% G = [1 0 0 0 0 0;...
%      0 1 0 0 0 0;...
%      -3 0 4 0 -1 0;...
%      0 -3 0 4 0 -1;...
%      2 0 -4 0 2 0;...
%      0 2 0 -4 0 2];

%element stiffness matrix

k = zeros(6);

k(1,1) = ((2/15)*c11*z*z*h)+((7/3)*c66/h);
k(1,2) = (1/2)*(c66-c12)*z;
k(1,3) = ((1/15)*c11*z*z*h)-((8/3)*c66/h);
k(1,4) = (2/3)*(c12+c66)*z;
k(1,5) = ((-1/30)*c11*z*z*h)+((1/3)*c66/h);
k(1,6) = (-1/6)*(c12+c66)*z;

k(2,1) = k(1,2);
k(2,2) = ((2/15)*c66*z*z*h)+((7/3)*c22/h);
k(2,3) = (-2/3)*(c12+c66)*z;
k(2,4) = ((1/15)*c66*z*z*h)-((8/3)*c22/h);
k(2,5) = (1/6)*(c12+c66)*z;
k(2,6) = ((-1/30)*c66*z*z*h)+((1/3)*c22/h);

k(3,1) = k(1,3);
k(3,2) = k(2,3);
k(3,3) = ((8/15)*c11*z*z*h)+((16/3)*c66/h);
k(3,4) = 0;
k(3,5) = ((1/15)*c11*z*z*h)-((8/3)*c66/h);
```

```
k(3,6) = (2/3)*(c12+c66)*z;

k(4,1) = k(1,4);
k(4,2) = k(2,4);
k(4,3) = k(3,4);
k(4,4) = ((8/15)*c66*z*z*h)+((16/3)*c22/h);
k(4,5) = (-2/3)*(c12+c66)*z;
k(4,6) = ((1/15)*c66*z*z*h)-((8/3)*c22/h);

k(5,1) = k(1,5);
k(5,2) = k(2,5);
k(5,3) = k(3,5);
k(5,4) = k(4,5);
k(5,5) = ((2/15)*c11*z*z*h)+((7/3)*c66/h);
k(5,6) = (1/2)*(c12-c66)*z;

k(6,1) = k(1,6);
k(6,2) = k(2,6);
k(6,3) = k(3,6);
k(6,4) = k(4,6);
k(6,5) = k(5,6);
k(6,6) = ((2/15)*c66*z*z*h)+((7/3)*c22/h);

%element mass matrix

m = zeros(6);

m(1,1) = 4;
m(1,2) = 0;
m(1,3) = 2;
m(1,4) = 0;
m(1,5) = -1;
m(1,6) = 0;

m(2,1) = m(1,2);
m(2,2) = 4;
m(2,3) = 0;
m(2,4) = 2;
m(2,5) = 0;
m(2,6) = -1;

m(3,1) = m(1,3);
m(3,2) = m(2,3);
m(3,3) = 16;
m(3,4) = 0;
m(3,5) = 2;
m(3,6) = 0;

m(4,1) = m(1,4);
m(4,2) = m(2,4);
m(4,3) = m(3,4);
m(4,4) = 16;
m(4,5) = 0;
m(4,6) = 2;
```

```
m(5,1) = m(1,5);
m(5,2) = m(2,5);
m(5,3) = m(3,5);
m(5,4) = m(4,5);
m(5,5) = 4;
m(5,6) = 0;

m(6,1) = m(1,6);
m(6,2) = m(2,6);
m(6,3) = m(3,6);
m(6,4) = m(4,6);
m(6,5) = m(5,6);
m(6,6) = 4;

m = (1/30)*rho*h.*m;
```

Appendix C: M-File for calculating theoretical scattering of compression wave from a finite sized hole in a thin elastic plate.

```
%Pao paper "Dynamic Stress Concentration in an Elastic Plate"
clear all
close all

a_a = 4.7124; %Product of wavenumber and hole radius
nu = 1/3;     %Poisson's ratio
ks = 2 / (1-nu);    %constant
b_a = a_a * sqrt(ks);   %constant

th = 0:2*pi/400:2*pi;   %Angle of inspection in radians
sig_th = zeros(size(th));   %Stress_th initialized zeros
sig_st = zeros(size(th));   %Stress_r initialized zeros
u_r = zeros(size(th));      %Displacement_r initialized zeros
u_th = zeros(size(th));     %Displacement_th initialized zeros

%Loop over angles
for m = 1:length(th);

    %Number of terms in series
    for n = 0:40;
        %Calculate constants

        Dna = ( (n^2+n-1/2*b_a^2)*besselj(n,a_a) ) - ( a_a*besselj(n-1,a_a)
);

        Ena = ( n*(n+1)*besselj(n,a_a) ) - ( n*a_a*besselj(n-1,a_a) );

        Fna = ( -1*(n^2+n-a_a^2+1/2*b_a^2)*besselj(n,a_a) ) + (
a_a*besselj(n-1,a_a) );

        sDna = ( (n^2+n-1/2*b_a^2)*besselh(n,a_a) ) - ( a_a*besselh(n-1,a_a)
);

        sEna = ( n*(n+1)*besselh(n,a_a) ) - ( n*a_a*besselh(n-1,a_a) );

        sFna = ( -1*(n^2+n-a_a^2+1/2*b_a^2)*besselh(n,a_a) ) + (
a_a*besselh(n-1,a_a) );

        sKna = ( -1*n*(n+1)*besselh(n,b_a) ) + ( n*b_a*besselh(n-1,b_a) );

        Kna = ( -1*(n^2+n-1/2*b_a^2)*besselh(n,b_a) ) + (b_a*besselh(n-
1,b_a));

        Jnp_aa = (1/2) * ( besselj(n-1,a_a) - besselj(n+1,a_a) );

        Hnp_aa = (1/2) * ( besselh(n-1,a_a) - besselh(n+1,a_a) );
```

```
        Hnp_ba = (1/2) * ( besselh(n-1,b_a) - besselh(n+1,b_a) );

        del = det( [sDna,sKna;sEna,Kna] );

        delr = det( [a_a*Jnp_aa, a_a*Hnp_aa, n*besselh(n,b_a);...
            Dna,sDna,sKna;...
            Ena,sEna,Kna] );

        delth = det( [-1*n*besselj(n,a_a), -1*n*besselh(n,a_a), -
1*b_a*Hnp_ba;...
            Dna,sDna,sKna;...
            Ena,sEna,Kna] );

        delthth = det( [Fna, sFna, -1*sKna;...
            Dna,sDna,sKna;...
            Ena,sEna,Kna] );

        if n == 0;

            u_r(m) = u_r(m) + ( 1*i^(n) * (delr/del) * cos(n*th(m)) );

            u_th(m) = u_th(m) + ( 1*i^(n) * (delth/del) * sin(n*th(m)) );

            sig_th(m) = sig_th(m) + ( 1*i^(n) * (delthth/del) * cos(n*th(m))
);

        else

            u_r(m) = u_r(m) + ( 2*i^(n) * (delr/del) * cos(n*th(m)) );

            u_th(m) = u_th(m) + ( 2*i^(n) * (delth/del) * sin(n*th(m)) );

            sig_th(m) = sig_th(m) + ( 2*i^(n) * (delthth/del) * cos(n*th(m))
);

        end

    end
    sig_st(m) = 2/ks*(ks-1-2*cos(2*th(m)));
end

%Calculate stress
sig_th = -2/((a_a^2)*ks)*sig_th;
%Normalize displacements
u_r = (1/a_a)*u_r;
u_th = (1/a_a)*u_th;


%Plotting Section
figure(1);
polarplot(th,abs(sig_th));hold on;
polarplot(th,sig_st,'r-');
```

```
thetalim([0 360]);rlim([0.0 3.0]);
title('Stress (|\sigma_{\theta\theta}|)')

figure(2);
polarplot(th,abs(u_r));hold on;
thetalim([0 360]);rlim([0 2]);
title('Displacement (|u_{r}|)')

figure(3);polarplot(th,abs(u_th));hold on;
thetalim([0 360]);rlim([0 2]);
title('Displacement (|u_{\theta}|)')
legend('ka = 3.5','ka = 0.01','location','northwest')

figure(6);
polarplot(th,abs( (u_r.*cos(th))-(u_th.*sin(th)) ) );hold on;
polarplot(th,abs( (u_r.*sin(th))+(u_th.*cos(th))) );
thetalim([0 360]);rlim([-1 2]);
title('Displacement |u_x| and |u_y|')
legend('|u_x| ka = 0.01','|u_y| ka = 0.01','location','northwest')
```